Supplementary Materials for "Theory of Superconductivity in $LaRu_3Si_2$ and Predictions of New Kagome Flat Band Superconductors"

Junze Deng*[1,2,3], Yi Jiang†[4], Tiago F. T. Cerqueira‡[5], Haoyu Hu[6,4], Eeli O. Lamponen[1], Dumitru Călugăru[7], Hanqi Pi[4], Zhijun Wang[2,3], Maia G. Vergniory[4,8], Emilia Morosan[9,10,11], Titus Neupert[12], S. Blanco-Canosa[4,13], Claudia Felser[14], Kristjan Haule[15], Miguel A. L. Marques[16], Päivi Törmä§[1], and B. Andrei Bernevig¶[4,7,13]

[1]Department of Applied Physics, Aalto University School of Science, FI-00076 Aalto, Finland
[2]Beijing National Laboratory for Condensed Matter Physics, and Institute of Physics, Chinese Academy of Sciences, Beijing 100190, China
[3]University of Chinese Academy of Sciences, Beijing 100049, China
[4]Donostia International Physics Center (DIPC), Paseo Manuel de Lardizábal. 20018, San Sebastián, Spain
[5]CFisUC, Department of Physics, University of Coimbra, Rua Larga, 3004-516 Coimbra, Portugal
[6]Department of Physics, University of Science and Technology of China, Hefei, Anhui 230026, China
[7]Department of Physics, Princeton University, Princeton, NJ 08544, USA
[8]Département de Physique et Institut Quantique, Université de Sherbrooke, Sherbrooke, J1K 2R1 Québec, Canada
[9]Department of Physics and Astronomy, Rice University, Houston, TX 77005, USA
[10]Department of Physics and Astronomy, Rice Center for Quantum Materials (RCQM), Rice University, Houston, Texas 77005, USA
[11]Smalley-Curl Institute, Rice University, Houston, TX 77005, USA
[12]Department of Physics, University of Zurich, Winterthurerstrasse 190, 8057 Zurich, Switzerland
[13]IKERBASQUE, Basque Foundation for Science, 48013 Bilbao, Spain
[14]Max Planck Institute for Chemical Physics of Solids, 01187 Dresden, Germany
[15]Center for Materials Theory, Department of Physics and Astronomy, Rutgers University, Piscataway, NJ 08854, USA
[16]Research Center Future Energy Materials and Systems of the University Alliance Ruhr and Interdisciplinary Centre for Advanced Materials Simulation, Ruhr University Bochum, Universitätsstraße 150, D-44801 Bochum, Germany

Contents

S1 Details of first-principles calculations **2**
S1.1 Electronic-structure calculations and structural relaxation 2
S1.2 Phonon and electron-phonon coupling calculations 3
S1.3 DFT+DMFT calculations 3
S1.4 High-throughput screening of the 1:3:2 family 3

*These authors contributed equally to this work.
†These authors contributed equally to this work.
‡These authors contributed equally to this work.
§paivi.torma@aalto.fi
¶bernevig@princeton.edu

S2 First-principles results **4**
S2.1 Kagome materials from LEGO building blocks . . . 4
S2.2 $LaRu_3Si_2$: phases and conventions . . . 5
S2.3 Lattice dynamics and the origin of the CDW phases . . . 8
S2.3.1 Soft phonons of the SG 191 ($P6/mmm$) phase . . . 8
S2.3.2 The $1 \times 1 \times 2$ phases in SG 193 and SG 176 . . . 10
S2.3.3 The $1 \times 1 \times 2$ phase in SG 66 . . . 10
S2.3.4 Mode decomposition of the $1 \times 1 \times 2$ distortions . . . 11
S2.3.5 Low-temperature CDW phases: SG 51 and SG 55 . . . 12
S2.3.6 Phonons under pressure . . . 14
S2.4 Electronic structure . . . 15
S2.4.1 Quasi-flat band and Fermi surfaces . . . 15
S2.4.2 Zone folding across the structural transitions . . . 18
S2.4.3 Spin-orbit coupling and correlation effects . . . 20
S2.5 Electron-phonon coupling and superconductivity . . . 22
S2.5.1 EPC matrix elements and spectral functions . . . 22
S2.5.2 Local-axis decomposition of the electron-phonon coupling . . . 24
S2.5.3 Evaluation of superconducting properties . . . 26
S2.5.4 Mode-resolved EPC in the reference phases . . . 27
S2.5.5 Superconductivity in undoped $LaRu_3Si_2$ . . . 31
S2.5.6 Doping dependence and competing instabilities . . . 32

S3 Analytical models **43**
S3.1 Electron-phonon coupling of $d_{x^2-y^2}$ orbitals . . . 43
S3.1.1 Slater-Koster hopping . . . 44
S3.1.2 Displacement derivatives and EPC . . . 47
S3.1.3 Interorbital A_g–B_{1g} hopping . . . 49
S3.2 Spring-ball model for the kagome lattice . . . 50

S4 Tight-binding model and superfluid weight **54**

S5 Superconducting candidates in the 1:3:2 family **58**
S5.1 Type I: compounds with d-derived kagome bands . . . 58
S5.2 Type II: compounds with p-derived kagome bands . . . 59
S5.3 Scope of the screening . . . 59
S5.4 Candidate tables and spectral data . . . 60

S1 Details of first-principles calculations

Unless otherwise stated, Sections S1.1 to S1.3 describe calculations for $LaRu_3Si_2$. The separate computational protocol used for the screening of the 1:3:2 family is given in Section S1.4.

S1.1 Electronic-structure calculations and structural relaxation

First-principles calculations were performed based on density functional theory (DFT), using the projector augmented wave method [1, 2], as implemented in the Vienna *ab initio* Simulation Package (`VASP`) [3, 4] and the Quantum ESPRESSO package [5, 6]. The generalized gradient approximation was used, incorporating the Perdew-Burke-Ernzerhof (PBE) exchange-correlation func-

tional [7]. The internal atomic positions within the structures were relaxed until the forces on each atom were reduced to less than 0.1 meV/Å. A kinetic energy cutoff of 500 eV or 100 Ry was set for the plane-wave basis set. The Brillouin zone (BZ) was sampled using the Monkhorst-Pack method [8] with a Γ-centered **k**-point grid of $9 \times 9 \times 12$ and $9 \times 9 \times 6$ for $LaRu_3Si_2$ in the SG 191 and SG 66 ($1 \times 1 \times 2$) phase respectively.

Irreducible representations (irreps) were determined using `IRVSP` [9, 10]. Wannier-based calculations were done with WannierTools [11]. The band representation analysis was conducted on the website `BRdecomp`. Furthermore, a Wannier-based tight-binding Hamiltonian was constructed using Wannier90 [12, 13], with La-d, Ru-s, d and Si-p orbitals.

S1.2 Phonon and electron-phonon coupling calculations

Phonon spectra were calculated via `VASP` using the frozen phonon method in conjunction with the `PHONOPY` package [14, 15] and via the Quantum ESPRESSO package in the framework of density functional perturbation theory (DFPT).

Electron-phonon coupling (EPC) properties were computed using the `EPW` package [16–19], included within Quantum ESPRESSO [5, 6]. Electron-phonon matrix elements were first computed on coarse **k**-point and **q**-point meshes ($9 \times 9 \times 12$ and $9 \times 9 \times 6$ for the SG 191 and SG 66 phases, respectively) and then interpolated onto finer grids using maximally localized Wannier functions.

S1.3 DFT+DMFT calculations

To study electronic correlation effects, first-principles calculations combining DFT and embedded dynamical mean-field theory (eDMFT) were performed using `WIEN2k` and the `Rutgers eDMFT` code [20, 21]. The local-density approximation [22] was employed, as it provides optimal results for lattice properties when combined with eDMFT [23, 24]. Coulomb repulsion and Hund's coupling parameters were set to $U = 6.0$ eV and $J_H = 0.9$ eV, respectively. The auxiliary impurity problem in eDMFT was solved using a continuous-time quantum Monte Carlo impurity solver [25].

S1.4 High-throughput screening of the 1:3:2 family

The family-wide screening of Section S5 was run with a separate, uniform protocol, described here. The two sets of numbers are therefore not interchangeable, and the comparisons drawn in Section S5 are made within the screening set.

High-throughput *ab initio* calculations were performed to study the kagome family RT_3X_2, crystallizing in space group (SG) 191 ($P6/mmm$). The chemical space was explored by systematically substituting elements up to Bi in all possible combinations within the prototype structure. From the resulting compounds, we selected those with distances to the convex hull below 100 meV/atom (calculated within the PBE approximation [7] against the Alexandria database [26, 27]), metallic, and nonmagnetic. For the resulting 3063 candidate materials, we performed DFPT calculations to obtain the EPC constants. All calculations were performed using Quantum Espresso (version 7.1) [5, 6] with the Perdew-Burke-Ernzerhof generalized gradient approximation for solids (PBEsol) [28], and we chose the PBEsol pseudopotentials from the pseudodojo project [29], specifically the stringent, scalar-relativistic norm-conserving set. Geometry optimizations were performed using uniform Γ-centered **k**-point grids with a density of 1500 **k**-points per reciprocal atom. Convergence thresholds for energies, forces, and stresses were set to 1×10^{-8} a.u., 1×10^{-6} a.u., and 5×10^{-2} kBar, respectively. For electron-phonon calculations, we used the double-grid technique, using the previous k-grid as the coarse grid and a quadrupled **k**-grid for the fine sampling. Phonon **q**-points were sampled at half the initial **k**-point grid. The Eliashberg function was

obtained through double delta integration using Methfessel-Paxton smearing [30] of 0.03 Ry. Materials exhibiting imaginary frequencies at explicitly calculated **q**-points were excluded from further analysis, while those developing instabilities during Fourier interpolation were retained but flagged as potentially unstable.

Superconducting transition temperatures were estimated using the McMillan formula [31, 32] [Eq. (S2.32)] with $\mu^* = 0.10$, the same Coulomb pseudopotential used for $LaRu_3Si_2$ in Section S2.5.5.

S2 First-principles results

S2.1 Kagome materials from LEGO building blocks

Kagome materials in SG 191 crystallize in various structures, including the 1 : 1, 1 : 6 : 6, 1 : 3 : 5, and 1 : 3 : 2 families, with representative materials such as FeGe, $MgFe_6Ge_6$, CsV_3Sb_5, and $LaRu_3Si_2$, respectively. Despite their distinct properties, the crystal and even electronic band structures of these materials can be understood through the 1 : 1 (or 3 : 3) family, which serves as a foundational "LEGO" building block [33].

We begin by examining the crystal structure in different kagome families, as illustrated in Fig. S2.1.

- In the 1 : 1 family, the unit cell contains an equal number of honeycomb, triangular, and kagome layers, with the triangular and kagome lattices lying on the same plane (sharing the same z-coordinate).

- The 1 : 6 : 6 structure can be obtained by doubling the unit cell of the 1 : 1 structure along the z-direction and adding an additional atom (triangular lattice) to one of the honeycomb layers. Thus we have the relation $(1:6:6) = 2 \times (0:3:3) + (1:0:0)$.

- In the 1 : 3 : 5 family, the unit cell contains one kagome, two honeycomb, and two triangular layers. The kagome layers are sandwiched between two honeycomb layers within the same unit cell. One of the triangular lattices lies in the same plane as the kagome lattice, while the other triangular lattice, composed of alkali metals, is positioned between two honeycomb layers from adjacent unit cells. Starting from the 3 : 3 structure, one can first double the unit cell along the z-direction to obtain the 6 : 6 structure. Then, one layer formed by the kagome and triangular lattices is replaced by a distinct triangular lattice composed of alkali metals. Thus we have the relation $(1:3:5) = 2 \times (0:3:3) - (0:3:1) + (1:0:0)$.

- The 1 : 3 : 2 family contains the same number of atoms as the 1 : 1 family but features triangular and honeycomb lattices formed by different elements. Additionally, unlike the 1 : 1 structure, where the triangular lattice lies in the same plane as the kagome lattice, the 1 : 3 : 2 structure places the triangular and honeycomb lattices on the same plane. Thus we have the relation $(1:3:2) = (0:3:3) - (0:0:1) + (1:0:0)$.

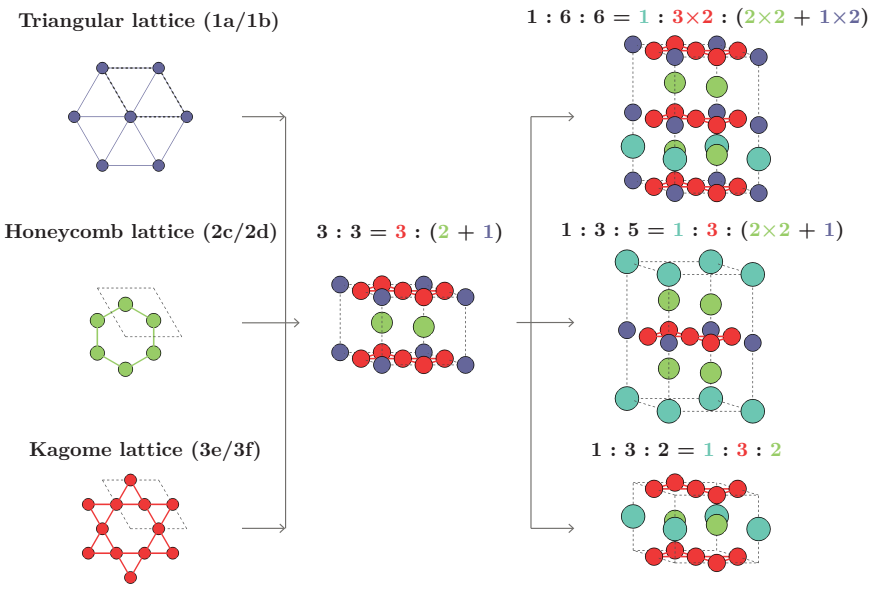


Figure S2.1: Crystal structures of various kagome material families and their connection to the 1 : 1 structure. The 1 : 1 (or 3 : 3) structure acts as a fundamental LEGO building block for different kagome materials.

In addition to the structural similarity, the electronic band structures of different kagome families also originate from similar LEGO building blocks. In these kagome metals, the kagome lattice is consistently formed by transition metal elements, producing kagome bands near the Fermi level primarily contributed by the *d*-electrons. As demonstrated in Ref. [33], the complex *spaghetti*-like electronic structure of the 1 : 1 family, exemplified by FeGe, can be understood by partitioning the kagome *d*-orbitals into distinct groups based on the symmetry and chemical analysis. Each group of *d* orbitals couples to specific *p* or *s* orbitals from neighboring lattices, forming separate LEGO building blocks. These blocks effectively describe the kagome band structures and have been successfully extended to the 1 : 6 : 6 and 1 : 3 : 5 families [33, 34]. In the following Section S2.4.1, we show that the 1 : 3 : 2 family, represented by $LaRu_3Si_2$, also shares similar LEGO building blocks of *d* orbitals in its band structure.

S2.2 $LaRu_3Si_2$: phases and conventions

$LaRu_3Si_2$ is a prominent member of the kagome 1 : 3 : 2 family and a paramagnetic type-II superconductor with a transition temperature $T_c \sim 7.8\,\mathrm{K}$ [35–40], the highest reported among kagome metals at ambient pressure. It carries a quasi-flat band (FB) close to the Fermi level without ordering magnetically, and muon spin rotation (μSR) experiments give compelling evidence that the superconducting state is a nodeless *s*-wave [38–40]. These are the two facts that the rest of this section has to reconcile: a large FB density of states (DOS), and a conventional gap.

The material reaches that state through a sequence of structural transitions, summarized below following Ref. [41]. The corresponding structures are shown in Fig. S2.2. The DFT analysis of how they arise from the soft phonons of the parent phase is given in Section S2.3.

- Above 620 K: $LaRu_3Si_2$ crystallizes in SG 191 ($P6/mmm$) as shown in Fig. S2.2(a)(d), representing the most symmetric structure. In this phase, the unit cell comprises a kagome layer at Wyckoff position (WKP) 3*g* formed by Ru atoms, a triangular lattice at WKP 1*a* formed

by La atoms, and a honeycomb lattice at WKP $2c$ formed by Si atoms. We call this phase the SG 191 phase through this manuscript.

- Between 400 and 620 K: the compound was first reported in the SG 176 ($P6_3/m$) setting [35] [Fig. S2.2(c)(f)], with the unit cell doubled along the z-axis and the C_{6z} symmetry broken by in-plane displacements of the kagome Ru atoms, a C_{6z}-screw symmetry $\tilde{C}_{6z} \equiv \{C_{6z}|0,0,1/2\}$ being retained. The structure could not later be fully refined in SG 176. Refinement succeeded instead in SG 66 ($Cccm$) [41] [Fig. S2.2(i)(k)]. We show in Sections S2.3.2 and S2.3.3 that the two settings condense out of two different soft modes of the SG 191 phase and that only SG 66 is harmonically stable, so we take SG 66 as the structure of this mid-temperature phase and refer to it as the $1 \times 1 \times 2$ ($Cccm$) phase throughout this work.
- Around 400 K: The first charge-ordered phase, CO-I, emerges in the super space group $Cmmm(0b0)s00$, with modulation vectors $\mathbf{q} = (1/4, 0, 0)$, $(0, 1/4, 0)$, and $(1/4, -1/4, 0)$ relative to the $1 \times 1 \times 2$ BZ [41, 42]. The crystal structure of this phase is illustrated in Fig. S2.2(j)(l).
- A second charge-ordered phase, CO-II, emerges alongside the CO-I phase and is most pronounced in Fe-doped samples ($x = 0.01$). This phase is characterized by modulation vectors $\mathbf{q} = (1/6, 0, 0)$, $(0, 1/6, 0)$, and $(1/6, -1/6, 0)$ relative to the $1 \times 1 \times 2$ BZ [41]. In undoped $LaRu_3Si_2$, CO-II is observed at a lower transition temperature ($T_{\text{CO-II}} \sim 80$ K) [41, 42].

Local frames on the kagome lattice. Ru d orbitals and phonon polarizations are labelled in the site-local frames shown in Fig. S2.3, with orientations defined by $\mathcal{R}_i^{ph}$ in Eq. (S3.12). Under the D_{2h} (mmm) site symmetry of the $3g$ Wyckoff position, the local $d_{x^2-y^2}$ orbital and x-polarized displacement transform as A_g and B_{3u}, respectively (see Table S2.1).

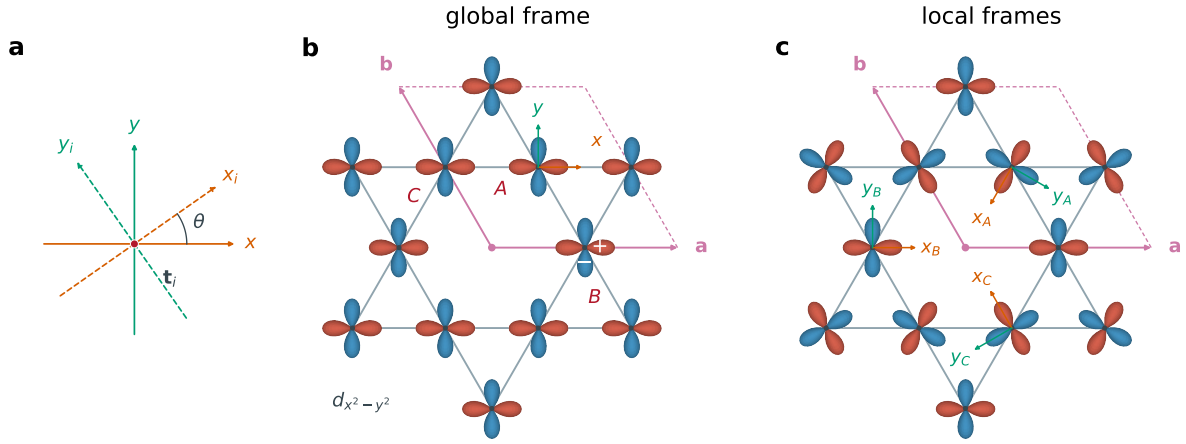


Figure S2.3: **a** Schematic illustration of a generic rotation of coordinate axes at site $\mathbf{t}_i$. Here, x and y represent the global Cartesian axes, while x_i and y_i denote the local axes. The rotation angle θ is defined anticlockwise. **b** and **c** Illustrations of coordinate systems on the kagome lattice, drawn with the direct lattice vectors and the three $3g$ sublattices of Section S3.1.1, labelled A, B and C: **b** $d_{x^2-y^2}$ orbitals defined in the global coordinate system. **c** $d_{x^2-y^2}$ orbitals defined in the local coordinate systems on the kagome lattice, with the local axes indicated by arrows (x_i orange, y_i green).

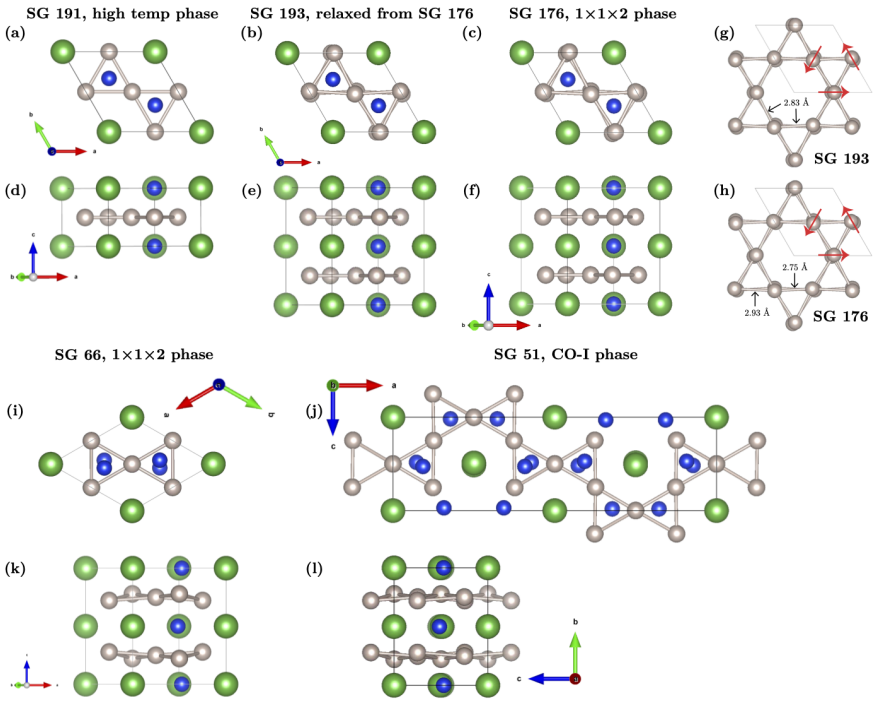


Figure S2.2: Structure of $LaRu_3Si_2$ in SG 191 [(a), (d)], 193 [(b), (e)], 176 [(c), (f)], 66 [(i), (k)], and 51 [(j), (l)], where the first row is the top view and the second row is the side view. SG 193, 176, and 66 are possible $1 \times 1 \times 2$ structures of the high-temperature structure in SG 191, while SG 51 is a $4 \times 4 \times 2$ CDW structure. The SG 193 and 176 structures are nearly identical, with the largest displacements being the inplane movements of Ru atoms. The SG 66 and 51 phases, however, have Ru atoms slightly moved in-plane but largely moved out-of-plane, while Si atoms displace oppositely. Panels (g) and (h) magnify the Ru kagome net of the SG 193 and SG 176 structures, with red arrows giving the in-plane Ru displacements toward the hexagon centers and the resulting Ru–Ru distances: a single 2.83 Å bond in SG 193, against the two inequivalent 2.75 and 2.93 Å bonds of SG 176. Structures are obtained from Refs. [41, 42].

Table S2.1: Irreps of site symmetry group $mmm(D_{2h})$ for WKP $3g$ in SG 191 ($P6/mmm$).

Irrep (ρ)	C_{2z}	C_{2y}	C_{2x}	$\mathcal{P}$	$\mathcal{M}_z$	$\mathcal{M}_y$	$\mathcal{M}_x$	orbitals
A_g	1	1	1	1	1	1	1	$s, d_{x^2-y^2}, d_{z^2}$
B_{1g}	1	−1	−1	1	1	−1	−1	d_{xy}
B_{2g}	−1	1	−1	1	−1	1	−1	d_{xz}
B_{3g}	−1	−1	1	1	−1	−1	1	d_{yz}
A_u	1	1	1	−1	−1	−1	−1	
B_{1u}	1	−1	−1	−1	−1	1	1	p_z
B_{2u}	−1	1	−1	−1	1	−1	1	p_y
B_{3u}	−1	−1	1	−1	1	1	−1	p_x

S2.3 Lattice dynamics and the origin of the CDW phases

The whole structural sequence of Section S2.2 follows from the phonons of the parent SG 191 cell. We start from its soft modes, condense them one at a time to obtain the $1 \times 1 \times 2$ candidates, decompose the observed distortions onto the parent modes to identify which soft mode each phase actually uses, and then follow the same kagome net into the low-temperature charge density wave (CDW) phases and under pressure.

S2.3.1 Soft phonons of the SG 191 ($P6/mmm$) phase

In the SG 191 phase the structure comprises a kagome lattice of Ru atoms at $z = c/2$ and, at $z = 0$, a honeycomb lattice of Si atoms and a triangular lattice of La atoms (c the lattice constant along z), occupying WKPs $3g$, $2c$ and $1a$ respectively [Fig. S2.2(a)]. To explore the stability of this phase at lower temperatures, we performed DFPT calculations within the harmonic approximation. The phonon spectrum, presented in Fig. S2.4 and Fig. S2.5**a**, carries imaginary frequencies spanning the $q_z = \pi$ plane, so the high-symmetry phase is dynamically unstable. The irreps of these unstable modes at the A point are labeled in Fig. S2.5**a**, following the convention of the Bilbao Crystallographic Server [43, 44]. Among the three, the one-dimensional A_4^+ mode is mainly in-plane Ru motion directed toward the centers of the hexagons, the local x of the kagome site, as the phonon orbital weights in Fig. S2.6**a** confirm. As shown in Fig. S2.4, increasing the smearing parameter in the Fermi-Dirac distribution within the *ab initio* calculations hardens this mode, while the two-dimensional A_5^+ mode remains largely unaffected by electronic temperature. The selective hardening suggests that the A_4^+ phonon softening is likely driven by EPC. This behavior closely resembles the phonon softening observed in 1T-phase transition metal dichalcogenide materials [45, 46], MgB_2 [47, 48], and KV_3Sb_5 [49].

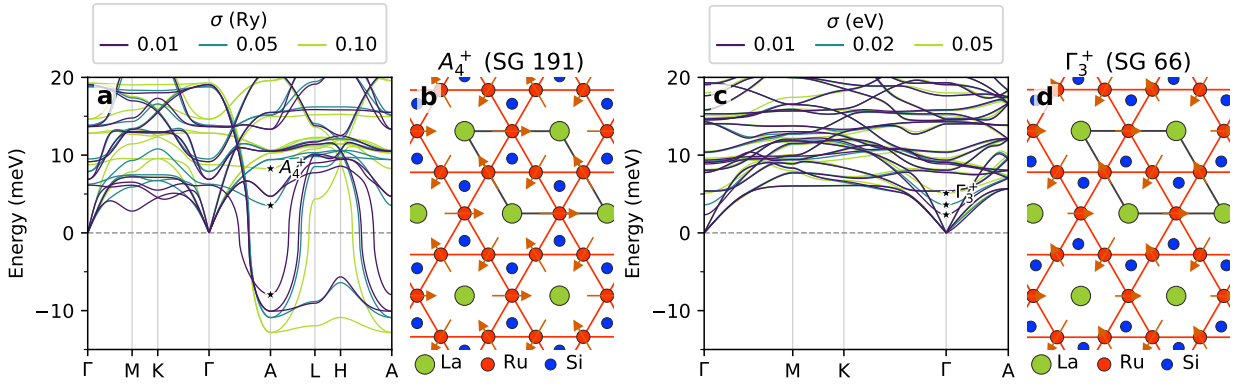


Figure S2.4: **a** Phonon spectrum of the pristine SG 191 phase at $\sigma = 0.01$, 0.05 and 0.10 Ry. The non-degenerate A_4^+ mode at A, starred, runs $-7.94 \to 3.53 \to 8.27$ meV, imaginary at the lowest smearing and hardening throughout. **b** Its displacement pattern on the structure seen down c, the Ru kagome net with the unit cell outlined. **c** The same sweep in the SG 66 phase at $\sigma = 0.01$, 0.02 and 0.05 eV. The marked mode is Γ_3^+ at the interior Γ, $2.33 \to 3.61 \to 5.10$ meV, softening without becoming imaginary. **d** Its pattern drawn the same way, here the Ru layer at $z = c/4$ of the twelve-atom cell with the La and Si of the $z = 0$ layer, the two arrow lengths being the mode's own amplitudes, 1 and 0.67. These modes also carry strong EPC, so their softening should be visible as anomalous mode softening and linewidth broadening in Raman and inelastic x-ray or neutron scattering.

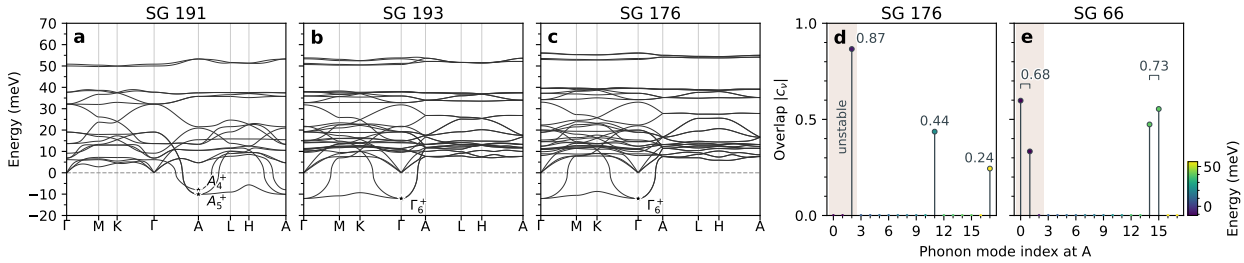


Figure S2.5: Phonon instabilities and distortion-mode decomposition of $LaRu_3Si_2$. **a**–**c** Phonon spectra of the parent SG 191 phase and the $1 \times 1 \times 2$ structures in SG 193 and SG 176, respectively, plotted on a common energy scale. The unstable A_5^+ doublet (-10.07 meV) and A_4^+ singlet (-7.94 meV) are marked at A in **a**. In both doubled cells, the A_4^+ instability is removed, whereas the A_5^+-derived doublet folds to Γ and remains unstable at -12.04 meV in SG 193 and -12.06 meV in SG 176. This residual instability persists at elevated electronic temperatures. **d**, **e** Decomposition of the $1 \times 1 \times 2$ distortions in SG 176 ($P6_3/m$) and SG 66 ($Cccm$), respectively, onto the 18 phonon eigenmodes of the parent SG 191 structure at $A = (0, 0, 1/2)$ [Fig. S2.6**a**–**c**]. Stem heights show the projection amplitudes $|c_\nu|$, and colours indicate mode energies. Shading marks the three unstable modes, and brackets indicate the root-sum-square amplitudes of degenerate pairs. The SG 176 distortion is dominated by the unstable singlet ($|c_\nu| = 0.87$), with additional optical-mode amplitudes of 0.44 and 0.24. The SG 66 distortion is dominated by the unstable and optical doublets, with combined amplitudes of 0.68 and 0.73, respectively.

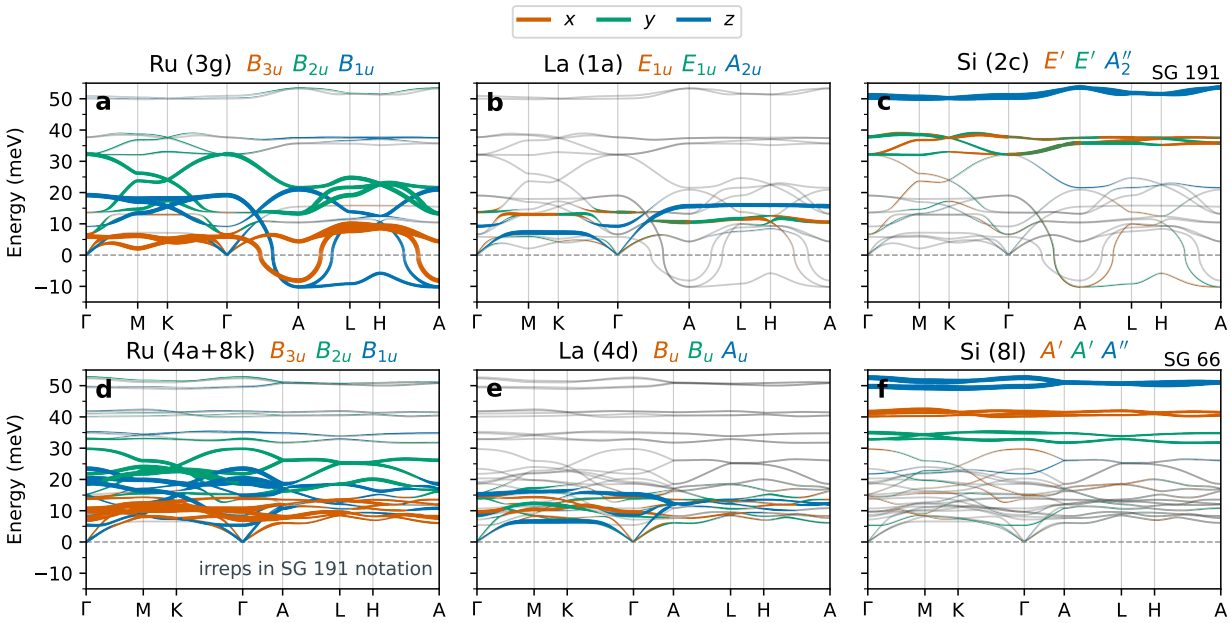


Figure S2.6: Local-orbital resolved phonon spectrum in SG 191 from **a** Ru, **b** La, and **c** Si. The 2D soft mode at A is mainly from the Ru-z phonon, while the 1D soft mode at A is from the Ru-x phonon. The 1D soft phonon can lead to the SG 193/176 structure, while the 2D soft mode can lead to the SG 66 phase. **d**–**f** are the same but for the SG 66 structure, where the soft modes are eliminated.

S2.3.2 The $1 \times 1 \times 2$ phases in SG 193 and SG 176

Experimental studies [35, 41, 42, 50] indicate that the room-temperature (above 400 K) structure of $LaRu_3Si_2$ undergoes a $1 \times 1 \times 2$ reconstruction relative to the SG 191 unit cell. To investigate the underlying phonon instabilities, we generated crystal structures based on the one-dimensional (1D) and two-dimensional (2D) softened phonon modes at the $A(0, 0, 1/2)$ point, corresponding to a $1 \times 1 \times 2$ supercell. As depicted in Fig. S2.2(b) and (e), the structure derived from the 1D A_4^+ mode belongs to SG 193. However, experimental refinements report the structure in SG 176 ($P6_3/m$, shown in Fig. S2.2(c) and (f)) [35]. Notably, SG 176 is a subgroup of SG 193, and it can be obtained from SG 193 by breaking the in-plane symmetry $\tilde{C}_{2x} \equiv \{C_{2x}|0, 0, 1/2\}$. Both SG 193 and SG 176 structures involve in-plane displacements of Ru atoms toward the hexagon centers, as illustrated in Fig. S2.2(g) and (h). The key distinction lies in the nearest-neighbor (NN) bond lengths of Ru atoms: SG 176 exhibits inequivalent NN bonds (2.75 Å and 2.93 Å, Fig. S2.2(h)), whereas SG 193 maintains uniform NN bond lengths (2.83 Å, Fig. S2.2(g)). This structural difference implies that the kagome layers in SG 193 retain in-plane C_{2x} symmetry, while those in SG 176 do not. Despite these variations, phonon spectra in Fig. S2.5**b** and **c** reveal that the 2D softened mode from the SG 191 phase remains present in both SG 193 and SG 176, folding onto the $q_z = 0$ plane. This suggests that the phonon instability persists in these two lower-symmetry structures.

S2.3.3 The $1 \times 1 \times 2$ phase in SG 66

The alternative $1 \times 1 \times 2$ superstructure in SG 66 arises from the condensation of the two-dimensional softened A_5^+ phonon mode. According to the group-subgroup relationship on *Bilbao Crystallo-*

graphic Server [43, 44], condensing the A_5^+ irrep in SG 191 could lead to structure in SG 66, SG 65, or SG 10. After full structural relaxation in DFT, the condensed phonon mode leads to a structure belonging to SG 66 (*Cccm*). In addition to the previously reported SG 176 structure from powder X-ray diffraction [35], recent experimental studies have identified an alternative $1 \times 1 \times 2$ structural phase in SG 66 [41, 42], which is consistent with our theoretical analysis. This phase is primarily characterized by out-of-plane (z-direction) displacements of Ru atoms, as illustrated in Fig. S2.2(k). Notably, the SG 66 structure is harmonically stable at low temperatures, as confirmed by the phonon spectrum shown in Fig. S2.8**a**. Upon further cooling (modeled by decreasing the smearing parameter in the Fermi-Dirac distribution function in DFT from 0.05 eV to 0.01 eV), a 1D phonon mode at Γ softens but does not become imaginary, as indicated by the star in Fig. S2.4**c**. This mode corresponds to the same atomic displacements associated with the A_4^+ mode in the SG 191 phonon spectrum – namely, the in-plane movement of Ru atoms within the kagome lattice toward the centers of the hexagons (Fig. S2.4**d**). The softening reflects the strong EPC of this mode.

S2.3.4 Mode decomposition of the $1 \times 1 \times 2$ distortions

To further verify that the $1 \times 1 \times 2$ structures originate from the condensation of the soft phonons in the high-temperature SG 191 phase, we compare the experimental $1 \times 1 \times 2$ structure in SG 176 and SG 66 with the eigenmodes of the soft phonon at the A point in SG 191. The steps are as follows:

- Starting from the experimental structure in SG 191, we make a $1 \times 1 \times 2$ supercell and use $\mathbf{u}_{i\mu}^{191}$ to denote the atomic positions, where i, μ are the atom and coordinate indices. Similarly, $\mathbf{u}_{i\mu}^{176/66}$ denotes the atomic positions in SG 176 and 66. Then the displacement vector $\Delta\mathbf{u}_{i\mu}^{176/66} = \mathbf{u}_{i\mu}^{176/66} - \mathbf{u}_{i\mu}^{191}$.
- We then compute the phonon eigenmodes, $\{\mathbf{v}_{i\mu}^n\}$ (n being the phonon mode index), at A in SG 191, which form a complete basis for displacements in the $1 \times 1 \times 2$ unit cell.
- Expand $\Delta\mathbf{u}_{i\mu}^{176/66}$ as a linear combination of the eigenmodes: $\Delta\mathbf{u}_{i\mu}^{176/66} = \sum_n c_n \mathbf{v}_{i\mu}^n$, where c_n is the expansion coefficient.
- Compute c_n to quantify the contribution of each eigenmode.

The computed absolute values of the c_n coefficients are shown in Fig. S2.5**d** and **e**. For the SG 176 phase, the largest coefficient comes from the 1D soft mode, which is mainly formed by the local x movements of Ru. We also compute the overlap between the displacement vector $\Delta\mathbf{u}^{176}$ and this 1D soft mode $\mathbf{v}^n$, i.e., $\sqrt{\Delta\mathbf{u}^{176} \cdot \mathbf{v}^n}$, which gives a large overlap of 93.1%. For the SG 66 phase, the largest coefficients come from the 2D soft phonon [i.e., the phonon modes with index 0 and 1 in Fig. S2.5**e**] together with a 2D optical phonon [i.e., the phonon modes with index 14 and 15 in Fig. S2.5**e**, which are the optical modes at about 40 meV in Fig. S2.6**c**]. The 2D soft phonon is mainly given by the z-directional phonon of Ru and the xy phonon of Si, while the 2D optical phonon is given by the xy phonon of Si at about 40 meV. The overlap between the CDW displacement vector and the 2D soft mode (combined using decomposition coefficients) is 97.4%. Thus we conclude that the $1 \times 1 \times 2$ structures in SG 176 and 66 can be understood from the condensation of the 1D and 2D soft phonons in the SG 191 phase, respectively. The SG 193 phase is very close to the SG 176 phase, thus we omit it for simplicity.

S2.3.5 Low-temperature CDW phases: SG 51 and SG 55

Below the CO-I transition the cell grows further and the symmetry drops to SG 51 and SG 55. Here we examine the fully relaxed structures and the phonon spectra of these phases, leaving their electronic structure to Section S2.4.2. The question in each case is the same: whether the kagome ingredients that drive the coupling survive the additional distortion.

Structure analysis. We first examine the structural changes associated with the symmetry lowering from SG 66 to SG 51 and SG 55. The distortion vectors shown in Fig. S2.7**a**–**d**, where black arrows indicate atomic displacements relative to the SG 66 structure and their lengths represent the distortion amplitudes, show that the transition is dominated by in-plane displacements of the Si sublattice. By contrast, the Ru kagome lattice is only weakly perturbed. This can be seen in Fig. S2.7**a,b** for SG 51 and Fig. S2.7**c,d** for SG 55. Thus, the low-temperature CDW distortions primarily affect the Si framework, while leaving the Ru kagome network nearly intact.

Phonon structure. Finally, we compare the phonon spectra of the low-temperature phases. Consistent with the weak distortion of the Ru kagome lattice, the characteristic low-frequency in-plane kagome Ru phonon branch is also preserved. In particular, the B_{3u} (local x) kagome Ru mode remains the lowest-energy branch relative to the corresponding y- and z-polarized modes, as shown in Fig. S2.8. Since this low-frequency in-plane Ru mode provides the dominant phononic ingredient of the EPC mechanism discussed in the main text, its persistence indicates that the essential phonon contribution to superconductivity (SC) remains intact across the low-temperature CDW transitions.

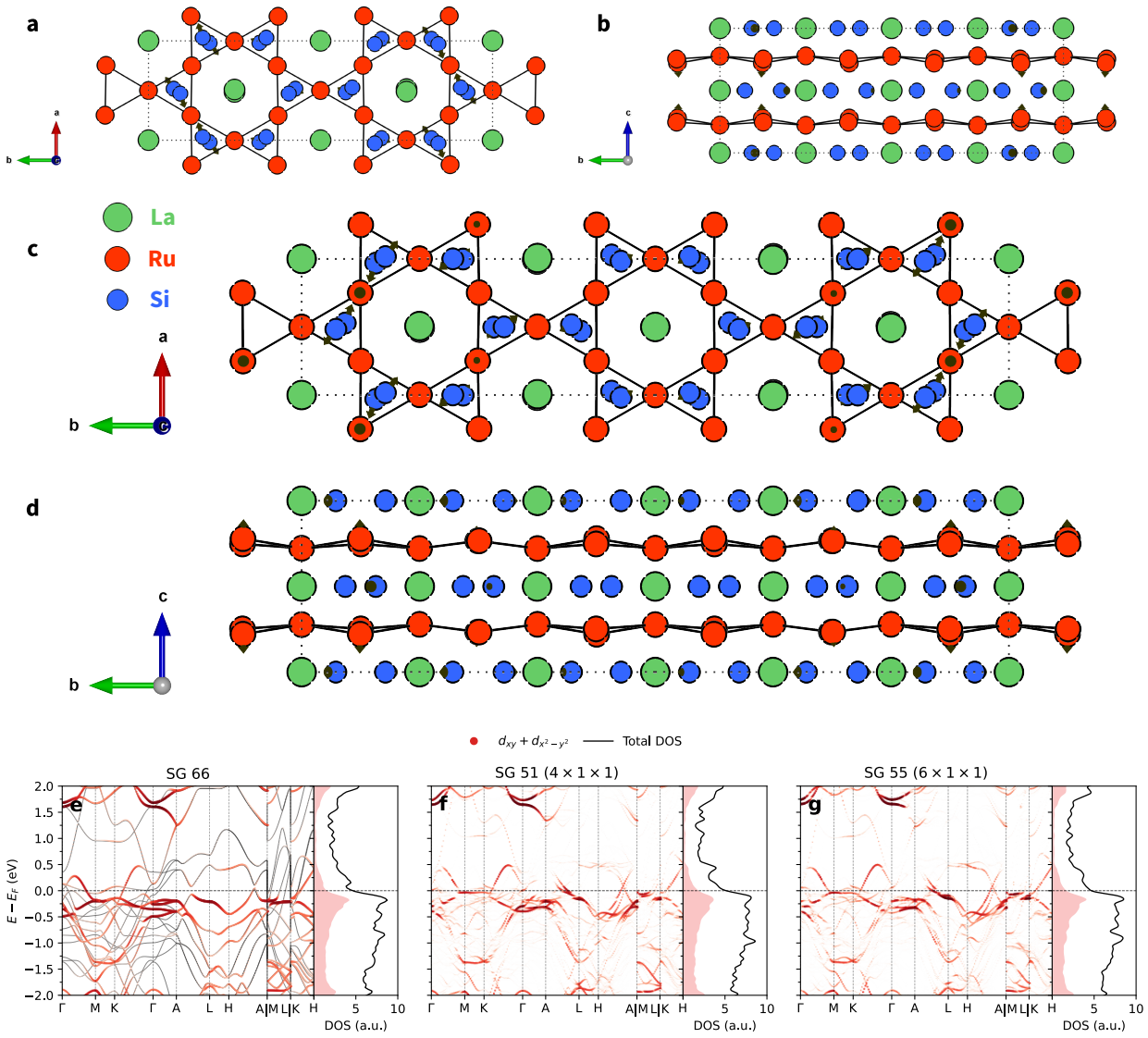


Figure S2.7: Fully relaxed crystal structures of $LaRu_3Si_2$ in the low-T CDW phases: **a** SG 51 (top view), **b** SG 51 (side view along $\hat{\boldsymbol{x}}$), **c** SG 55 (top view), and **d** SG 55 (side view along $\hat{\boldsymbol{x}}$). Black arrows indicate the distortion vectors of the atoms relative to the SG 66 structure. Electronic band structures and DOS of $LaRu_3Si_2$ for **e** SG 66, **f** SG 51, and **g** SG 55. The color scale in the band plots represents the Ru $d_{x^2-y^2} + d_{xy}$ orbital weight. The orbital-resolved bands show that the quasi-FB, dominated by Ru $d_{x^2-y^2}$ character, remains largely preserved across the CDW transitions from the high-T SG 66 phase to the lower-T SG 51 and SG 55 phases, together with the associated DOS peak. The band structures of SG 51 and SG 55 are unfolded into the primitive BZ of SG 66.

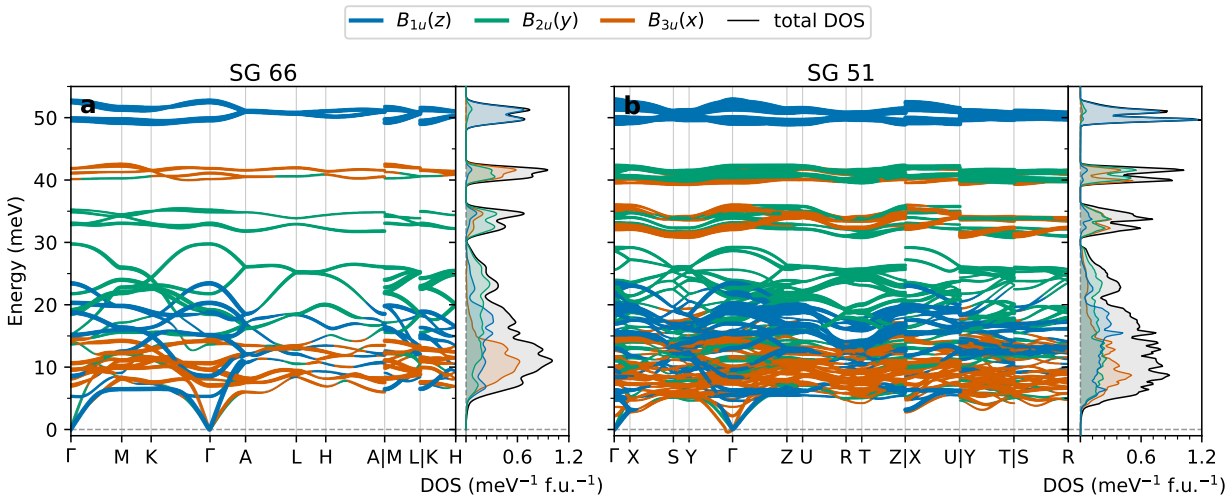


Figure S2.8: Phonon spectra and phonon DOS of $LaRu_3Si_2$ in the SG 66 phase **a** and in the low-temperature SG 51 CDW phase **b**. The branches are colored by their polarization character: $B_{1u}(z)$, $B_{2u}(y)$, and $B_{3u}(x)$. All three soft phonon modes of SG 191 are eliminated in both, and the SG 51 spectrum closely resembles that of SG 66 once the BZ is folded (Fig. S2.12**b**, where the SG 51 zone is one quarter of the SG 66 zone entirely in plane). While the SG 51 phase requires a much larger CDW supercell and therefore makes a full mode-resolved EPC and SC calculation computationally prohibitive, the overall low-energy phonon structure remains similar to that of SG 66. In particular, the low-frequency part of the spectrum is still dominated by the same B_{3u} modes of the kagome Ru lattice, indicating that the main physical ingredients identified in SG 66 are expected to remain relevant in the CDW phase as well.

S2.3.6 Phonons under pressure

To connect our results to recent high-pressure experiments on $LaRu_3Si_2$, we computed the pressure dependence of the phonon spectrum in the SG 66 phase. We do not attempt a complete *ab initio* evaluation of the pressure dependence of the superconducting transition temperature T_c, but the lattice dynamics alone already give a direct, material-specific indication of how the structure evolves under compression.

Our calculations show that, in the SG 66 phase, increasing pressure drives a pronounced softening of the phonon spectrum. In particular, a phonon mode near Γ decreases continuously in energy and becomes imaginary at approximately $P \approx 13\,\mathrm{GPa}$, as shown in Fig. S2.9. This behavior signals the onset of a pressure-induced lattice instability and indicates that the SG 66 structure is no longer dynamically stable beyond this pressure range. The appearance of such an instability suggests that pressure may induce either a structural transition or a substantial reconstruction of the charge-ordered state.

This pressure scale is in good agreement with recent experimental studies of $LaRu_3Si_2$. In particular, Ref. [51] reported anomalous behavior near 11.5-14 GPa that was interpreted as evidence for a possible pressure-induced structural transition at room temperature. In addition, low-temperature measurements in Ref. [52] identified a crossover from long-range to short-range charge order in a similar pressure window, accompanied by a suppression of SC. Our phonon calculations therefore provide a natural microscopic interpretation of these experimental observations, namely that the pressure range where SC is suppressed coincides with the approach to a lattice instability of the SG 66 phase.

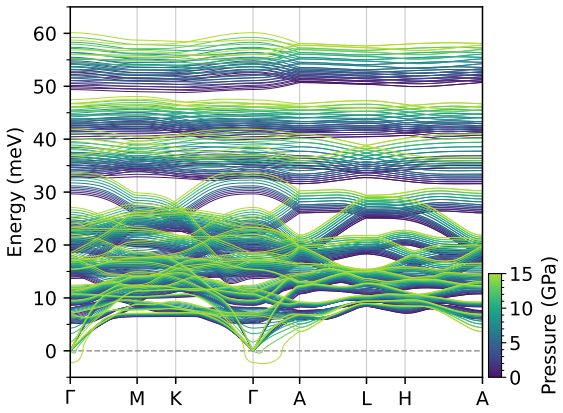


Figure S2.9: Pressure evolution of the phonon spectrum of $LaRu_3Si_2$ in the SG 66 phase. A phonon mode at Γ softens continuously under compression and becomes unstable, *i.e.*, develops an imaginary frequency, above approximately 13 GPa, signaling a pressure-induced lattice instability. This pressure range is consistent with experiments on $LaRu_3Si_2$ reporting either a possible room-temperature structural transition near 11.5-14 GPa [51] or, at low temperature, a crossover from long-range to short-range charge order together with the onset of T_c suppression [52].

S2.4 Electronic structure

We now turn to the electronic structure. The key characteristic of the system is a quasi-FB below the Fermi level (E_F), which produces a pronounced peak in the DOS. We describe it first in the SG 191 and SG 66 phases, then show in Section S2.4.2 that the whole CDW chain leaves it intact, and close with the effects of spin-orbit coupling (SOC) and of electronic correlations.

S2.4.1 Quasi-flat band and Fermi surfaces

We first tabulate the atomic WKPs and the induced elementary band representations (EBRs) [53–55] in Table S2.2 in the high-temperature SG 191 phase of $LaRu_3Si_2$. The electronic structure is dominated by a quasi-FB below the Fermi level E_F, originating primarily from the $d_{x^2-y^2}$ orbitals of the kagome Ru atoms, as seen in the orbital-resolved band structures in Fig. S2.10. This quasi-FB has a maximum at the K point on the $k_z = 0$ plane and significantly contributes to the DOS at approximately -150 meV, as shown in Fig. S2.10**a**. Additionally, a partial FB from the Ru d_{z^2} orbitals is present on the $k_z = \pi$ plane, contributing to a smaller DOS peak at approximately 50 meV below the E_F. The Fermi surfaces (FSs), as shown in Fig. S2.11, are primarily contributed by the $d_{x^2-y^2}$, d_{z^2}, and d_{xz} orbitals of the Ru atoms. That ordering survives the distortion into SG 66, which moves weight out of $d_{x^2-y^2}$ into the two out-of-plane channels without changing which orbitals carry the surface. The d_{xz} orbitals contribute to a more dispersive band with a hole pocket near Γ, which is less relevant to the SC in $LaRu_3Si_2$ (for example, Section S2.5.5 shows the SC gap function which is small on the d_{xz} FS). We remark that the d orbitals in $LaRu_3Si_2$ have similar distributions in the band structure as the 1:1 family FeGe, which could be understood from the LEGO building blocks in FeGe [33].

In Fig. S2.10, the DFT-calculated band structures and orbital contributions for the $1 \times 1 \times 2$ SG 66 phase are presented, revealing only minor modifications compared to SG 191, apart from a twofold band folding along the k_z direction. Furthermore, a comparison of the orbital-resolved

Table S2.2: The atomic valence electrons and their induced band representations of $LaRu_3Si_2$ in the pristine phase SG 191.

Atom	WKP (q)	Symm.	Conf.		Irreps (ρ)	ABRs (ρ@q)
La	$1a$	D_{6h}	s^2d^1	A_{1g}:	s	
				A_{2u}:	p_z	
				E_{1u}:	p_x, p_y	
				A_{1g}:	d_{z^2}	A_{1g}@$1a$
				E_{2g}:	$d_{x^2-y^2}, d_{xy}$	E_{2g}@$1a$
				E_{1g}:	d_{xz}, d_{yz}	E_{1g}@$1a$
Ru	$3g$	D_{2h}	s^1d^7	A_g:	d_{z^2}	A_g@$3g$
				A_g:	$d_{x^2-y^2}$	A_g@$3g$
				B_{1g}:	d_{xy}	B_{1g}@$3g$
				B_{2g}:	d_{xz}	B_{2g}@$3g$
				B_{3g}:	d_{yz}	B_{3g}@$3g$
Si	$2c$	D_{3h}	s^2p^2	A_1':	s	A_1'@$2c$
				A_2'':	p_z	A_2''@$2c$
				E':	p_x, p_y	E'@$2c$

DOS in SG 191 and SG 66 is provided in Fig. S2.10. In SG 66, the DOS at E_F is slightly reduced by about 25% due to the structural reconstruction, decreasing from 2.855 states per unit cell per eV in SG 191 to 2.206 states per unit cell per eV in SG 66 (after normalization for direct comparison). Despite these structural differences, the primary DOS peak at approximately -150 meV persists in both SG 191 and SG 66. This peak is primarily attributed to the Ru $d_{x^2-y^2}$ orbitals, defined according to the local coordinate system illustrated in Fig. S2.3.

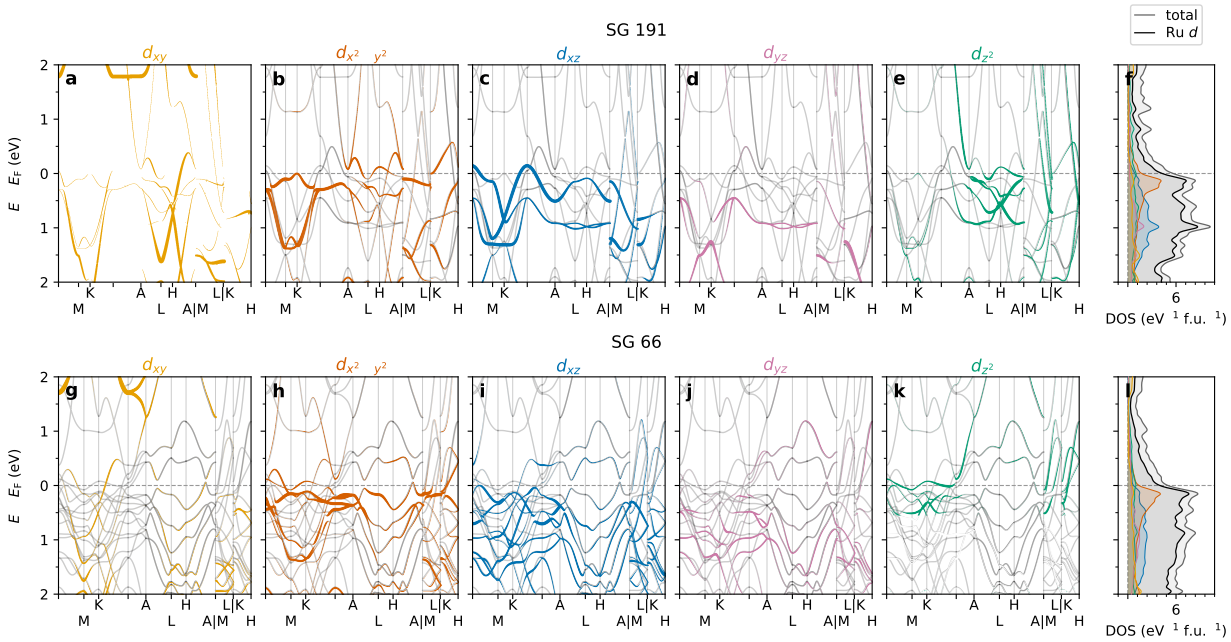


Figure S2.10: Orbital-resolved band structures and DOS of $LaRu_3Si_2$ in the SG 191 phase (**a**–**f**) and the $1\times1\times2$ SG 66 ($Ccmm$) phase (**g**–**l**). The five Ru d orbitals are defined in the local frames shown in Fig. S2.3, with the same convention used in SG 66 despite its broken C_3 symmetry. Ribbon widths represent the weights of the orbitals labelled above each column, with a common normalization across all ten band panels. The quasi-FB near E_F on the $k_z = 0$ plane has predominantly local $d_{x^2-y^2}$ character, which is largely preserved after cell doubling and band folding in SG 66. **f**, **l** Total DOS, Ru d DOS, and individual orbital projections, plotted on a common horizontal scale. The DOS peak approximately 150 meV below E_F is dominated by local $d_{x^2-y^2}$ states in both phases, while the reconstruction reduces the DOS at E_F by approximately 25%. The SG 66 DOS is divided by two to account for cell doubling along z; all DOS curves are calculated without SOC and shown per spin.

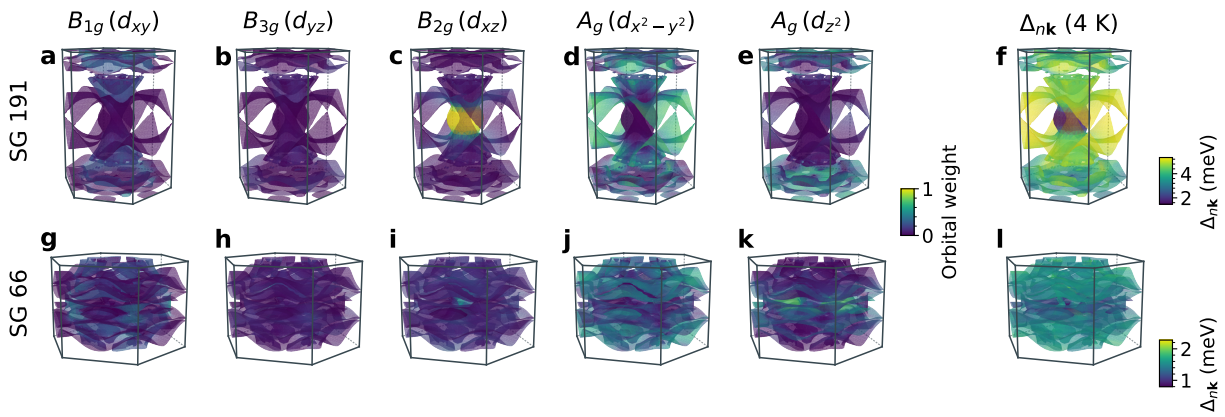


Figure S2.11: Orbital-resolved Fermi surfaces and superconducting gaps of $LaRu_3Si_2$ in the SG 191 phase (**a**–**f**) and the $1 \times 1 \times 2$ SG 66 ($Cccm$) phase (**g**–**l**). **a**–**e**, **g**–**k** Fermi surfaces coloured by individual Ru d-orbital weights on a common 0-1 scale. The orbitals are defined in the local frames of Fig. S2.3 and labelled by the irreps of the $3g$ site-symmetry group. **f**, **l** Anisotropic superconducting gap $\Delta_{n\mathbf{k}}$ at $T = 4\,\mathrm{K}$ and $\mu^* = 0.10$, with separate colour scales (in meV) for the two phases. All panels within each row show the same Fermi surfaces from the same viewpoint. In both phases, the gap is largest in regions with strong $d_{x^2-y^2}$ character and smallest where d_{z^2} character dominates. The area-weighted mean gap decreases from 4.2 meV in SG 191 to 1.5 meV in SG 66. For SG 66, the electronic mesh is twice as dense as the phonon mesh along each axis, yielding eight mesh sublattices uncoupled by the Eliashberg kernel. Mesh-induced variation accounts for approximately one-eighth of the gap variance in **l**; the 29^3 electronic mesh used for SG 191 does not exhibit this partitioning.

S2.4.2 Zone folding across the structural transitions

The unfolded band structures of the $1 \times 1 \times 2$ phases in SG 176, SG 193, and SG 66 closely resemble that of the parent SG 191 phase [Fig. S2.13**b**–**d**]. To distinguish zone-folding effects from distortion-induced changes, we compare the SG 66 bands with the SG 191 bands folded into a $1 \times 1 \times 2$ supercell representation. In this representation, doubling the cell along c halves the BZ height while preserving its in-plane cross-section, so that only the parent Γ and A points fold onto the new Γ point [Fig. S2.12**a**]. The folded bands combine the dispersions along corresponding paths on the $k_z = 0$ and $k_z = \pi/c$ planes of SG 191 [Fig. S2.14**a,b**]. The quasi-FB below E_F in SG 66 derives from the Ru $d_{x^2-y^2}$ band on the parent $k_z = 0$ plane, whereas the branch crossing E_F originates from the corresponding band on the $k_z = \pi/c$ plane, folded onto $k_z = 0$.

The subsequent SG 66 $\rightarrow$ SG 51 transition involves only in-plane folding, mapping four points of the SG 66 BZ onto the new Γ point [Fig. S2.12**b**]. The unfolded bands and DOS of SG 51 and SG 55 show that the quasi-flat Ru $d_{x^2-y^2}$ band remains near E_F, with its associated DOS peak largely preserved [Fig. S2.7**e**–**g**]. The distortions open small hybridization gaps between folded branches but largely preserve the low-energy kagome electronic structure relevant to our EPC mechanism, both across the C_{3z}-breaking SG 191 $\rightarrow$ SG 66 transition and through the subsequent transitions to SG 51 and SG 55.

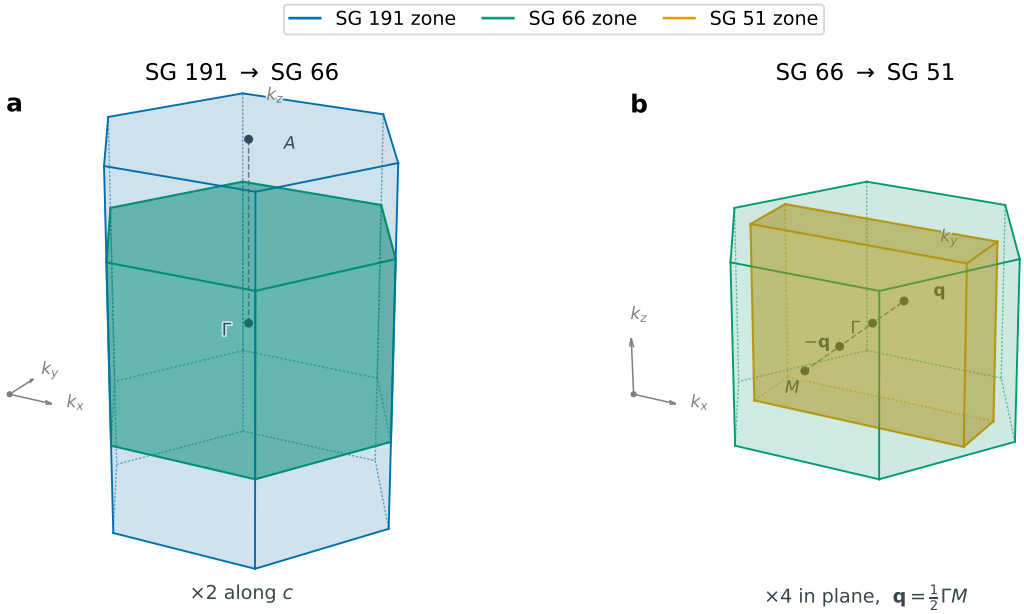


Figure S2.12: Brillouin-zone folding along the SG 191 → SG 66 → SG 51 distortion sequence of $LaRu_3Si_2$. **a** BZs of SG 191 (blue) and SG 66 (green). Doubling the real-space cell along c halves the BZ height while preserving its in-plane cross-section. The parent Γ and $A = (0, 0, 0.886)$ Å^{-1} points fold onto the SG 66 Γ point. **b** BZs of SG 66 (green) and SG 51 (orange). The in-plane reconstruction reduces the BZ volume by a factor of four while preserving its k_z extent. The four parent points Γ, $\pm\mathbf{q}$, and M, with $\mathbf{q} = \frac{1}{2}\overrightarrow{\Gamma M}$, lie along the k_y axis and fold onto the SG 51 Γ point. Both panels use the same viewpoint and scale in the SG 66 Cartesian reciprocal-space frame; dashed lines indicate hidden edges, and grey arrows mark the coordinate axes. The primitive-cell sizes and phonon-branch counts increase as 6 → 12 → 48 atoms and 18 → 36 → 144, respectively. Each BZ is constructed as the Wigner-Seitz cell of the reciprocal lattice used in the corresponding calculation.

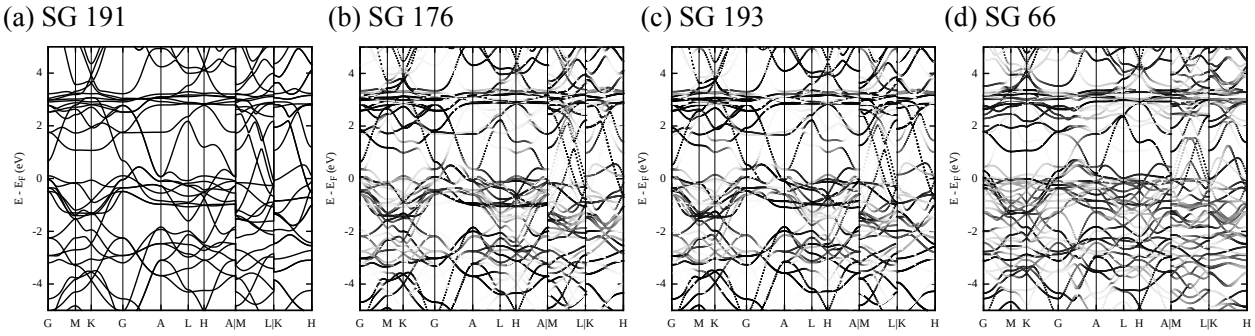


Figure S2.13: The electronic structure of $LaRu_3Si_2$ along high symmetry **k** path in (a) SG 191, and unfolded band structure from (b) SG 176, (c) SG 193, and (d) SG 66 to the same BZ in SG 191. The unfolded bands in three $1 \times 1 \times 2$ phases (b)-(d) are similar to the SG 191 bands in (a), with weak reconstructions at E_F that slightly reduce the DOS at E_F.

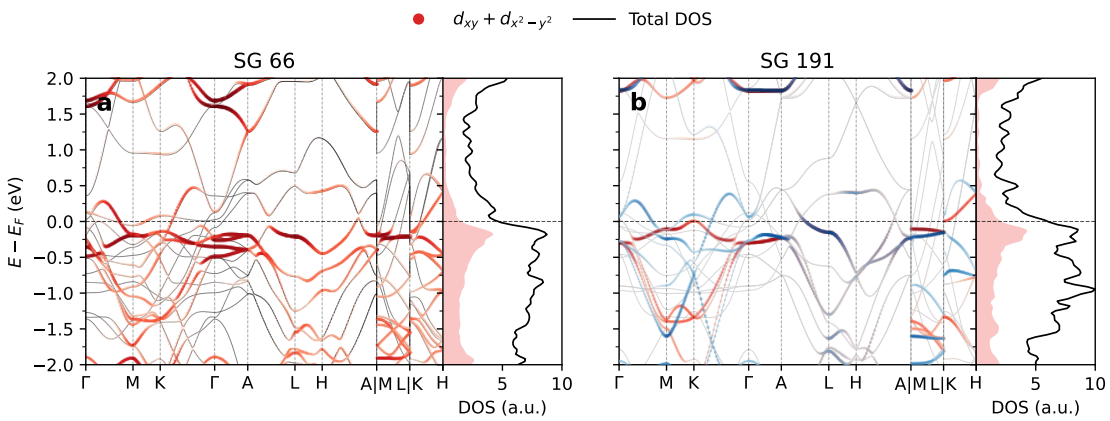


Figure S2.14: Comparison between the electronic band structure of the high-T CDW phase SG 66 and the k_z-folded band structure of SG 191. **a** Electronic band structure of $LaRu_3Si_2$ in SG 66. **b** Electronic band structure of SG 191 folded along the k_z direction into the BZ of SG 66. The color scale denotes the Ru $d_{x^2-y^2}$ orbital weight. The comparison shows that the apparent splitting of the kagome-derived A_g band in SG 66 originates primarily from Brillouin-zone folding: the quasi-flat branch below E_F derives from the SG 191 band on the $k_z = 0$ plane (red dots), whereas the branch crossing E_F originates from the corresponding band on the $k_z = \pi$ plane (blue dots). The symmetry lowering from SG 191 to SG 66 mainly introduces small hybridization gaps at band crossings, while the quasi-FB feature and its associated local DOS peak remain largely preserved.

S2.4.3 Spin-orbit coupling and correlation effects

From the comparison of band structures with and without SOC in Fig. S2.15(a), one can observe that SOC has a minor impact on the overall band structure. Consequently, all subsequent calculations are performed without considering SOC effects. However, band crossings below E_F at about $-0.2\,\text{eV}$ without SOC are observed on the $k_z = 0$ plane between the $d_{x^2-y^2}$ and d_{xz} bands, protected by $\mathcal{M}_z$ symmetry. When SOC is included, this crossing opens a gap, leading to a gapped quasi-FB on the $k_z = 0$ plane. To further explore the role of correlation effects in $LaRu_3Si_2$, eDMFT calculations were conducted using WIEN2K and the RUTGERS EDMFT code [20, 21, 23–25]. The spectral function obtained at $T = 100\,\text{K}$ from the eDMFT calculations aligns closely with the DFT band structure [Fig. S2.15(b) and (c)], as does the FS, indicating weak electron correlation effects and supporting the conclusion that this material is highly itinerant. The estimated mass renormalization factor (quasiparticle weight), $Z = \left[1 - \frac{\partial\,\mathrm{Im}\,\Sigma(i\omega_n)}{\partial i\omega_n}\Big|_{\omega_n\to 0}\right]^{-1} \approx 0.66$, remains relatively small, further supporting the conclusion that SC in $LaRu_3Si_2$ is predominantly mediated by EPC rather than strong electronic correlations. Given these results, correlation effects are not considered in the subsequent analysis of SC in this study.

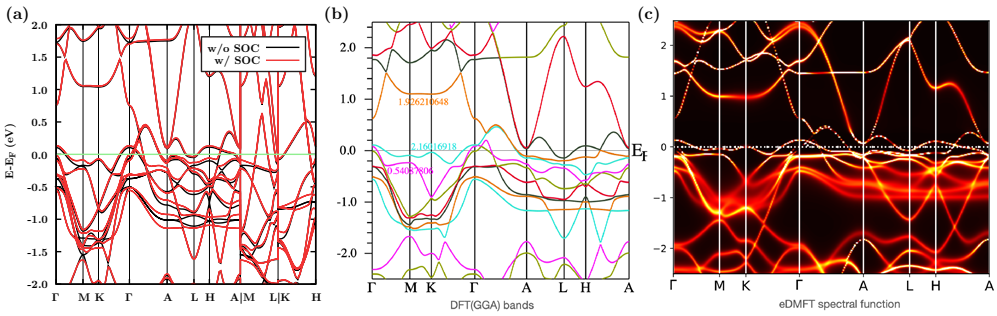


Figure S2.15: (a) The DFT band structure with and without SOC, indicating SOC has negligible effects on the overall band structure and the FSs. (b) The DFT bands with SOC and (c) eDMFT spectral function at $T = 100\,\mathrm{K}$. The eDMFT bands are very close to DFT bands, with the largest mass renormalization Z being 0.66, showing a weak correlation effect in $LaRu_3Si_2$.

S2.5 Electron-phonon coupling and superconductivity

We first define the EPC matrix elements, spectral functions, and the mode-resolved local-axis decomposition, and summarize the evaluation of superconducting properties. We then present the mode-resolved EPC in the reference phases, the superconducting solutions for undoped $LaRu_3Si_2$, and the effects of doping on coupling and stability. The reference phases are the high-temperature SG 191 phase and the intermediate-temperature $1 \times 1 \times 2$ phase in SG 66 ($Cccm$), and doping is treated in the SG 66 phase. The SG 191 phase carries soft phonon modes, and we analyze its superconducting properties by neglecting them, which allows a direct comparison with the results in SG 66.

The chain stops there. We do not treat the lower-temperature SG 51 and SG 55 phases explicitly, and Sections S2.3 and S2.4 justify that choice. Those phases distort mainly the Si framework and leave the Ru kagome net nearly intact [Fig. S2.7**a**–**d**]. Their quasi-flat Ru $d_{x^2-y^2}$ band and its DOS peak survive [Fig. S2.7**e**–**g**], and the low-frequency B_{3u} (local x) kagome Ru branch, which supplies the dominant phonon ingredient of the mechanism, remains the lowest of the three polarizations [Fig. S2.8]. Since the enlarged CDW supercells are substantially more expensive and none of these ingredients change, we compute the coupling in SG 66 and expect the conclusion to carry over.

S2.5.1 EPC matrix elements and spectral functions

First, we review the EPC from first principles. The first-order electron-phonon matrix element of a generic electron-phonon-coupled system can be computed using DFPT as:

$$\left[\tilde{g}(\mathbf{k},\mathbf{k}')\right]_{n'n,\nu} = \frac{1}{\sqrt{2\omega_{\mathbf{k}'-\mathbf{k},\nu}}}\left[g(\mathbf{k},\mathbf{k}')\right]_{n'n,\nu} = \frac{1}{\sqrt{2\omega_{\mathbf{k}'-\mathbf{k},\nu}}}\left\langle\psi_{\mathbf{k}',n'}\middle|\partial_{\mathbf{k}'-\mathbf{k},\nu}\hat{V}\middle|\psi_{\mathbf{k},n}\right\rangle \tag{S2.1}$$

which quantifies a scattering process between the Kohn-Sham eigenstates $|\psi_{\mathbf{k}'n'}\rangle$ and $|\psi_{\mathbf{k}n}\rangle$ computed by DFT, where n is the band index. The matrix elements can be conveniently expressed as $[\tilde{g}(\mathbf{k},\mathbf{q})]_{n'n,\nu}$ instead of $[\tilde{g}(\mathbf{k},\mathbf{k}+\mathbf{q})]_{n'n,\nu}$ using the phonon wavevector $\mathbf{q} = \mathbf{k}' - \mathbf{k}$:

$$[\tilde{g}(\mathbf{k},\mathbf{q})]_{n'n,\nu} = \frac{1}{\sqrt{2\omega_{\mathbf{q},\nu}}}\left\langle\psi_{\mathbf{k}+\mathbf{q},n'}\middle|\partial_{\mathbf{q},\nu}\hat{V}\middle|\psi_{\mathbf{k},n}\right\rangle. \tag{S2.2}$$

In Eq. (S2.2), the operator $\partial_{\mathbf{q},\nu}\hat{V}$ is the derivative of the self-consistent Born-Oppenheimer potential (obtained from DFT, with both electronic and ionic contributions) with respect to a collective ionic displacement corresponding to a phonon with branch index ν and momentum $\mathbf{q}$. The nucleus masses are *already* included in the phonon eigenmodes.

The electron (Σ) and phonon (Π) self-energies at the temperature T for metals and doped semiconductors are given by [17, 56]

$$\Sigma_{\mathbf{k},n}(\omega,T) = \sum_{n',\nu}\int_{\mathrm{BZ}}\frac{\mathrm{d}\mathbf{q}}{\Omega_{\mathrm{BZ}}}\left|[\tilde{g}(\mathbf{k},\mathbf{q})]_{n'n,\nu}\right|^2\left[\frac{n_{\mathbf{q},\nu}(T)+f_{\mathbf{k}+\mathbf{q},n'}(T)}{\omega-\left(\epsilon_{\mathbf{k}+\mathbf{q},n'}-E_F\right)+\omega_{\mathbf{q},\nu}+i\eta}+\frac{n_{\mathbf{q},\nu}(T)+1-f_{\mathbf{k}+\mathbf{q},n'}(T)}{\omega-\left(\epsilon_{\mathbf{k}+\mathbf{q},n'}-E_F\right)-\omega_{\mathbf{q},\nu}+i\eta},\right] \tag{S2.3}$$

$$\Pi_{\mathbf{q},\nu}(\omega_{\mathbf{q},\nu},T) = -2\sum_{n',n}\int_{\mathrm{BZ}}\frac{\mathrm{d}\mathbf{k}}{\Omega_{\mathrm{BZ}}}\left|[\tilde{g}(\mathbf{k},\mathbf{q})]_{n'n,\nu}\right|^2\frac{f_{\mathbf{k},n}(T)-f_{\mathbf{k}+\mathbf{q},n'}(T)}{\epsilon_{\mathbf{k}+\mathbf{q},n'}-\epsilon_{\mathbf{k},n}-\omega_{\mathbf{q},\nu}-i\eta}. \tag{S2.4}$$

In Eq. (S2.4), the factor 2 accounts for the spin degeneracy, E_F is the Fermi energy, $n_{\mathbf{q},\nu}(T) = [\exp(\omega_{\mathbf{q},\nu}/T)-1]^{-1}$ is the Bose-Einstein distribution, $f_{\mathbf{k},n}(T)$ is the electronic (Fermi-Dirac) occupation at wavevector $\mathbf{k}$ and band n, and η is a small positive real parameter which ensures the

correct analytical structure of the self-energies and avoids numerical instabilities. The physical interpretation of η is related to the finite lifetime of the electronic states. The integrals extend over the BZ of volume Ω_{BZ}.

The electron and phonon linewidths can be obtained from the imaginary part of the electron ($\Sigma'' = \mathrm{Im}\,\Sigma$) and phonon ($\Pi'' = \mathrm{Im}\,\Pi$) self-energies [16]:

$$\begin{aligned}\Sigma''_{\mathbf{k},n}(\omega,T) = \pi \sum_{n',\nu} \int_{\mathrm{BZ}} \frac{\mathrm{d}\mathbf{q}}{\Omega_{\mathrm{BZ}}} \left|[\tilde{g}(\mathbf{k},\mathbf{q})]_{n'n,\nu}\right|^2 \Big\{ \big[n_{\mathbf{q},\nu}(T) + f_{\mathbf{k}+\mathbf{q},n'}(T)\big]\delta(\omega - (\epsilon_{\mathbf{k}+\mathbf{q},n'} - E_F) + \omega_{\mathbf{q},\nu}) \\ + \big[n_{\mathbf{q},\nu}(T) + 1 - f_{\mathbf{k}+\mathbf{q},n'}(T)\big]\delta(\omega - (\epsilon_{\mathbf{k}+\mathbf{q},n'} - E_F) - \omega_{\mathbf{q},\nu})\Big\}\end{aligned} \tag{S2.5}$$

$$\gamma_{\mathbf{q},\nu} = \Pi''_{\mathbf{q},\nu}(\omega_{\mathbf{q},\nu},T) = 2\pi \sum_{n',n} \int_{\mathrm{BZ}} \frac{\mathrm{d}\mathbf{k}}{\Omega_{\mathrm{BZ}}} \left|[\tilde{g}(\mathbf{k},\mathbf{q})]_{n'n,\nu}\right|^2 \big[f_{\mathbf{k},n}(T) - f_{\mathbf{k}+\mathbf{q},n'}(T)\big]\delta\big(\epsilon_{\mathbf{k}+\mathbf{q},n'} - \epsilon_{\mathbf{k},n} - \omega_{\mathbf{q},\nu}\big). \tag{S2.6}$$

Under the double-delta approximation (see derivation at the end of this section), the phonon linewidth $\gamma_{\mathbf{q},\nu}$ is expressed as

$$\gamma_{\mathbf{q},\nu} = 2\pi\omega_{\mathbf{q},\nu} \sum_{n',n} \int_{\mathrm{BZ}} \frac{\mathrm{d}\mathbf{k}}{\Omega_{\mathrm{BZ}}} |[\tilde{g}(\mathbf{k},\mathbf{q})]_{n'n,\nu}|^2 \delta(\epsilon_{\mathbf{k},n} - E_F)\delta(\epsilon_{\mathbf{k}+\mathbf{q},n'} - E_F) \tag{S2.7}$$

Finally, the EPC strength associated with a specific phonon mode ν and wavevector $\mathbf{q}$ is:

$$\begin{aligned}\lambda_{\mathbf{q},\nu} &= \frac{1}{D(E_F)\omega_{\mathbf{q},\nu}} \sum_{n'n} \int_{\mathrm{BZ}} \frac{\mathrm{d}\mathbf{k}}{\Omega_{\mathrm{BZ}}} \left|[\tilde{g}(\mathbf{k},\mathbf{q})]_{n'n,\nu}\right|^2 \delta(\epsilon_{\mathbf{k},n} - E_F)\delta\big(\epsilon_{\mathbf{k}+\mathbf{q},n'} - E_F\big) \\ &= \frac{\gamma_{\mathbf{q},\nu}}{2\pi D(E_F)\omega^2_{\mathbf{q},\nu}},\end{aligned} \tag{S2.8}$$

where $D(E_F)$ is the DOS per spin at the Fermi level. From Eq. (S2.2), $[\tilde{g}(\mathbf{k},\mathbf{q})]_{n'n,\nu}$ is proportional to $\frac{1}{\sqrt{\omega_{\mathbf{q},\nu}}}$, and the integration of two delta-functions gives $D(E_F)^2$, thus

$$\lambda_{\mathbf{q},\nu} \propto \frac{D(E_F)}{\omega^2_{\mathbf{q},\nu}}. \tag{S2.9}$$

Therefore, a low phonon energy with a finite EPC matrix element $\tilde{g}$ will result in a considerably high EPC $\lambda_{\mathbf{q},\nu}$. The total EPC constant λ is the BZ average over the phonon-resolved $\lambda_{\mathbf{q},\nu}$:

$$\lambda = \sum_{\nu} \int_{\mathrm{BZ}} \frac{\mathrm{d}\mathbf{q}}{\Omega_{\mathrm{BZ}}} \lambda_{\mathbf{q},\nu} \tag{S2.10}$$

The Eliashberg spectral function $\alpha^2F(\omega)$ is defined as

$$\begin{aligned}\alpha^2F(\omega) &= \frac{1}{2}\sum_{\nu} \int_{\mathrm{BZ}} \frac{\mathrm{d}\mathbf{q}}{\Omega_{\mathrm{BZ}}} \omega_{\mathbf{q}\nu}\lambda_{\mathbf{q}\nu}\delta(\omega - \omega_{\mathbf{q}\nu}) \\ &= \frac{1}{2}\sum_{\nu} \int_{\mathrm{BZ}} \frac{\mathrm{d}\mathbf{q}}{\Omega_{\mathrm{BZ}}} \frac{\gamma_{\mathbf{q},\nu}}{2\pi D(E_F)\omega_{\mathbf{q},\nu}} \delta(\omega - \omega_{\mathbf{q}\nu}).\end{aligned} \tag{S2.11}$$

This function describes the distribution of the EPC over phonon frequencies. An equivalent definition of total EPC constant λ is based on $\alpha^2F(\omega)$:

$$\lambda = 2\int_0^{\infty} \mathrm{d}\omega\, \frac{\alpha^2F(\omega)}{\omega} \tag{S2.12}$$

The double-delta approximation of phonon linewidth. The double-delta approximation of phonon linewidth makes the assumption that the phonon frequency $\omega_{\mathbf{q}\nu}$ is small, so one only needs to consider the electron states close to the Fermi level for the SC properties. We start from

$$\gamma_{\mathbf{q},\nu} = -2\,\mathrm{Im}\sum_{m,n}\int_{\mathrm{BZ}}\frac{\mathrm{d}\mathbf{k}}{\Omega_{\mathrm{BZ}}}\left|[\tilde{g}(\mathbf{k},\mathbf{q})]_{mn,\nu}\right|^2\frac{f_{\mathbf{k},n}(T)-f_{\mathbf{k}+\mathbf{q},m}(T)}{\epsilon_{\mathbf{k}+\mathbf{q},m}-\epsilon_{\mathbf{k},n}-\omega_{\mathbf{q},\nu}-i\eta}. \tag{S2.13}$$

The Fermi-Dirac functions can be approximated as

$$f_{\mathbf{k},n}(T)-f_{\mathbf{k}+\mathbf{q},m}(T) = -(\epsilon_{\mathbf{k}+\mathbf{q},m}-\epsilon_{\mathbf{k},n})f'_{\mathbf{k},n}(T) = (\epsilon_{\mathbf{k}+\mathbf{q},m}-\epsilon_{\mathbf{k},n})\delta(\epsilon_{\mathbf{k},n}-E_F). \tag{S2.14}$$

Then

$$\gamma_{\mathbf{q},\nu} = -2\,\mathrm{Im}\sum_{m,n}\int_{\mathrm{BZ}}\frac{\mathrm{d}\mathbf{k}}{\Omega_{\mathrm{BZ}}}\left|[\tilde{g}(\mathbf{k},\mathbf{q})]_{mn,\nu}\right|^2\left(\frac{\epsilon_{\mathbf{k}+\mathbf{q},m}-\epsilon_{\mathbf{k},n}-\omega_{\mathbf{q},\nu}}{\epsilon_{\mathbf{k}+\mathbf{q},m}-\epsilon_{\mathbf{k},n}-\omega_{\mathbf{q},\nu}-i\eta}+\frac{\omega_{\mathbf{q},\nu}}{\epsilon_{\mathbf{k}+\mathbf{q},m}-\epsilon_{\mathbf{k},n}-\omega_{\mathbf{q},\nu}-i\eta}\right)\delta(\epsilon_{\mathbf{k},n}-E_F) \tag{S2.15}$$

The imaginary part of the first term vanishes when $\eta\to 0$. Thus

$$\begin{aligned}\gamma_{\mathbf{q},\nu} &\approx 2\pi\sum_{m,n}\int_{\mathrm{BZ}}\frac{\mathrm{d}\mathbf{k}}{\Omega_{\mathrm{BZ}}}\left|[\tilde{g}(\mathbf{k},\mathbf{q})]_{mn,\nu}\right|^2\omega_{\mathbf{q},\nu}\delta(\epsilon_{\mathbf{k}+\mathbf{q},m}-\epsilon_{\mathbf{k},n}-\omega_{\mathbf{q},\nu}-E_F)\delta(\epsilon_{\mathbf{k},n}-E_F)\\ &\approx 2\pi\omega_{\mathbf{q},\nu}\int_{\mathrm{BZ}}\frac{\mathrm{d}\mathbf{k}}{\Omega_{\mathrm{BZ}}}\left|[\tilde{g}(\mathbf{k},\mathbf{q})]_{mn,\nu}\right|^2\delta(\epsilon_{\mathbf{k}+\mathbf{q},m}-E_F)\delta(\epsilon_{\mathbf{k},n}-E_F)\end{aligned} \tag{S2.16}$$

The second approximation follows when $\omega_{\mathbf{q},\nu}$ is negligible. Thus we arrive at the expression of phonon linewidth in the double-delta approximation.

S2.5.2 Local-axis decomposition of the electron-phonon coupling

We use phonon eigenvector weights to resolve whole-mode EPC values by atomic species and local displacement direction, focusing on the Ru kagome channels.

Local frames and channel weights. Let $e_{\kappa\alpha,\nu}(\mathbf{q})$ denote the eigenvectors of the mass-weighted dynamical matrix, where κ labels atoms and $\alpha\in\{X,Y,Z\}$ labels Cartesian components. Their normalization and completeness are

$$\sum_{\kappa\alpha}|e_{\kappa\alpha,\nu}(\mathbf{q})|^2 = 1, \tag{S2.17}$$

$$\sum_{\nu}e_{\kappa\alpha,\nu}(\mathbf{q})e^*_{\kappa'\beta,\nu}(\mathbf{q}) = \delta_{\kappa\kappa'}\delta_{\alpha\beta}. \tag{S2.18}$$

For each atom, we define an orthonormal local frame $\{\hat{\mathbf{e}}^\kappa_x,\hat{\mathbf{e}}^\kappa_y,\hat{\mathbf{e}}^\kappa_z\}$. On Ru, the local x and y axes point toward the kagome hexagon and triangle centres, respectively, and z is parallel to the crystallographic c axis (Fig. S2.3). These channels are labelled B_{3u}, B_{2u}, and B_{1u} using the local site-symmetry convention of Table S2.1. On La and Si, we use the global Cartesian frame.

For species s and axis c, the channel weight is

$$W_{s,c}(\mathbf{q},\nu) = \sum_{\kappa\in s}|\hat{\mathbf{e}}^\kappa_c\cdot\mathbf{e}_{\kappa,\nu}(\mathbf{q})|^2. \tag{S2.19}$$

Orthonormality of the local frames, together with the normalization and completeness of the eigenvectors, gives

$$\sum_{s,c} W_{s,c}(\mathbf{q},\nu) = 1, \tag{S2.20}$$

$$\sum_{\nu} W_{s,c}(\mathbf{q},\nu) = N_s, \tag{S2.21}$$

where N_s is the number of atoms of species s in the primitive cell. Thus, the weights partition each mode and give equal total mode weight to the three axes of a given species.

Projected spectral functions. The projected Eliashberg function, EPC constant, and phonon density of states are

$$\alpha^2 F_{s,c}(\omega) = \frac{1}{2}\sum_{\nu}\int_{\mathrm{BZ}} \frac{\mathrm{d}\mathbf{q}}{\Omega_{\mathrm{BZ}}} W_{s,c}(\mathbf{q},\nu)\,\omega_{\mathbf{q},\nu}\lambda_{\mathbf{q},\nu}\,\delta(\omega-\omega_{\mathbf{q},\nu}), \tag{S2.22}$$

$$\lambda_{s,c} = \sum_{\nu}\int_{\mathrm{BZ}} \frac{\mathrm{d}\mathbf{q}}{\Omega_{\mathrm{BZ}}} W_{s,c}(\mathbf{q},\nu)\lambda_{\mathbf{q},\nu} = 2\int_0^\infty \frac{\mathrm{d}\omega}{\omega}\alpha^2 F_{s,c}(\omega), \tag{S2.23}$$

$$F_{s,c}(\omega) = \sum_{\nu}\int_{\mathrm{BZ}} \frac{\mathrm{d}\mathbf{q}}{\Omega_{\mathrm{BZ}}} W_{s,c}(\mathbf{q},\nu)\,\delta(\omega-\omega_{\mathbf{q},\nu}). \tag{S2.24}$$

By Eq. (S2.20), summing over species and axes recovers the corresponding unprojected quantities. For a stable phonon spectrum, Eq. (S2.21) also gives

$$\int_0^\infty \mathrm{d}\omega\; F_{s,c}(\omega) = N_s, \tag{S2.25}$$

when all branches are counted. Omitting the three zero-frequency acoustic modes at Γ on the $12\times12\times8$ $\mathbf{q}$ mesh reduces this integral from $N_{\mathrm{Ru}} = 6$ to 5.99947 for each Ru axis. Where $F_{s,c}(\omega) > 0$, we also define the phonon-DOS-normalized spectral function

$$\alpha^2_{s,c}(\omega) = \frac{\alpha^2 F_{s,c}(\omega)}{F_{s,c}(\omega)}. \tag{S2.26}$$

This removes the projected phonon DOS factor but retains the weighting of whole-mode EPC values.

Frequency moments and phonon linewidths. Define the spectral moments

$$\begin{aligned} M_n^{(s,c)} &\equiv 2\int_0^\infty \mathrm{d}\omega\; \alpha^2 F_{s,c}(\omega)\omega^{n-1} \\ &= \sum_{\nu}\int_{\mathrm{BZ}} \frac{\mathrm{d}\mathbf{q}}{\Omega_{\mathrm{BZ}}} W_{s,c}(\mathbf{q},\nu)\lambda_{\mathbf{q},\nu}\omega^n_{\mathbf{q},\nu}, \end{aligned} \tag{S2.27}$$

so that $M_0^{(s,c)} = \lambda_{s,c}$. The corresponding λ-weighted root-mean-square frequency is

$$\bar{\omega}_{2,s,c} = \left(\frac{M_2^{(s,c)}}{\lambda_{s,c}}\right)^{1/2}. \tag{S2.28}$$

Using the vertex normalization $\tilde{g} = g/\sqrt{2\omega_{\mathbf{q},\nu}}$ of Eq. (S2.2), the double-delta linewidth in Eq. (S2.7) becomes

$$\gamma_{\mathbf{q},\nu} = \pi \sum_{n',n} \int_{\mathrm{BZ}} \frac{\mathrm{d}\mathbf{k}}{\Omega_{\mathrm{BZ}}} |[g(\mathbf{k},\mathbf{q})]_{n'n,\nu}|^2 \times \delta(\epsilon_{\mathbf{k},n} - E_F)\delta(\epsilon_{\mathbf{k}+\mathbf{q},n'} - E_F), \tag{S2.29}$$

where g is the unscaled mode vertex of Eq. (S2.1). The explicit frequency prefactor therefore cancels. Combining this result with $\lambda_{\mathbf{q},\nu} = \gamma_{\mathbf{q},\nu}/[2\pi D(E_F)\omega^2_{\mathbf{q},\nu}]$ gives

$$M_2^{(s,c)} = \frac{1}{2\pi D(E_F)} \sum_{\nu} \int_{\mathrm{BZ}} \frac{\mathrm{d}\mathbf{q}}{\Omega_{\mathrm{BZ}}} W_{s,c}(\mathbf{q},\nu)\gamma_{\mathbf{q},\nu}. \tag{S2.30}$$

Thus, $M_2^{(s,c)}$ measures the projected linewidth sum without the explicit $\omega^{-2}_{\mathbf{q},\nu}$ factor in $\lambda_{s,c}$, while retaining eigenvector and electronic-phase-space weighting.

Comparison of the Ru channels. The projected quantities for undoped $LaRu_3Si_2$ in SG 66 are listed in Table S2.3. The two in-plane channels satisfy

$$\frac{\lambda_{\mathrm{Ru},x}}{\lambda_{\mathrm{Ru},y}} = \frac{M_2^{(\mathrm{Ru},x)}}{M_2^{(\mathrm{Ru},y)}} \left(\frac{\bar{\omega}_{2,\mathrm{Ru},y}}{\bar{\omega}_{2,\mathrm{Ru},x}}\right)^2. \tag{S2.31}$$

Numerically, $\lambda_{\mathrm{Ru},x}/\lambda_{\mathrm{Ru},y} \simeq 3.16$, with a projected linewidth ratio of 0.783 and a squared characteristic-frequency ratio of 4.04. Within this partition, the larger x-projected EPC is therefore associated with its lower characteristic frequency, not a larger projected linewidth sum. This is consistent with the separate analyses of the phonon frequencies and displacement-dependent coupling in Sections S3.1.2 and S3.2.

Table S2.3: Ru local-axis projections for undoped $LaRu_3Si_2$ in SG 66, calculated on $12 \times 12 \times 8$ $\mathbf{q}$ and $24 \times 24 \times 16$ $\mathbf{k}$ meshes. Spectral moments were evaluated directly from discrete mode sums rather than broadened phonon spectra; the three zero-frequency acoustic modes at Γ were omitted.

c	$\lambda_{\mathrm{Ru},c}$	$M_2^{(\mathrm{Ru},c)}/\mathrm{meV}^2$	$\bar{\omega}_{2,\mathrm{Ru},c}/\mathrm{meV}$
x (B_{3u})	0.3147	32.47	10.16
y (B_{2u})	0.0995	41.45	20.41
z (B_{1u})	0.1658	33.81	14.28

The three Ru projections sum to $\lambda_{\mathrm{Ru}} = 0.580$, approximately 64% of the total $\lambda = 0.910$. This weighting scheme does not isolate the EPC generated by a single displacement component or separate interference terms within mixed modes. The frequency factorization therefore characterizes the projected spectrum rather than independently determining directional deformation potentials.

S2.5.3 Evaluation of superconducting properties

Critical-temperature estimate. We estimate T_c using the Allen-Dynes modification of the McMillan formula [31, 32, 57], with the strong-coupling and spectral-shape correction factors set to unity:

$$k_{\mathrm{B}}T_c = \frac{\omega_{\log}}{1.2} \exp\left[-\frac{1.04(1+\lambda)}{\lambda - \mu^*(1+0.62\lambda)}\right]. \tag{S2.32}$$

Frequencies are expressed in energy units ($\hbar = 1$). Here, μ^* is the effective Coulomb pseudopotential, λ is the dimensionless EPC constant defined in Eq. (S2.12), and $\omega_{\log}$ is the logarithmic phonon average,

$$\omega_{\log} = \exp\left[\frac{2}{\lambda}\int_0^\infty \frac{\mathrm{d}\omega}{\omega}\alpha^2F(\omega)\ln\omega\right]. \tag{S2.33}$$

Isotropic Migdal-Eliashberg equations. We also solve the isotropic Migdal-Eliashberg equations directly to obtain T_c and the temperature-dependent gap without the empirical T_c fit [58, 59]. Within the constant-DOS approximation, the imaginary-axis equations for the renormalization function $Z(i\omega_n)$ and gap function $\Delta(i\omega_n)$ are

$$Z(i\omega_n) = 1 + \frac{\pi k_{\mathrm{B}}T}{\omega_n}\sum_{|\omega_{n'}|\le\omega_{\mathrm{c}}} \frac{\omega_{n'}}{\sqrt{\omega_{n'}^2 + \Delta^2(i\omega_{n'})}}\lambda(\omega_n - \omega_{n'}), \tag{S2.34}$$

$$Z(i\omega_n)\Delta(i\omega_n) = \pi k_{\mathrm{B}}T\sum_{|\omega_{n'}|\le\omega_{\mathrm{c}}} \frac{\Delta(i\omega_{n'})}{\sqrt{\omega_{n'}^2 + \Delta^2(i\omega_{n'})}}[\lambda(\omega_n - \omega_{n'}) - \mu^*]. \tag{S2.35}$$

Here, $\omega_n = (2n+1)\pi k_{\mathrm{B}}T$ are the fermionic Matsubara frequencies, and the frequency-dependent kernel is obtained from the Eliashberg spectral function as

$$\lambda(\omega_n - \omega_{n'}) = \int_0^\infty \mathrm{d}\omega\ \frac{2\omega\,\alpha^2F(\omega)}{\omega^2 + (\omega_n - \omega_{n'})^2}. \tag{S2.36}$$

At zero frequency transfer, this kernel reduces to the total EPC constant in Eq. (S2.12). The Matsubara sums and Coulomb term share the cutoff ω_{c}, at which μ^* is defined. Both approaches use the same $\alpha^2F(\omega)$, but comparing their T_c estimates requires a consistent Coulomb-pseudopotential convention. We determine T_c from the disappearance of the nonzero gap solution and denote $\Delta(i\omega_0)$ at the lowest calculated temperature by Δ_0.

Quasiparticle density of states. The converged imaginary-axis gap is analytically continued using Padé approximants to obtain the complex real-frequency gap $\Delta(\omega)$ [59]. We evaluate the numerically broadened superconducting DOS as

$$\frac{N_S(\omega)}{N_F} = \mathrm{Re}\left[\frac{\omega + i\delta}{\sqrt{(\omega + i\delta)^2 - \Delta^2(\omega)}}\right], \tag{S2.37}$$

where N_F is the normal-state DOS at E_F and δ is a numerical broadening set equal to the spacing of the tabulated $\alpha^2F(\omega)$ grid. This broadening smooths the coherence peaks and introduces artificial subgap spectral weight; it is not a fitted quasiparticle damping rate. In the weak-damping limit, the spectral gap edge is approximately the lowest positive solution of $\omega = \mathrm{Re}\,\Delta(\omega)$ and is distinct from the Matsubara-axis quantity Δ_0.

S2.5.4 Mode-resolved EPC in the reference phases

Figs. S2.16 and S2.17 give the EPC strength $\lambda_{\mathbf{q},\nu}$ along high-symmetry lines, the isotropic Eliashberg spectral function $\alpha^2F(\omega)$, and the total and orbital-resolved integrated EPC $\lambda(\omega)$ for the SG 191 and SG 66 phases. In SG 191, λ is dominated by low-frequency phonons, with the Ru-x phonon of the kagome local frame [Fig. S2.3] the primary contributor, and the three soft modes on the $q_z = \pi$ plane are excluded because they are unstable. In SG 66, where the soft phonons are eliminated, the

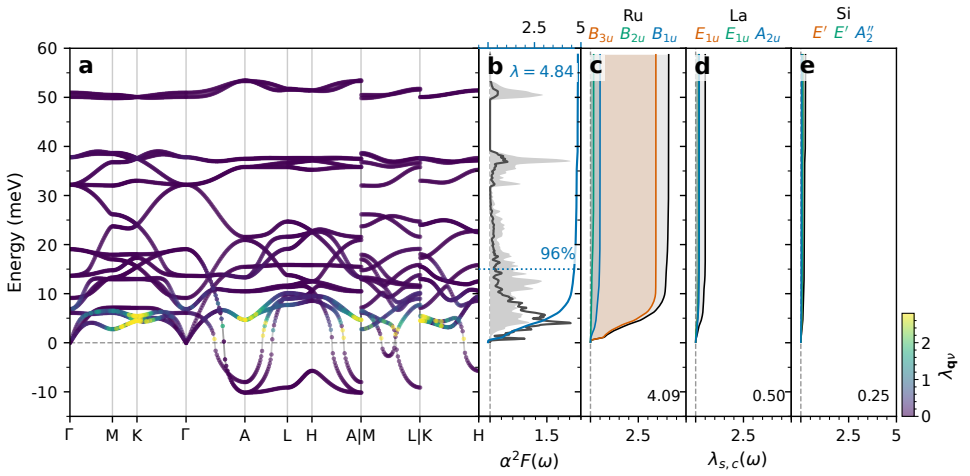


Figure S2.16: Mode- and axis-resolved EPC in undoped $LaRu_3Si_2$ in the SG 191 ($P6/mmm$) phase, plotted on the same energy scale as Fig. S2.17. **a** Mode-resolved coupling strengths $\lambda_{\mathbf{q}\nu}$ along the high-symmetry path in Fig. S2.5**a**. The unstable branch along A–L–H reaches -10.07 meV. Imaginary-frequency modes are assigned zero coupling for plotting and excluded from all EPC sums: 367 of 8262 modes along the path and 1414 of 41472 modes on the mesh. The colour scale saturates at $\lambda = 2.80$, the 99th percentile of the stable-mode values; the maximum is $\lambda = 47.5$ along H–A. **b** Eliashberg spectral function $\alpha^2F(\omega)$ (dark line), phonon DOS (grey shading, scaled to the same peak height), and cumulative EPC strength $\lambda(\omega)$ (blue, upper axis). Phonons below 15 meV (dotted line) contribute 96% of the stable-mode total $\lambda = 4.84$, which differs from the coupling tabulated in Table S2.4. **c**–**e** Element- and axis-resolved cumulative EPC strengths $\lambda_{s,c}(\omega)$, defined in Eq. (S2.19), on the same horizontal scale as **b**. Black curves show the element totals, and shaded regions show the directional contributions in the local Ru frames of Fig. S2.3 and the global Cartesian frame for La and Si. The Ru, La, and Si contributions are 4.09, 0.50, and 0.25, respectively; the Ru contribution comprises 3.42, 0.17, and 0.50 along the local x, y, and z axes. Panels **b**–**e** are Brillouin-zone averages over a uniform $12 \times 12 \times 16$ **q** mesh with 0.2 meV Gaussian broadening, rather than sums along the path in **a**.

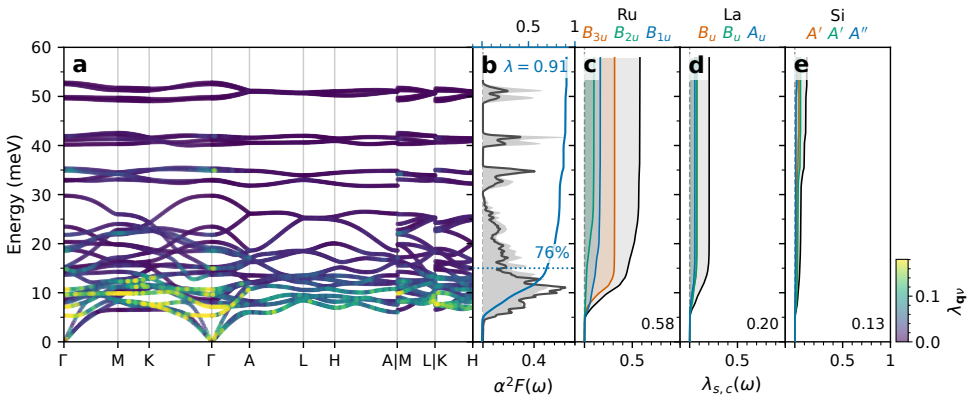


Figure S2.17: Mode- and axis-resolved EPC in the SG 66 ($Cccm$) phase of $LaRu_3Si_2$. **a** Mode-resolved EPC along the high-symmetry path in Fig. S2.4, with colours indicating the coupling strengths $\lambda_{\mathbf{q},\nu}$. **b** Eliashberg spectral function $\alpha^2F(\omega)$ (dark line), phonon DOS (grey shading, scaled to the same peak height), and cumulative EPC strength $\lambda(\omega)$ (blue, upper axis). Phonons below 15 meV (dotted line) contribute 76% of the total $\lambda = 0.910$. **c**–**e** Element- and axis-resolved cumulative EPC strengths $\lambda_{s,c}(\omega)$, defined in Eq. (S2.19), using the plotting conventions of Fig. S2.16. Ru displacements are resolved along the local axes of Fig. S2.3, whereas La ($4d$) and Si ($8l$) displacements are resolved along the global Cartesian axes. The Ru channels retain the parent SG 191 $3g$ labels B_{3u} (x), B_{2u} (y), and B_{1u} (z) as polarization labels rather than SG 66 site-symmetry assignments. The Ru, La, and Si contributions to λ are 0.58, 0.20, and 0.13, respectively. Panels **b**–**e** are Brillouin-zone averages over a uniform $12 \times 12 \times 8$ **q** mesh with 0.2 meV Gaussian broadening, rather than sums along the path in **a**.

strong Ru-x contribution persists: the Ru-y and Ru-z contributions grow with the hybridization that symmetry breaking allows, but Ru-x remains dominant in the orbital-resolved $\lambda(\omega)$. Fig. S2.18 shows this channel by channel, on the dispersion of both phases and on the Brillouin-zone averaged linewidth spectra beside it. The soft modes of SG 191 also render its EPC ill-defined, and the tabulated $\lambda = 4.788$, 5.3 times the SG 66 value of 0.9089, is an artefact of the imaginary one-dimensional A_4^+ mode rather than a physical coupling, as the caption of Table S2.4 sets out in full.

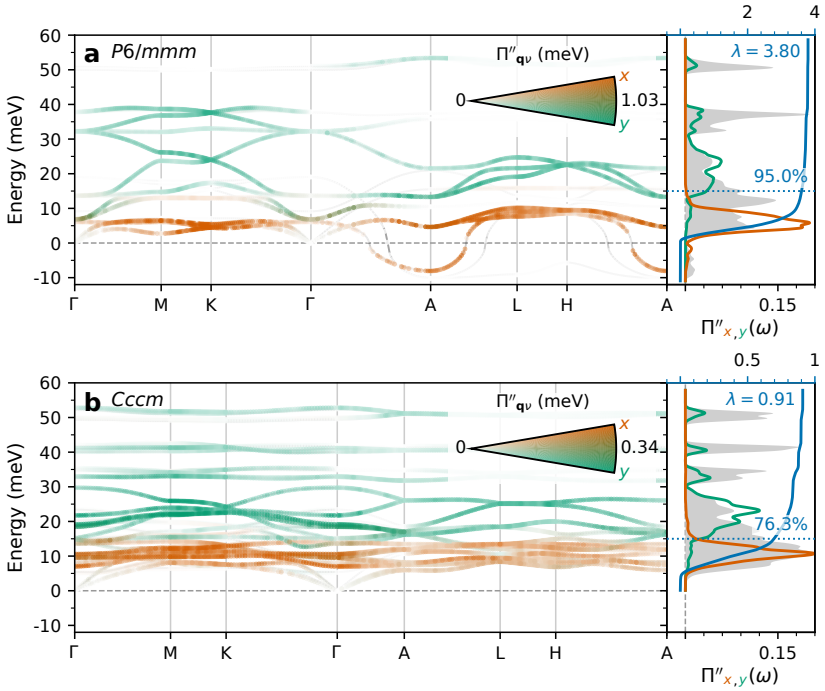


Figure S2.18: Ru local-axis character and projected phonon linewidths in $LaRu_3Si_2$: **a** SG 191 ($P6/mmm$) and **b** SG 66 ($Cccm$). Here $W_c \equiv W_{\mathrm{Ru},c}$ is defined in Eq. (S2.19); all channel-resolved quantities refer to the Ru sublattice. Hue encodes $W_x/(W_x+W_y)$, with orange and green denoting the local x (B_{3u}) and y (B_{2u}) channels, respectively (Fig. S2.3). Lightness encodes the weighted linewidth $\Pi''_{\mathbf{q}\nu}(W_x+W_y)$, with white at zero and a power-law exponent of 0.55. The colour scales are capped at the panel-specific 98th percentiles, 1.03 meV in **a** and 0.34 meV in **b**; colour intensities are therefore not directly comparable between panels. The inset keys encode linewidth magnitude by radius and channel mixing by opening angle. Side panels show the projected linewidth spectra $\Pi''_x(\omega)$ and $\Pi''_y(\omega)$ in the corresponding channel colours, the phonon DOS in grey, and the cumulative $\lambda(\omega)$ in blue (top axis). Dotted lines mark 15 meV. These spectra are Brillouin-zone averages on uniform $18\times18\times18$ and $12\times12\times8$ $\mathbf{q}$ meshes for **a** and **b**, respectively, with 0.5 meV Gaussian broadening. Imaginary frequencies are displayed as negative values. In **a**, imaginary modes constitute 3.4% of the sampled modes and are included in the linewidth plots but excluded from $\lambda(\omega)$. The resulting $\lambda = 3.80$ is a stable-mode partial sum, not a physical total EPC constant for the unstable structure. For the dynamically stable SG 66 phase, $\lambda = 0.91$ (Table S2.4).

S2.5.5 Superconductivity in undoped $LaRu_3Si_2$

Table S2.4 summarizes the integrated EPC strength λ, logarithmic average phonon frequency $\omega_{\log}$, and the superconducting transition temperature T_c, calculated using the Allen-Dynes modified McMillan equation [Eq. (S2.32)] [31, 32, 57] with $\mu^* = 0.10$. In the dynamically stable SG 66 phase, we obtain a theoretical T_c of 8.0 K, in excellent agreement with the experimentally reported $T_c \sim 7.8$ K [35–38, 40, 50, 52, 60–67].

The superconducting gaps of SG 191 and SG 66, obtained by solving the anisotropic Migdal-Eliashberg equations on the imaginary axis [59] followed by Padé analytic continuation, are shown in

Table S2.4: The superconducting quantities of undoped $LaRu_3Si_2$ in the two high-temperature phases. The SG 191 entry is not a physical coupling. That phase carries soft modes (Fig. S2.5**a**), and since $\lambda_{\mathbf{q},\nu} \propto 1/\omega^2_{\mathbf{q},\nu}$ every anomalously soft branch inflates the sum, so the tabulated $\lambda = 4.788$ is an artefact of the imaginary one-dimensional A_4^+ mode rather than a measure of the coupling. With higher electronic temperature (such as 0.15 Ry or 0.3 Ry), the 1D soft mode A_4^+ will be eliminated in SG 191 (Fig. S2.4), and λ reduces to 1.74 or 0.75. Thus we conclude that the large λ in SG 191 is a result of the soft modes, and will be reduced to a similar value as SG 66 once all soft modes are removed. The DOS at E_F, $D(E_F)$, is divided by 2 in SG 66 for comparison with the SG 191 phase.

Phase	$D(E_F)$/states spin^{-1} eV^{-1} unit cell^{-1}	λ	$\omega_{\log}$/K	T_c/K
SG 191 ($P6/mmm$)	2.855	4.788	42.11	8.911
SG 66 ($Cccm$)	2.206	0.9089	133.81	7.973

Fig. S2.11**f,l**, respectively. In both phases, the gap is largest on FS regions with predominantly local $d_{x^2-y^2}$ character and smallest where d_{z^2} character dominates [Fig. S2.11]. In SG 191, the gap on the $d_{x^2-y^2}$-dominated sheets is approximately three times larger than on the other sheets, qualitatively consistent with the reported two-gap behavior of $LaRu_3Si_2$ [40]. The distortion preserves this orbital dependence but reduces the area-weighted mean gap in SG 66. The enhanced gap on the $d_{x^2-y^2}$-dominated sheets supports the participation of the kagome quasi-FB states in superconductivity.

The SG 66 gap shown in Fig. 3**a** of the main text is obtained using matching $24 \times 24 \times 16$ fine electron and phonon meshes, avoiding the mesh partitioning described above. The calculation includes 15082 electronic states within 1.0 eV of E_F and uses a Fermi-surface broadening of 20 meV, a Matsubara cutoff of 0.1 eV, and $\mu^* = 0.10$. At $T = 2.5$ K, the gap ranges from 0.86 to 2.01 meV, with an FS-area-weighted mean of 1.37 meV. The area-weighted mean gaps for the six bands crossing E_F range from 1.13 to 1.53 meV. These values are used in the main text.

We additionally solve the isotropic Migdal-Eliashberg equations [Eqs. (S2.34) and (S2.35)] using the SG 66 $\alpha^2F(\omega)$, with $\mu^* = 0.10$ defined at the cutoff $\omega_c = 100$ meV [Fig. S2.19]. The solution yields $T_c = 8.94$ K and a low-temperature Matsubara gap $\Delta_0 = 1.494$ meV, giving $2\Delta_0/(k_B T_c) = 3.88$, above the weak-coupling Bardeen-Cooper-Schrieffer (BCS) value of 3.53. The calculated gap exceeds the BCS interpolation by approximately 3% between 5.5 and 8.5 K. The low-frequency renormalization function, $Z(i\omega_0) = 1.857$, is close to the normal-state reference value $1 + \lambda = 1.909$. The corresponding quasiparticle DOS indicates a gap edge near 1.51 meV, while its subgap spectral weight and coherence-peak height depend on the numerical broadening δ in Eq. (S2.37). The isotropic solution provides a reference gap scale and temperature dependence, whereas the anisotropic calculations resolve the variation across the FS.

S2.5.6 Doping dependence and competing instabilities

Given that the FB is located just below the E_F at approximately 150 meV [Fig. S2.10**f** and **l**], it is natural to explore the effects of doping on SC. To investigate this, *ab initio* calculations were performed with a varied number of valence electrons (together with a homogeneous background charge to maintain charge neutrality) to simulate doping. First, we examine the structural stability of $LaRu_3Si_2$ under hole doping. As shown in Fig. S2.20**b**, hole doping generally induces structural instability starting from two holes per unit cell, as indicated by the progressive softening of phonon modes with increasing doping levels. Moreover, the energy difference between the paramagnetic and ferromagnetic states as a function of doping level reveals that hole doping beyond two holes

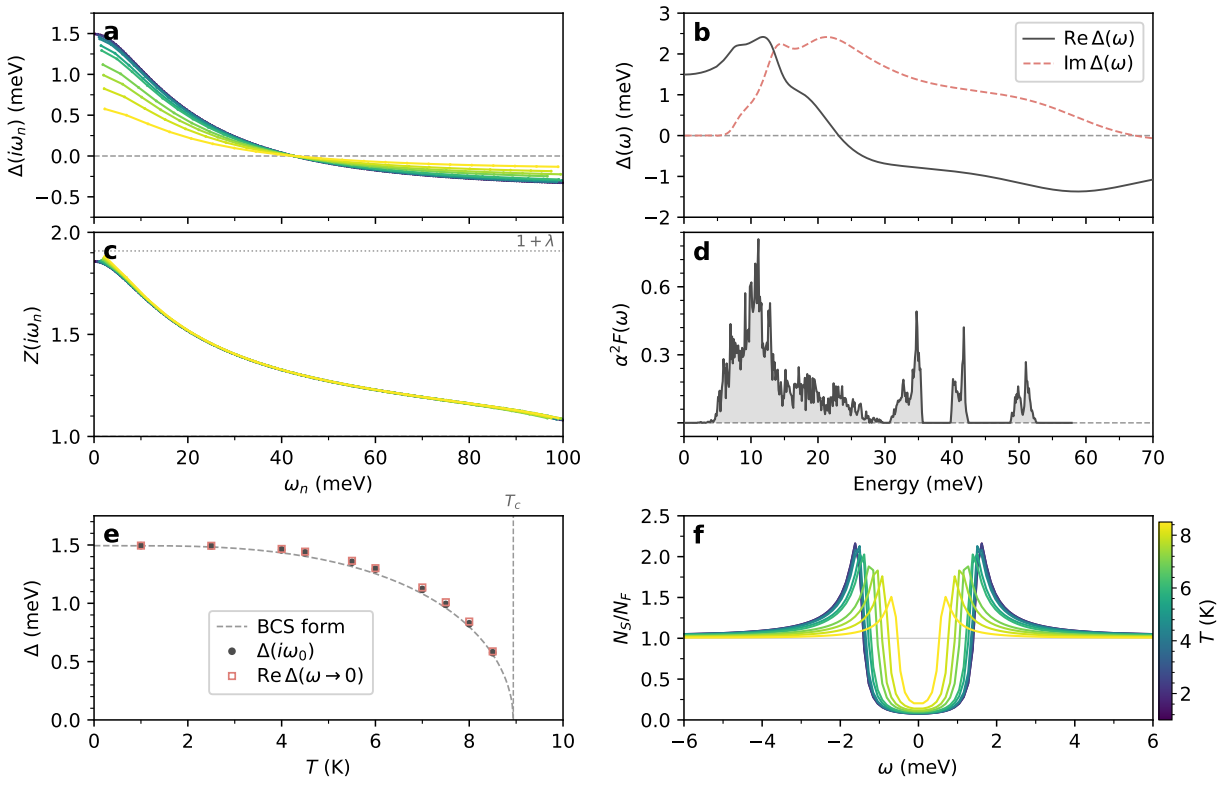


Figure S2.19: Isotropic Eliashberg calculations for undoped $LaRu_3Si_2$ in SG 66 ($Cccm$), using the spectral function in **d**, $\mu^* = 0.1$, and a Matsubara cutoff $\omega_c = 100\,\text{meV}$. **a,c** Gap function $\Delta(i\omega_n)$ and mass-renormalization function $Z(i\omega_n)$, respectively, at the fermionic Matsubara frequencies $\omega_n = (2n+1)\pi k_B T$. The dotted line in **c** marks $1+\lambda = 1.909$. **b** Real and imaginary parts of $\Delta(\omega)$ at 1 K, obtained by Padé continuation of the Matsubara-axis solution. **d** Input Eliashberg function $\alpha^2F(\omega)$, calculated as a Brillouin-zone average on a uniform $12 \times 12 \times 8$ **q** mesh with 0.05 meV Gaussian broadening. **e** Temperature dependence of $\Delta(i\omega_0)$ (filled circles) and $\text{Re}\,\Delta(\omega \to 0)$ (open squares), obtained from the Matsubara-axis solutions and their Padé continuations, respectively. The dashed line shows the BCS-like interpolation $\Delta(T) = \Delta_0 \tanh[1.74\sqrt{T_c/T - 1}]$, with $\Delta_0 = 1.494\,\text{meV}$ and $T_c = 8.94\,\text{K}$ taken from the Eliashberg calculations rather than fitted to the temperature dependence. **f** Normalized quasiparticle DOS $N_S(\omega)/N_F$, evaluated from Eq. (S2.37) with $\delta = 0.116\,\text{meV}$. The shared colour bar indicates the ten temperatures used in **a**, **c**, and **f**.

per unit cell induces ferromagnetism. This observation aligns with prior studies suggesting that a half-filled FB is prone to magnetization and polarization, as well as with the magnetic instabilities observed in FeGe and other kagome materials featuring partially filled FBs at the Fermi level (E_F) [68–70] However, at doping levels below one hole per unit cell, although some phonon modes soften, no imaginary modes appear, and the system remains paramagnetic. This suggests that $LaRu_3Si_2$ retains its structural and magnetic stability under light hole doping.

The doping effects on SC in the SG 66 phase of $LaRu_3Si_2$ are presented in Table S2.5, where the filling level is varied by introducing the background charge. As shown in Fig. S2.20**a**, which depicts the band dispersion and DOS at different filling levels (for simplicity, only the dispersion along the high-symmetry $H - L$ line is shown), changes in the background charge effectively result in a rigid shift of the total band structure and DOS. Specifically, doping one electron or hole shifts E_F by roughly $+0.12\,\text{eV}$ or $-0.12\,\text{eV}$, respectively. The full doping curve across an extended range is calculated using the rigid band approximation, as shown in Fig. S2.20**c**. Here, the shift in the chemical potential μ is mapped onto the hole doping level by integrating the DOS rather than by a constant rate, which places one hole per unit cell at 83 meV, two at 145 meV and four at 266 meV. Note that under the rigid band approximation, where both electronic and phononic bands are fixed, the λ and T_c calculated here are likely to be underestimated, This underestimation arises because, as shown in Fig. S2.20**b**, the phononic bands tend to soften with increasing levels of hole doping, which would, in reality, enhance λ and, consequently, T_c.

A maximal Allen-Dynes $T_c = 16.9\,\text{K}$ is observed at 120 meV below the E_F, and the isotropic Eliashberg solution of the same coupling puts its own maximum at 20.4 K at 150 meV. This filling is close to the peak of DOS given by the quasi-FB below the E_F (Fig. S2.10**l**). Note that such a large hole doping brings the system to the edge of the ferromagnetic phase in DFT, as shown in Fig. S2.20**c**: the Allen-Dynes maximum falls at 1.6 holes per unit cell and the ferromagnetic solution becomes the ground state at two. In Fig. S2.21, we show the $\lambda_{\mathbf{q},\nu}$ along high-symmetry lines and the element- and local-axis-resolved $\lambda(\omega)$ for different dopings. We observe that the λ increases when the Fermi level is shifted closer to the peak in DOS, while it decreases when shifted further from the peak, consistent with the experiment observation [65–67]. The phonon orbital contributions remain almost the same. Note that while the DOS $D(E_F)$ appears in the denominator of Eq. (S2.8), the integration of two delta functions results in an expression proportional to $D(E_F)^2$, so that $\lambda_{\mathbf{q},\nu}$ remains proportional to $D(E_F)$, as shown in Eq. (S2.9).

Figs. S2.22 to S2.25 show the species- and local-axis-resolved $\alpha^2F(\omega)$ and $\lambda(\omega)$ at the six fillings, using the projection defined in Section S2.5.2. The species-resolved contributions retain the same hierarchy: Ru accounts for 63-66% of the total λ, La for 22-26%, and Si for 9-15%.

Hole doping toward the quasi-flat band nevertheless increases the in-plane anisotropy of the Ru contribution. Between zero doping and $E_F - \mu = +0.15\,\text{eV}$, $\lambda_{\text{Ru},x}$ increases from 0.315 to 0.733, while λ_{Ru} increases from 0.580 to 1.161. The local x (B_{3u}) channel therefore grows from 54% to 63% of the Ru contribution, and $\lambda_{\text{Ru},x}/\lambda_{\text{Ru},y}$ increases from 3.2 to 4.6. By comparison, the in-plane ratios remain within 0.93-1.10 for La and 0.68-0.77 for Si across the sampled fillings.

The mode-count sum rule in Eq. (S2.21) provides a reference for comparing channels with different numbers of displacement degrees of freedom: $(N_s/3N_{\text{at}})\lambda$ for species s and axis c. For Ru, $N_s = 6$ and $N_{\text{at}} = 12$, giving a reference of $\lambda/6$ for each local axis. The Ru local-x contribution is approximately 2.08 times this reference at zero doping and 1.94-2.49 times it across the sampled fillings. This normalization quantifies the projected EPC weight per displacement degree of freedom; it does not separate phonon-frequency effects from directional matrix elements.

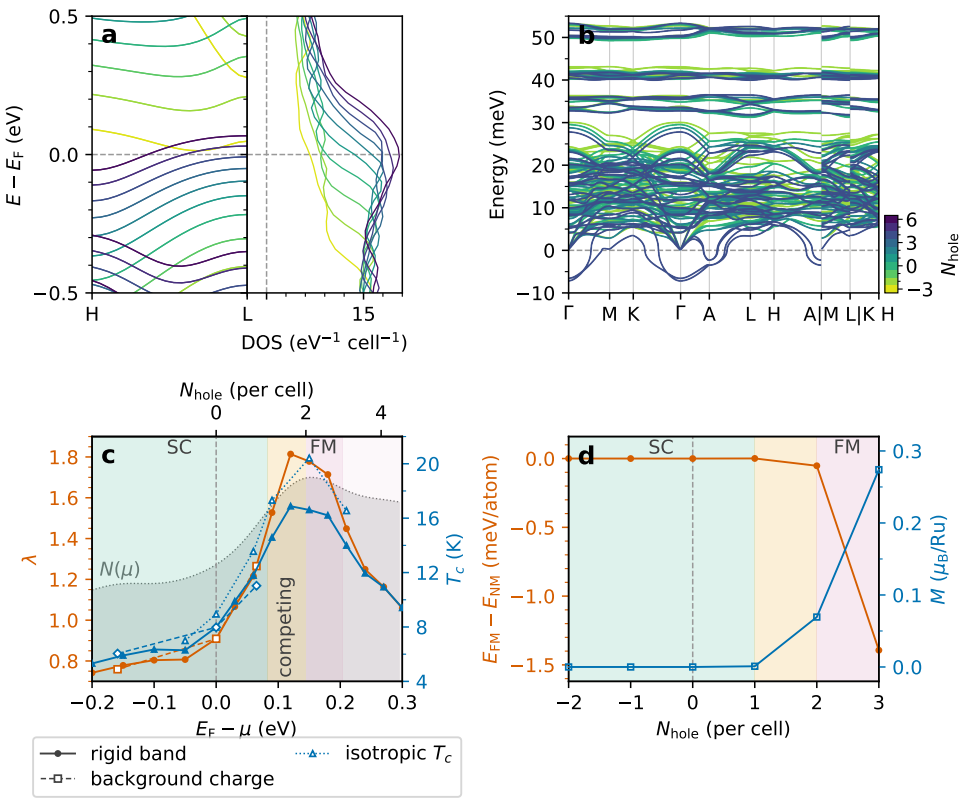


Figure S2.20: Doping effects in the $1 \times 1 \times 2$ SG 66 ($Cccm$) phase of $LaRu_3Si_2$. **a** Band structures along H–L (left) and total DOS (right) for ten background-charge fillings, $N_{\text{hole}} = -3$ to $+6$ per cell, with energies referenced to the corresponding E_F. The bands and DOS evolve approximately rigidly, with an E_F shift of 117 meV per hole near the undoped filling, compared with 83 meV for the first hole estimated from the integrated rigid-band DOS in **c**. **b** Phonon dispersions at $N_{\text{hole}} = -2$, 0, 2, and 4. Hole doping progressively softens the low-energy modes, leading to dynamical instability beyond approximately two holes per cell. **c** EPC strength λ (left axis) and T_c (right axis) versus the rigid-band shift $E_F - \mu$, together with the DOS $N(\mu)$. Filled markers denote 15 converged EPW calculations on $12 \times 12 \times 8$ **q** and $24 \times 24 \times 16$ **k** meshes, with Allen-Dynes T_c estimates at $\mu^* = 0.10$, as used in main-text Fig. 3**d**. Open triangles show isotropic Migdal-Eliashberg T_c values at six shifts, exceeding the Allen-Dynes estimates by 11-23% and peaking at 20.4 K, where the latter gives 16.6 K. Open squares and diamonds show three self-consistent background-charge calculations from Table S2.5; the fourth, in the ferromagnetic region, is omitted. **d** Energy difference between the ferromagnetic (FM) and nonmagnetic (NM) solutions, $E_{\text{FM}} - E_{\text{NM}}$ (left axis) and mean Ru magnetic moment (right axis) at six fillings. The Ru moments are sphere-projected and averaged over the six kagome Ru sites. The moment vanishes through one hole per cell and reaches 0.069 and 0.274 μ_B per Ru at two and three holes per cell, respectively. At three holes per cell, the ferromagnetic solution lies 1.39 meV per atom below the nonmagnetic solution. The corresponding moments averaged over all 12 atoms at two and three holes per cell are 0.031 and 0.131 μ_B per atom, respectively. Panels **a,b** share a colour scale for N_{hole}, which also labels the horizontal axis in **d**. The upper doping axis in **c** is obtained from the integrated rigid-band DOS, which also maps the phase boundaries from **d** onto the shaded regions.

Table S2.5: Superconducting properties of doped $LaRu_3Si_2$ in the $1 \times 1 \times 2$ SG 66 ($Cccm$) phase. Doping is introduced using a compensating background charge, with the structure relaxed and phonons recalculated at each filling. T_c is estimated using the Allen-Dynes formula [Eq. (S2.32)] with $\mu^* = 0.10$, and $\omega_{\log}$ is the logarithmic average phonon frequency. The nonmagnetic result at $N_{\text{hole}} = 2$ is omitted from Fig. S2.20**c** because the ferromagnetic state is energetically favoured [Fig. S2.20**d**]. All four calculations use commensurate $12 \times 12 \times 8$ **q** and $24 \times 24 \times 16$ **k** meshes. The undoped entry is the SG 66 result listed in Table S2.4.

$N_e - N_e^{\text{undoped}}$	E_F/eV	$D(E_F)$/states spin^{-1} eV^{-1} unit cell^{-1}	λ	$\omega_{\log}$/K	T_c/K
+1	16.3501	1.991	0.7594	143.47	6.05
0	16.1912	2.206	0.9089	133.81	7.97
−1	16.1262	2.398	1.2650	115.79	11.03
−2	16.0228	3.278	2.6015	82.95	13.92

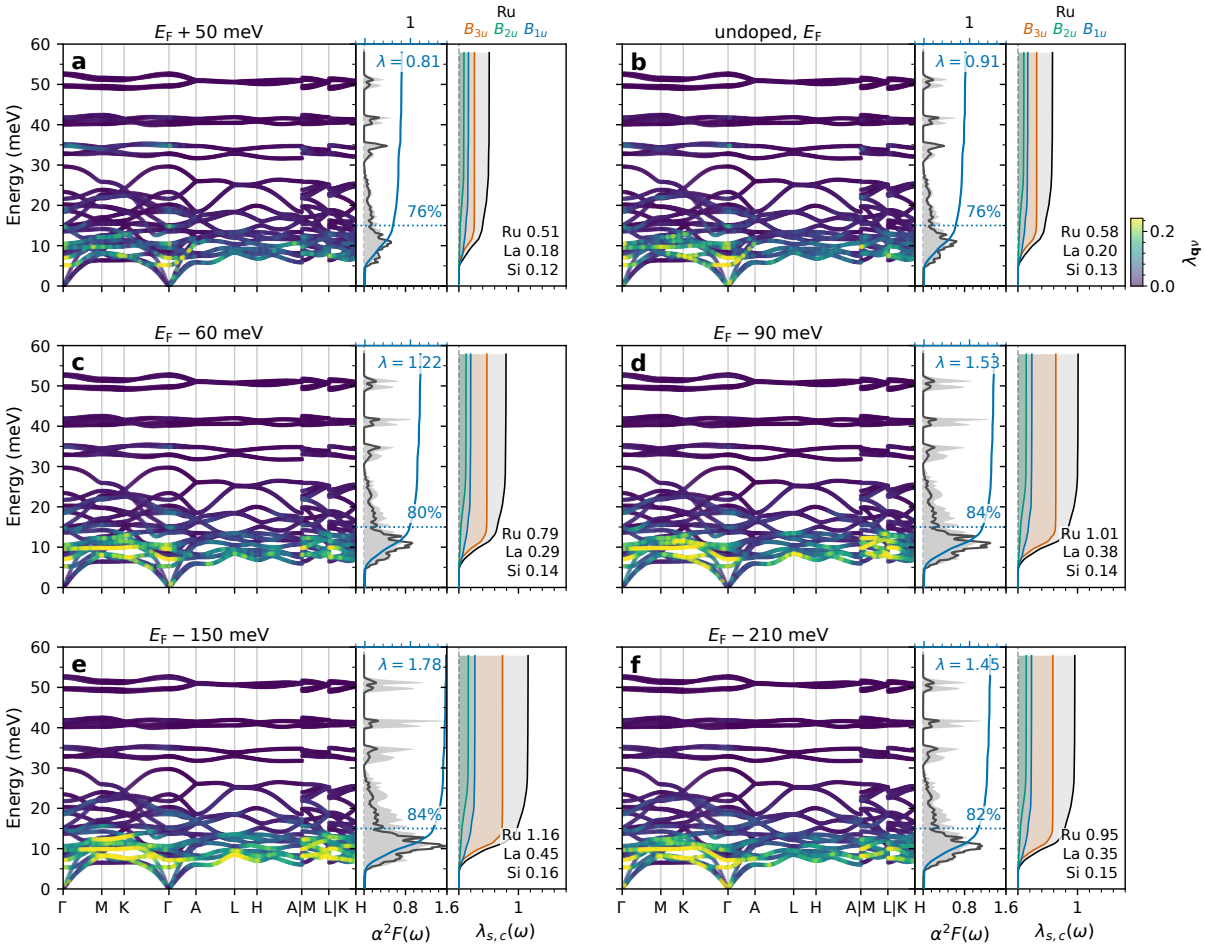


Figure S2.21: Mode- and local-axis-resolved EPC of $LaRu_3Si_2$ in SG 66 ($Cccm$) under rigid-band doping. **a**–**f** correspond to $E_F - \mu = -0.05$, 0, +0.06, +0.09, +0.15, and +0.21 eV, respectively, where E_F is the undoped Fermi level (Fig. S2.20**c**). Each group contains three subpanels sharing a phonon-energy axis. Left: phonon dispersion along high-symmetry lines, coloured by the mode-resolved EPC $\lambda_{\mathbf{q},\nu}$. Middle: $\alpha^2F(\omega)$ (dark line), phonon DOS (grey fill, rescaled to the peak of α^2F), and cumulative $\lambda(\omega)$ (blue). Right: cumulative Ru contribution $\lambda_{\mathrm{Ru}}(\omega)$ (black) and its local-axis projections $\lambda_{\mathrm{Ru},c}(\omega)$ (coloured fills), using the kagome local frame of Fig. S2.3 and the weights defined in Eq. (S2.19). The total and species-resolved EPC values and the fraction of λ below 15 meV (dotted lines) are indicated. All six groups share common scales for the mode-resolved EPC colour map, α^2F, and cumulative λ. The colour scale is capped at the 99th percentile of $\lambda_{\mathbf{q},\nu}$ across all six fillings. The spectral functions and cumulative couplings are Brillouin-zone averages on a uniform $12 \times 12 \times 8$ $\mathbf{q}$ mesh, rather than sums along the plotted path. The α^2F and phonon DOS curves are displayed with 0.2 meV Gaussian broadening.

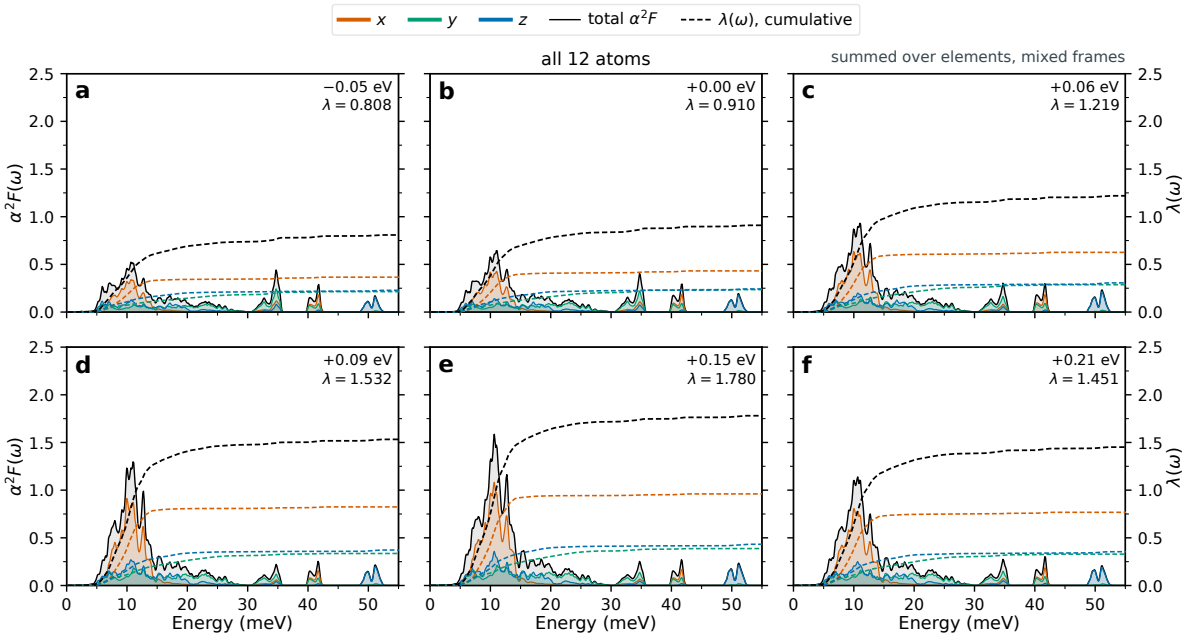


Figure S2.22: Local-axis decomposition of the Eliashberg function and cumulative EPC of $LaRu_3Si_2$ in SG 66 ($Cccm$) under rigid-band doping. **a**–**f** correspond to $E_F - \mu = -0.05$, 0, +0.06, +0.09, +0.15, and +0.21 eV, respectively (Fig. S2.20**c**). Filled curves show the projected $\alpha^2F_c(\omega)$ (left axis), and dashed curves show the corresponding cumulative $\lambda_c(\omega)$ (right axis), for $c = x, y, z$. The black curve shows the total $\alpha^2F(\omega)$ from `EPW`; the total λ is indicated in each panel. The projections follow Section S2.5.2 and are summed over all twelve atoms. Ru uses the kagome local frame of Fig. S2.3, whereas La and Si use the global Cartesian axes. The spectra are displayed with 0.20 meV Gaussian broadening; the integrated EPC values are evaluated directly from mode sums without this spectral broadening. Species-resolved projections are shown in Figs. S2.23 to S2.25. Vertical scales differ across these four figures.

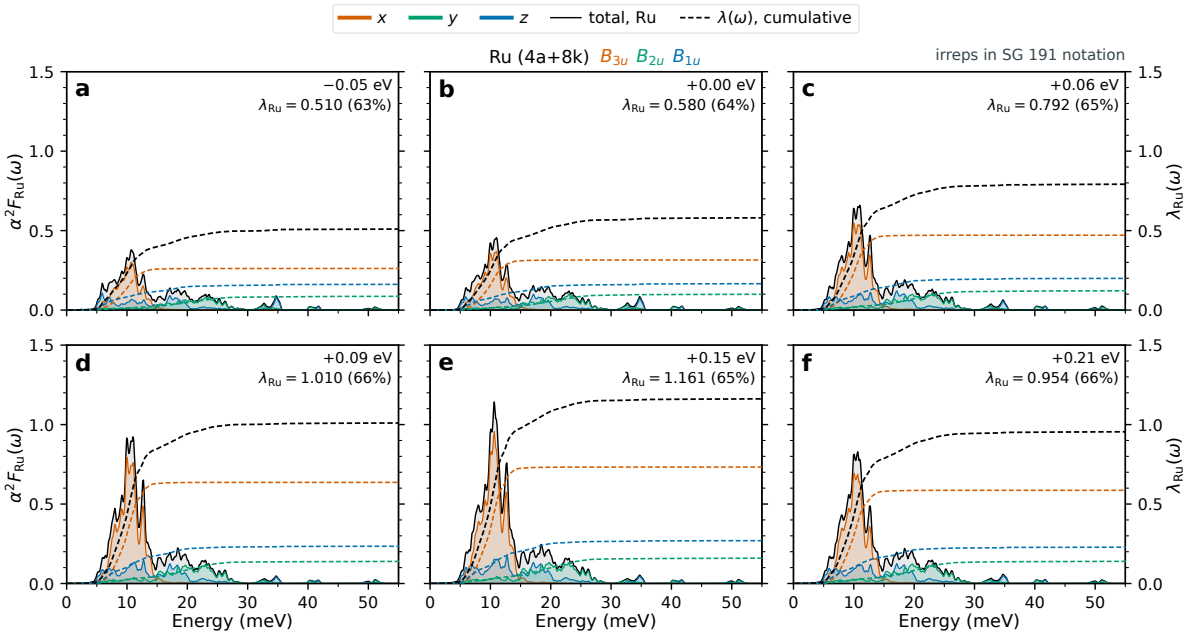


Figure S2.23: Ru local-axis decomposition of $\alpha^2F(\omega)$ in SG 66 $LaRu_3Si_2$ across the rigid-band doping sweep. **a**–**f** show $\alpha^2F_{\mathrm{Ru}}(\omega)$ (filled, left axis) and $\lambda_{\mathrm{Ru}}(\omega)$ (dashed, right axis) at $E_F - \mu = -0.05,\ 0,\ +0.06\,\mathrm{eV},\ +0.09\,\mathrm{eV},\ +0.15\,\mathrm{eV}$, and $+0.21\,\mathrm{eV}$. Black curves denote the total Ru contribution; coloured curves denote the projections onto the Ru kagome local axes of Fig. S2.3 (x toward the hexagon centre, y toward the triangle centre, and $z \parallel c$). Each panel lists λ_{Ru} and the Ru fraction of the total λ. Projection definitions are given in Section S2.5.2; spectra use 0.20 meV Gaussian broadening.

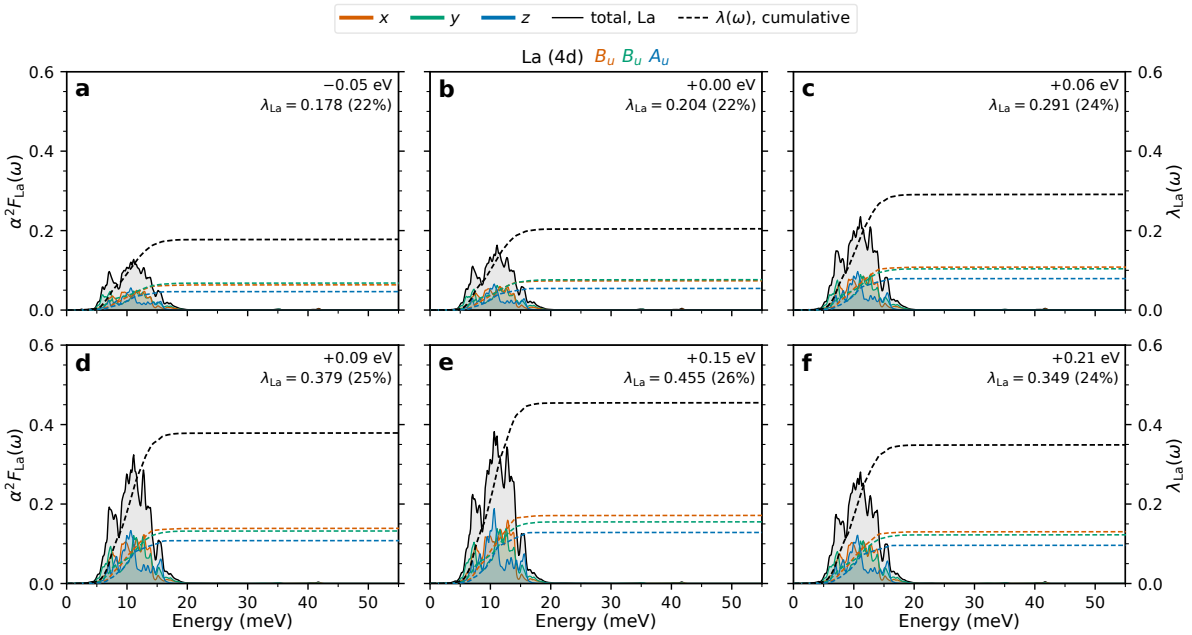


Figure S2.24: Same as Fig. S2.23, but for the La contribution projected onto the global Cartesian axes. Across the doping sweep, La contributes 22-26% of the total λ, second only to Ru. The in-plane contributions are similar, with $0.93 \leq \lambda_{\mathrm{La},x}/\lambda_{\mathrm{La},y} \leq 1.10$. Note the different vertical scale.

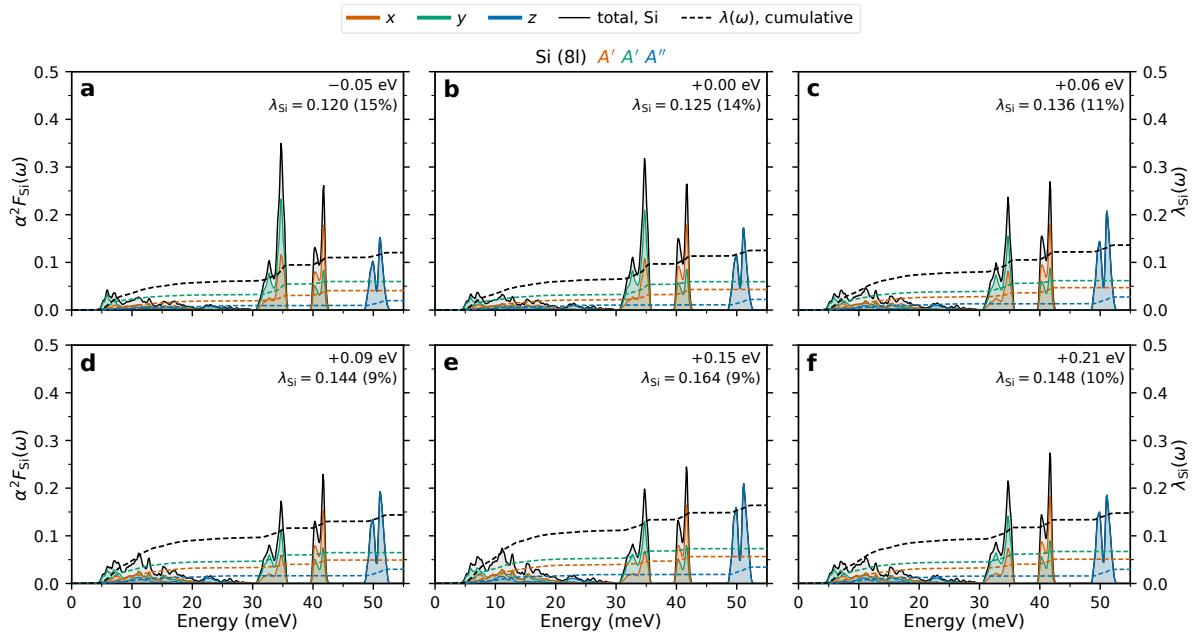


Figure S2.25: Same as Fig. S2.23, but for the Si contribution projected onto the global Cartesian axes. Across the doping sweep, $0.68 \leq \lambda_{\mathrm{Si},x}/\lambda_{\mathrm{Si},y} \leq 0.77$. Between $E_F - \mu = -0.05\,\mathrm{eV}$ and $+0.15\,\mathrm{eV}$, λ_{Si} increases from 0.121 to 0.164, whereas its share of the total λ decreases from 15% to 9%. The Si contribution to $\alpha^2F(\omega)$ is concentrated near 34, 41 and 50 meV. Note the different vertical scale.

Doping dependence of mode selectivity. We group phonon modes by their Ru local-axis weights $W_{\mathrm{Ru},c}(\mathbf{q},\nu)$ (Table S2.6). In the undoped state, modes with $W_{\mathrm{Ru},x} > 0.5$ account for 12.5% of the sampled $(\mathbf{q},\nu)$ pairs but contribute 30.5% of the total λ; for $W_{\mathrm{Ru},x} > 0.7$, the corresponding fractions are 4.6% and 13.4%.

To remove the explicit ω^{-2} factor in Eq. (S2.8), we compare $\lambda_{\mathbf{q},\nu}\omega^2_{\mathbf{q},\nu} = \gamma_{\mathbf{q},\nu}/[2\pi D(E_F)]$ for the same selections (Table S2.7). The undoped local-x and local-y selections have comparable mean $\lambda\omega^2$ values, at 0.98 and 1.07 times the all-mode mean, respectively, whereas their mean frequencies are 10.2 and 22.6 meV. This frequency separation is discussed in Section S3.2. At $E_F - \mu = +0.15\,\mathrm{eV}$, the corresponding ratios to the doped all-mode mean are 1.70 and 1.08. The increased relative local-x selectivity therefore persists after removing the explicit inverse-frequency factor. The local-x median of $\lambda\omega^2$ is also higher, at $13.9\,\mathrm{meV}^2$ compared with $8.1\,\mathrm{meV}^2$ for all modes, showing that the difference is not confined to the high-value tail.

Table S2.6: EPC of phonon subsets selected by their Ru local-x weight $W_{\mathrm{Ru},x}$ (Eq. (S2.19)) on the $12 \times 12 \times 8$ $\mathbf{q}$ mesh with 36 branches. Each subset S contains modes satisfying $W_{\mathrm{Ru},x} > t$, with f_S denoting its fraction of the sampled modes. The subset contribution $\lambda_S = \sum_{\mathbf{q}} w_{\mathbf{q}} \sum_{\nu \in S(\mathbf{q})} \lambda_{\mathbf{q},\nu}$ includes the full EPC of each selected mode, without multiplication by $W_{\mathrm{Ru},x}$. The enhancement factor $R_\lambda = (\lambda_S/\lambda)/f_S$ compares the subset-averaged EPC with the all-mode average. The subsets are nested, and their mode fractions are common to both fillings. The total EPC values are $\lambda = 0.910$ and 1.780, respectively.

		$E_F - \mu = 0$			$E_F - \mu = +0.15\,\mathrm{eV}$		
Threshold t	f_S	λ_S	λ_S/λ	R_λ	λ_S	λ_S/λ	R_λ
0.3	25.4%	0.485	53.3%	2.10	1.165	65.5%	2.58
0.4	19.4%	0.386	42.5%	2.19	0.952	53.5%	2.75
0.5	12.5%	0.277	30.5%	2.44	0.679	38.1%	3.05
0.6	7.8%	0.190	20.8%	2.66	0.460	25.8%	3.30
0.7	4.6%	0.121	13.4%	2.89	0.285	16.0%	3.46

Table S2.7: Subset-averaged EPC and frequency-weighted EPC for modes selected by their Ru local-x or local-y weights. Angle brackets denote averages over the modes in each subset. The dimensionless ratios $R_A = \langle A \rangle_S / \langle A \rangle_{\mathrm{all}}$ are evaluated separately at each filling for $A = \lambda_{\mathbf{q},\nu}$ and $\lambda_{\mathbf{q},\nu}\omega^2_{\mathbf{q},\nu}$. By Eq. (S2.8), $R_{\lambda\omega^2} = \langle \gamma \rangle_S / \langle \gamma \rangle_{\mathrm{all}}$, giving the normalized mean phonon linewidth. The all-mode means at the two fillings are $\langle \lambda \rangle_{\mathrm{all}} = 0.0253$ and 0.0494, and $\langle \lambda\omega^2 \rangle_{\mathrm{all}} = 6.55$ and $9.45\,\mathrm{meV}^2$, respectively.

			$E_F - \mu = 0$		$E_F - \mu = +0.15\,\mathrm{eV}$	
Subset S	f_S	$\langle \omega \rangle_S$ /meV	R_λ	$R_{\lambda\omega^2}$	R_λ	$R_{\lambda\omega^2}$
All modes	100%	23.5	1.00	1.00	1.00	1.00
$W_{\mathrm{Ru},x} > 0.5$	12.5%	10.2	2.44	0.98	3.05	1.70
$W_{\mathrm{Ru},y} > 0.5$	14.6%	22.6	0.59	1.07	0.45	1.08
$W_{\mathrm{Ru},x} > 0.7$	4.6%	9.8	2.89	1.10	3.46	1.82
$W_{\mathrm{Ru},y} > 0.7$	10.3%	23.4	0.56	1.11	0.40	1.05

S3 Analytical models

We use analytical models to examine the hopping derivatives and phonon-frequency hierarchy discussed in Section S2.5. Section S3.1 treats the electronic hopping and its displacement dependence, while Section S3.2 describes the kagome lattice dynamics.

S3.1 Electron-phonon coupling of $d_{x^2-y^2}$ orbitals

To understand why the EPC in $LaRu_3Si_2$ is dominated by the B_{3u} (local x) kagome phonon, we parameterise the electron hopping in the two-centre Slater-Koster (SK) formalism [71] and adopt the Gaussian approximation (GA) of Ref. [72]. In the SK formalism a hopping matrix element is a function of the direction cosines of the bond vector $\mathbf{r}$ [Fig. S3.1**b**],

$$l = \frac{r_x}{|\mathbf{r}|}, \quad m = \frac{r_y}{|\mathbf{r}|}, \quad n = \frac{r_z}{|\mathbf{r}|} \tag{S3.1}$$

and of the σ-, π- and δ-bonding integrals, tabulated for d orbitals in Table S3.1. The GA supplies the radial dependence, assuming that every bonding integral decays as a Gaussian in the bond length,

$$V_i(\mathbf{r}) = V_{i,0} \exp\left(-\gamma_i \frac{|\mathbf{r}|^2}{2}\right), \quad i \in \{\sigma, \pi, \delta\}, \tag{S3.2}$$

where $V_{i,0}$ sets the overlap strength and γ_i the decay rate of that bond type. Throughout, $\mathbf{r} = \mathbf{R}_{ij} + \mathbf{u}$ is the instantaneous bond vector, $\mathbf{R}_{ij}$ its equilibrium value and $\mathbf{u}$ the phonon displacement. It is the $\mathbf{u}$ dependence of Eq. (S3.2) that generates the EPC in Section S3.1.2.

Table S3.1: Hopping elements in terms of SK parameters [71]. (l, m, n) are the direction cosines defined as $l = r_x/|\mathbf{r}|, m = r_y/|\mathbf{r}|, n = r_z/|\mathbf{r}|$ (Eq. (S3.1)), where $\mathbf{r} = \mathbf{R} + \mathbf{t}_\beta - \mathbf{t}_\alpha$ is the hopping vector connecting orbital α in the home unit cell to orbital β in unit cell $\mathbf{R}$. $V_{dd\sigma}, V_{dd\pi}, V_{dd\delta}$ are the bonding integrals used to parameterize the hopping, as illustrated in Fig. S3.1**c**–**e**. The d orbitals in this table are defined in the global Cartesian coordinates.

α	β	$t_{\alpha\beta}(\mathbf{R} + \mathbf{t}_\beta - \mathbf{t}_\alpha)$
d_{xy}	d_{xy}	$3l^2m^2V_{dd\sigma} + (l^2 + m^2 - 4l^2m^2)V_{dd\pi} + (n^2 + l^2m^2)V_{dd\delta}$
d_{xy}	d_{yz}	$3lm^2nV_{dd\sigma} + ln(1 - 4m^2)V_{dd\pi} + ln(m^2 - 1)V_{dd\delta}$
d_{xy}	d_{xz}	$3l^2mnV_{dd\sigma} + mn(1 - 4l^2)V_{dd\pi} + mn(l^2 - 1)V_{dd\delta}$
d_{xy}	$d_{x^2-y^2}$	$3/2lm(l^2 - m^2)V_{dd\sigma} + 2lm(m^2 - l^2)V_{dd\pi} + lm(l^2 - m^2)/2V_{dd\delta}$
d_{xy}	d_{z^2}	$\sqrt{3}\{lm[n^2 - (l^2 + m^2)/2]V_{dd\sigma} - 2lmn^2V_{dd\pi} + lm(1 + n^2)/2V_{dd\delta}\}$
d_{yz}	$d_{x^2-y^2}$	$3/2mn(l^2 - m^2)V_{dd\sigma} - mn[1 + 2(l^2 - m^2)]V_{dd\pi} + mn[1 + (l^2 - m^2)/2]V_{dd\delta}$
d_{yz}	d_{z^2}	$\sqrt{3}\{mn[n^2 - (l^2 + m^2)/2]V_{dd\sigma} + mn(l^2 + m^2 - n^2)V_{dd\pi} - mn(l^2 + m^2)/2V_{dd\delta}\}$
d_{xz}	$d_{x^2-y^2}$	$3/2nl(l^2 - m^2)V_{dd\sigma} + nl[1 - 2(l^2 - m^2)]V_{dd\pi} - nl[1 - (l^2 - m^2)/2]V_{dd\delta}$
d_{xz}	d_{z^2}	$\sqrt{3}\{ln[n^2 - (l^2 + m^2)/2]V_{dd\sigma} + ln(l^2 + m^2 - n^2)V_{dd\pi} - ln(l^2 + m^2)/2V_{dd\delta}\}$
$d_{x^2-y^2}$	$d_{x^2-y^2}$	$3/4(l^2 - m^2)^2V_{dd\sigma} + [l^2 + m^2 - (l^2 - m^2)^2]V_{dd\pi} + [n^2 + (l^2 - m^2)^2/4]V_{dd\delta}$
$d_{x^2-y^2}$	d_{z^2}	$\sqrt{3}\{(l^2 - m^2)[n^2 - (l^2 + m^2)/2]/2V_{dd\sigma} + n^2(m^2 - l^2)V_{dd\pi} + (1 + n^2)(l^2 - m^2)/4V_{dd\delta}\}$
d_{z^2}	d_{z^2}	$[n^2 - (l^2 + m^2)/2]^2V_{dd\sigma} + 3n^2(l^2 + m^2)V_{dd\pi} + 3/4(l^2 + m^2)^2V_{dd\delta}$

S3.1.1 Slater-Koster hopping

The electron hopping matrix of d orbitals under the basis chosen as $\{d_{xy}, d_{yz}, d_{xz}, d_{x^2-y^2}, d_{z^2}\}$ in SK parameters with hopping vector $\mathbf{r}$, connecting site i and j, is

$$h_{ij}(\mathbf{r}) = \begin{pmatrix} t_{i1j1}(\mathbf{r}) & \cdots & t_{i1j5}(\mathbf{r}) \\ & \ddots & \vdots \\ * & & t_{i5j5}(\mathbf{r}) \end{pmatrix} \tag{S3.3}$$

where we use $\alpha, \beta \in \{1, \cdots, 5\}$ to denote $\{d_{xy}, \cdots, d_{z^2}\}$ and the explicit formula of each hopping element are listed in Table S3.1. Note that Eq. (S3.3) is written in the basis where the d orbitals are aligned to the Cartesian axes. The direct lattice vectors are defined as

$$(\mathbf{a}, \mathbf{b}, \mathbf{c}) = \begin{pmatrix} a & -\frac{a}{2} & 0 \\ 0 & \frac{\sqrt{3}a}{2} & 0 \\ 0 & 0 & c \end{pmatrix}, \tag{S3.4}$$

and the sublattices are

$$\mathbf{t}_A = (1/2, 1/2, 1/2), \qquad \mathbf{t}_B = (1/2, 0, 1/2), \qquad \mathbf{t}_C = (0, 1/2, 1/2), \tag{S3.5}$$

where the numbers are direct coordinates given under the basis in Eq. (S3.4). In Fig. S2.3**b** and **c**, we show the direct lattice vectors and three kagome sublattices, together with the local coordinates defined on each sublattice.

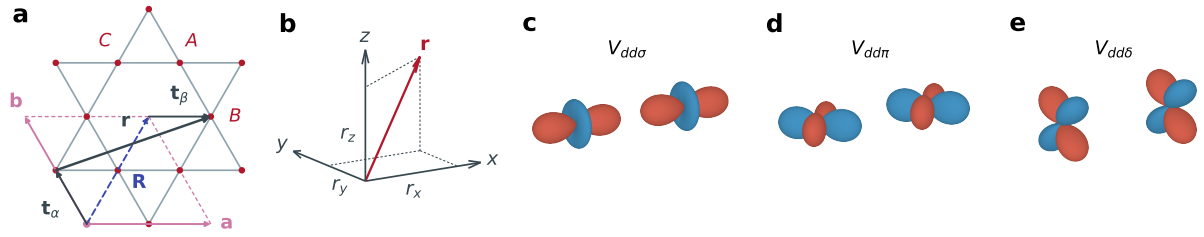


Figure S3.1: **a** Definition of the hopping vector $\mathbf{r} = \mathbf{R} + \mathbf{t}_\beta - \mathbf{t}_\alpha$ in Table S3.1 connecting orbital α to β, where $\mathbf{R}$ is a lattice vector and $\mathbf{t}_{\alpha/\beta}$ are the orbital positions. **b** Illustration of direction cosines in Eq. (S3.1). **c**–**e** Illustration of three types of d orbital hopping integrals in the SK formalism, with **c** being $V_{dd\sigma}$, **d** $V_{dd\pi}$, and **e** $V_{dd\delta}$.

Due to the z-directional mirror ($\mathcal{M}_z$) symmetry of a perfect kagome lattice, the five d orbitals can be divided into two distinct groups: the $\mathcal{M}_z$-even set, which includes the $d_{x^2-y^2}$, d_{xy}, and d_{z^2} orbitals (indexed by 1, 4, and 5), and the $\mathcal{M}_z$-odd set, which consists of the d_{yz} and d_{xz} orbitals (indexed by 2 and 3).

As a result, the full 5×5 hopping matrix $h^f_{ij}(\mathbf{r})$ (explicitly given in Eq. (S3.3)) can be decoupled into two separate blocks corresponding to these $\mathcal{M}_z$-even and -odd orbitals. Furthermore, since our *ab-initio* calculations indicate that the orbitals of interest are primarily the $d_{x^2-y^2}$ orbitals on the kagome lattice, we can further simplify the expression in Eq. (S3.3) to the 3×3 block associated with the $\mathcal{M}_z$ even subset. In this $\mathcal{M}_z$-simplified expression, the full 3×3 hopping matrix $h^{f,\mathcal{M}_z-\text{even}}_{ij}(\mathbf{r})$

between site i and j, ordered by the basis $\{d_{xy}(1), d_{x^2-y^2}(4), d_{z^2}(5)\}$, can be rewritten as:

$$h_{ij}^{f,\mathcal{M}_z-\text{even}}(\mathbf{r}) = \begin{pmatrix} t_{i1j1}^f(\mathbf{r}) & t_{i1j4}^f(\mathbf{r}) & t_{i1j5}^f(\mathbf{r}) \\ & t_{i4j4}^f(\mathbf{r}) & t_{i4j5}^f(\mathbf{r}) \\ * & & t_{i5j5}^f(\mathbf{r}) \end{pmatrix}, \tag{S3.6}$$

where $t_{i\alpha j\beta}^f(\mathbf{r}), \alpha, \beta \in \{1, 4, 5\}$ represents the hopping amplitude between orbital α on site $\mathbf{t}_i$ and orbital β on site $\mathbf{t}_j$ and the indices 1, 4, and 5 correspond to the d_{xy}, $d_{x^2-y^2}$, and d_{z^2} orbitals defined in global Cartesian coordinate, respectively. Specifically, the hopping matrix elements for the $\mathcal{M}_z$-simplified 3×3 hopping matrix can be expressed by taking $n = r_z/|\mathbf{r}| = 0$ in the expressions from Table S3.1 as:

$$\begin{aligned}
t_{i1j1}^f(\mathbf{r}) &= 3l^2m^2V_\sigma(\mathbf{r}) + (l^2 + m^2 - 4l^2m^2)V_\pi(\mathbf{r}) + l^2m^2V_\delta(\mathbf{r}) \\
t_{i1j4}^f(\mathbf{r}) &= \frac{3}{2}lm(l^2 - m^2)V_\sigma(\mathbf{r}) + 2lm(m^2 - l^2)V_\pi + \frac{lm(l^2 - m^2)}{2}V_\delta(\mathbf{r}) \\
t_{i1j5}^f(\mathbf{r}) &= \sqrt{3}\left\{-\frac{lm(l^2 + m^2)}{2}V_\sigma(\mathbf{r}) + \frac{lm}{2}V_\delta(\mathbf{r})\right\} \\
t_{i4j4}^f(\mathbf{r}) &= \frac{3}{4}(l^2 - m^2)^2V_\sigma(\mathbf{r}) + \left[l^2 + m^2 - (l^2 - m^2)^2\right]V_\pi(\mathbf{r}) + \frac{(l^2 - m^2)^2}{4}V_\delta \\
t_{i4j5}^f(\mathbf{r}) &= \sqrt{3}\left\{-\frac{(l^2 - m^2)(l^2 + m^2)}{4}V_\sigma(\mathbf{r}) + \frac{l^2 - m^2}{4}V_\delta(\mathbf{r})\right\} \\
t_{i5j5}^f(\mathbf{r}) &= \frac{1}{4}(l^2 + m^2)^2V_\sigma(\mathbf{r}) + \frac{3}{4}(l^2 + m^2)^2V_\delta(\mathbf{r})
\end{aligned} \tag{S3.7}$$

Then we derive the rotation matrix that transforms the global Cartesian coordinate system into the local coordinate system. For orbitals situated at an arbitrary site $\mathbf{t}_i$ and aligned with the global Cartesian coordinate system (denoted by (x, y, z), referred to as global orbitals), we label them as α. In this context, we ignore the sublattice indices and use the subscript α solely to distinguish different global orbitals. The creation operator $f_{i,\alpha}^\dagger$ is defined as creating a global orbital α at site $\mathbf{t}_i$. On the other hand, the creation operators for local orbitals are denoted as $c_{i,\alpha'}^\dagger$, where α' represents the local orbitals defined with respect to the local axes (denoted as (x_i, y_i, z_i)) specified by the site symmetry group at site $\mathbf{t}_i$. The rotation matrix on site $\mathbf{t}_i$ that transforms the global orbitals α to the local orbitals α' is denoted as $\mathcal{R}_l^{el}$, where the superscript el indicates the electronic system. This matrix defines the relationship between the global and local coordinate systems. Consequently, the local orbitals $c_{i,\alpha'}^\dagger$ can be expressed in terms of the global orbitals as:

$$c_{i,\alpha'}^\dagger = \sum_\alpha f_{i,\alpha}^\dagger \left[\mathcal{R}_i^{el}\right]_{\alpha\alpha'}, \tag{S3.8}$$

where $\left[\mathcal{R}_i^{el}\right]_{\alpha\alpha'}$ represents the elements of the rotation matrix $\mathcal{R}_i^{el}$. Specifically, if we consider an anticlockwise rotation around the z-axis by an angle θ (as illustrated in Fig. S2.3**a**), the rotation matrices for different types of orbitals are given as follows:

- For p orbitals (ordered as $\{p_x, p_y, p_z\}$): The rotation matrix is given by:

$$\mathcal{R}^p(\theta) = \begin{pmatrix} \cos\theta & -\sin\theta & 0 \\ \sin\theta & \cos\theta & 0 \\ 0 & 0 & 1 \end{pmatrix}. \tag{S3.9}$$

- For d orbitals (ordered as $\{d_{xy}, d_{yz}, d_{xz}, d_{x^2-y^2}, d_{z^2}\}$): The rotation matrix takes a more complex form due to the different symmetries of d orbitals. It is given by:

$$\mathcal{R}^d(\theta) = \begin{pmatrix} \cos 2\theta & 0 & 0 & \sin 2\theta & 0 \\ 0 & \cos\theta & \sin\theta & 0 & 0 \\ 0 & -\sin\theta & \cos\theta & 0 & 0 \\ -\sin 2\theta & 0 & 0 & \cos 2\theta & 0 \\ 0 & 0 & 0 & 0 & 1 \end{pmatrix}. \tag{S3.10}$$

This local coordinate system is defined based on the site symmetry group of the kagome lattice. Specifically, at WKP $3g$, the symmetry group is $mmm(D_{2h})$. Define the transformation matrix from the global to local coordinates on three kagome sublattices:

$$\mathcal{R}^{el}_A = \mathcal{R}^d(-\frac{2\pi}{3}) = \begin{pmatrix} -\frac{1}{2} & 0 & 0 & \frac{\sqrt{3}}{2} & 0 \\ 0 & -\frac{1}{2} & -\frac{\sqrt{3}}{2} & 0 & 0 \\ 0 & \frac{\sqrt{3}}{2} & -\frac{1}{2} & 0 & 0 \\ -\frac{\sqrt{3}}{2} & 0 & 0 & -\frac{1}{2} & 0 \\ 0 & 0 & 0 & 0 & 1 \end{pmatrix}, \quad \mathcal{R}^{el}_B = \mathcal{R}^d(0) = \mathbb{1}_{5\times 5}, \quad \mathcal{R}^{el}_C = \mathcal{R}^d(\frac{2\pi}{3}) = \left[\mathcal{R}^{el}_A\right]^{-1}. \tag{S3.11}$$

Similarly, the rotation matrices $\mathcal{R}^{ph}_i$ with $i \in \{A, B, C\}$ for the phonon atom movement $\mathbf{u} \equiv (u_{i,x}, u_{i,y}, u_{i,z})$ (which are equivalent to the rotation matrices for p orbitals $\mathcal{R}^p$) are

$$\mathcal{R}^{ph}_A = \mathcal{R}^p(-\frac{2\pi}{3}) = \begin{pmatrix} -\frac{1}{2} & \frac{\sqrt{3}}{2} & 0 \\ -\frac{\sqrt{3}}{2} & -\frac{1}{2} & 0 \\ 0 & 0 & 1 \end{pmatrix}, \quad \mathcal{R}^{ph}_B = \mathcal{R}^p(0) = \mathbb{1}_{3\times 3}, \quad \mathcal{R}^{ph}_C = \mathcal{R}^p(\frac{2\pi}{3}) = \left[\mathcal{R}^{ph}_A\right]^{-1}. \tag{S3.12}$$

Accordingly, the hopping matrices transform as

$$h^c_{ij}(\mathbf{r}) = \mathcal{R}^{el,\dagger}_i h^f_{ij}(\mathbf{r}) \mathcal{R}^{el}_j. \tag{S3.13}$$

where the superscript f/c denotes the hopping matrix between global/local orbitals.

In systems such as $LaRu_3Si_2$, where the quasi-FB near E_F is primarily given by Ru A_g (local $d_{x^2-y^2}$) orbitals, it is the 44 element of h^c_{ij} that matters. Writing $\mathcal{R}_{i,+}$ for the $\mathcal{M}_z$-even block of $\mathcal{R}^{el}_i$ in Eq. (S3.11), reordered to the basis $\{d_{xy}(1), d_{x^2-y^2}(4), d_{z^2}(5)\}$ of Eq. (S3.6), Eq. (S3.13) reads $h^c_{ij} = \mathcal{R}^\dagger_{i,+} h^f_{ij} \mathcal{R}_{j,+}$ and gives

$$\begin{aligned} t^c_{A4,B4}(\mathbf{r}) &= [h^c_{AB}(\mathbf{r})]_{44} = \frac{1}{2}\Big(\sqrt{3} t^f_{A1B4}(\mathbf{r}) - t^f_{A4A4}(\mathbf{r})\Big) \\ t^c_{A4,C4}(\mathbf{r}) &= [h^c_{AC}(\mathbf{r})]_{44} = \frac{1}{4}\Big(-3 t^f_{A1C1}(\mathbf{r}) + t^f_{A4C4}(\mathbf{r})\Big) \\ t^c_{B4,C4}(\mathbf{r}) &= [h^c_{BC}(\mathbf{r})]_{44} = \frac{1}{2}\Big(-\sqrt{3} t^f_{A1B4}(\mathbf{r}) - t^f_{A4A4}(\mathbf{r})\Big). \end{aligned} \tag{S3.14}$$

Note that $t^f_{i\alpha j\beta}(\mathbf{r})$ is identical for any pair of sites i and j, as the orbitals are defined in the global Cartesian coordinate system. Therefore, by substituting Eq. (S3.7) into Eq. (S3.14), we obtain the explicit forms of the NN hopping terms between $d_{x^2-y^2}$ orbitals defined in the local coordinate system on a kagome lattice within the SK formalism: For intra-layer NN bonds $n = 0$

and $l^2+m^2=1$, so that $l=\cos\theta$ and $m=\sin\theta$. The NN hopping between A_g orbitals then takes the compact form $t_{mn}(\mathbf{r})=f_{mn}(\mathbf{r})V^d(\mathbf{r})-V_\pi(\mathbf{r})/2$, with a purely geometric factor f_{mn}:

$$\begin{aligned}
t^c_{A4,B4}(\mathbf{r}) &= f_{A4,B4}(\mathbf{r})V^d(\mathbf{r})-\frac{1}{2}V_\pi(\mathbf{r}), \qquad f_{A4,B4}(\mathbf{r}) = -(l-m)(l+m)(l^2-2\sqrt{3}lm-m^2),\\
t^c_{A4,C4}(\mathbf{r}) &= f_{A4,C4}(\mathbf{r})V^d(\mathbf{r})-\frac{1}{2}V_\pi(\mathbf{r}), \qquad f_{A4,C4}(\mathbf{r}) = \frac{1}{2}(l^4-14l^2m^2+m^4),\\
t^c_{B4,C4}(\mathbf{r}) &= f_{B4,C4}(\mathbf{r})V^d(\mathbf{r})-\frac{1}{2}V_\pi(\mathbf{r}), \qquad f_{B4,C4}(\mathbf{r}) = -(l-m)(l+m)(l^2+2\sqrt{3}lm-m^2),
\end{aligned} \tag{S3.15}$$

where $V^d(\mathbf{r})\equiv[V_\delta(\mathbf{r})-4V_\pi(\mathbf{r})+3V_\sigma(\mathbf{r})]/8$, and $\{V_\delta(\mathbf{r}),V_\pi(\mathbf{r}),V_\sigma(\mathbf{r})\}$ are bonding integrals (SK parameters) of d orbitals (i.e., $V_{dd\sigma/\pi/\delta}$ used in Table S3.1), which we assume to be Gaussian (Eq. (S3.2)).

S3.1.2 Displacement derivatives and EPC

To explore the EPC from this SK formalism in GA, it is important to recognize that the EPC strength associated with a given hopping term for a specific electron in relation to a phonon mode can be expressed as [72]:

$$[g(\mathbf{R}_{ij})]_{i\alpha j\beta;\nu} = \partial_{r_\nu} t_{i\alpha j\beta}(\mathbf{r})\Big|_{\mathbf{r}=\mathbf{R}_{ij}}. \tag{S3.16}$$

Here, g_ν represents the EPC constant for the phonon mode ν, and $t(\mathbf{r})$ is the hopping integral that depends on the electron position $\mathbf{r}$, as introduced in Ref. [72]. This derivative indicates how sensitive the hopping parameter is to changes in atomic positions due to phonon displacements, capturing the variation of the electronic hopping strength with respect to the lattice distortion induced by the phonon mode ν. After taking derivatives of Eq. (S3.15), we have the following equation

$$\frac{\partial t_{mn}(\mathbf{r})}{\partial r_\nu} = \frac{\partial f_{mn}(\mathbf{r})}{\partial r_\nu}V^d(\mathbf{r}) + f_{mn}(\mathbf{r})\frac{\partial V^d(\mathbf{r})}{\partial r_\nu} - \frac{1}{2}\frac{\partial V_\pi(\mathbf{r})}{\partial r_\nu} \tag{S3.17}$$

Here, m,n denote the sublattices A,B,C and orbital $d_{x^2-y^2}$. Eq. (S3.17) can be divided into two components: the radial part, which consists of the partial derivatives of the Gaussian decaying bonding integrals $V_i(\mathbf{r})$, and the angular part, which consists of the partial derivatives of the function $f_{mn}(\mathbf{r})$. We start with the radial parts in Eq. (S3.17). For the partial derivatives of SK hopping integrals $V_i(\mathbf{r})$, $i\in\{\sigma,\pi,\delta\}$, individually, we have

$$\frac{\partial V_i(\mathbf{r})}{\partial r_\nu} = \frac{\partial V_{i,0}\exp\left(-\gamma_i\frac{|\mathbf{r}|^2}{2}\right)}{\partial r_\nu} = -r_\nu\gamma_i V_{i,0}\exp\left(-\gamma_i\frac{r^2}{2}\right) \tag{S3.18}$$

which leads to

$$\begin{aligned}
\frac{\partial V^d(\mathbf{r})}{\partial r_\nu} &= \frac{1}{8}\frac{\partial V_\delta(\mathbf{r})-4V_\pi(\mathbf{r})+3V_\sigma(\mathbf{r})}{\partial r_\nu}\\
&= \frac{1}{8}\frac{\partial V_{\delta,0}\exp\left(-\gamma_\delta\frac{|\mathbf{r}|^2}{2}\right)}{\partial r_\nu} - \frac{4}{8}\frac{\partial V_{\pi,0}\exp\left(-\gamma_\pi\frac{|\mathbf{r}|^2}{2}\right)}{\partial r_\nu} + \frac{3}{8}\frac{\partial V_{\sigma,0}\exp\left(-\gamma_\sigma\frac{|\mathbf{r}|^2}{2}\right)}{\partial r_\nu}\\
&= -r_\nu[\gamma_\delta V_\delta(\mathbf{r})-4\gamma_\pi V_\pi(\mathbf{r})+3\gamma_\sigma V_\sigma(\mathbf{r})]/8
\end{aligned} \tag{S3.19}$$

From Eqs. (S3.18) and (S3.19), one can determine that the radial component of the EPC for the B_{3u} (local x) and B_{2u} (local y) phonons depends on the projection of the hopping vector $\mathbf{r}$ onto

the corresponding local axes. This dependency leads to the following relation:

$$\frac{\frac{\partial V_i(\mathbf{r})}{\partial x}}{\frac{\partial V_i(\mathbf{r})}{\partial y}} = \frac{x}{y}, \quad i \in \{\sigma, \pi, \delta\} \tag{S3.20}$$

The local x_i axis at every kagome site points at the centre of an adjacent hexagon and therefore makes an angle of 60° with each of the four NN bonds at that site [Fig. S2.3**b** and **c**]. Resolving an NN bond vector on the local axes of either of its end points thus gives $(x, y) = |\mathbf{r}|(\cos 60°, \pm \sin 60°)$, so that $|y/x| = \tan(\pi/3) = \sqrt{3}$ for all three inequivalent NN bonds $\mathbf{r}_{A4,B4} = (a/4, -\sqrt{3}a/4, 0)$, $\mathbf{r}_{B4,C4} = (a/4, \sqrt{3}a/4, 0)$ and $\mathbf{r}_{A4,C4} = (a/2, 0, 0)$, meaning

$$\sqrt{3}\frac{\partial V_i(\mathbf{r})}{\partial x} = \frac{\partial V_i(\mathbf{r})}{\partial y}, \quad i \in \{\sigma, \pi, \delta\} \tag{S3.21}$$

for every Gaussian decaying hopping integral $V_i(\mathbf{r})$, and the same holds for their linear combination in Eq. (S3.19).

Second, for the angular parts in Eq. (S3.17),

$$\begin{aligned}
\frac{\partial f_{A4,B4}(\mathbf{r})}{\partial x} &= -y\frac{2(\sqrt{3}x^4 + 4x^3y - 6\sqrt{3}x^2y^2 - 4xy^3 + \sqrt{3}y^4)}{r^6} \\
\frac{\partial f_{A4,B4}(\mathbf{r})}{\partial y} &= x\frac{2(\sqrt{3}x^4 + 4x^3y - 6\sqrt{3}x^2y^2 - 4xy^3 + \sqrt{3}y^4)}{r^6} \\
\frac{\partial f_{A4,C4}(\mathbf{r})}{\partial x} &= y\frac{16xy(x-y)(x+y)}{r^6} \\
\frac{\partial f_{A4,C4}(\mathbf{r})}{\partial y} &= -x\frac{16xy(x-y)(x+y)}{r^6} \\
\frac{\partial f_{B4,C4}(\mathbf{r})}{\partial x} &= y\frac{2(\sqrt{3}x^4 - 4x^3y - 6\sqrt{3}x^2y^2 + 4xy^3 + \sqrt{3}y^4)}{r^6} \\
\frac{\partial f_{B4,C4}(\mathbf{r})}{\partial y} &= -x\frac{2(\sqrt{3}x^4 - 4x^3y - 6\sqrt{3}x^2y^2 + 4xy^3 + \sqrt{3}y^4)}{r^6}
\end{aligned} \tag{S3.22}$$

From the above equations,

$$\frac{\frac{\partial f_{mn}(\mathbf{r})}{\partial x}}{\frac{\partial f_{mn}(\mathbf{r})}{\partial y}} = -\frac{y}{x} = -\sqrt{3} \tag{S3.23}$$

Thus, we arrive at a relation where the amplitude of the angular component in the partial derivatives of the hopping terms with respect to x is $\sqrt{3}$ times larger than that for y, while the opposite holds for the radial component. To further check the validity of our approximation, the amplitudes of the EPC are calculated numerically.

By fitting DFT data (Fig. S3.2), the corresponding decaying parameters for the SK hopping integrals $V_i(\mathbf{r})$ are $(\gamma_\sigma, V_\sigma) = (0.7143\,\text{Å}^{-2}, -15.2033\,\text{eV})$, $(\gamma_\pi, V_\pi) = (0.4351\,\text{Å}^{-2}, 4.2644\,\text{eV})$ and $(\gamma_\delta, V_\delta) = (0.3096\,\text{Å}^{-2}, -0.8584\,\text{eV})$. The corresponding EPC of $A_g(d_{x^2-y^2})$ orbitals coupling to $B_{3u}(x)$ and $B_{2u}(y)$ atom movements are calculated to be 0.0192 Ry/Bohr and 0.0334 Ry/Bohr, respectively. Both are of the same order as the *ab-initio* values, 0.0201 Ry/Bohr and 0.0204 Ry/Bohr, but the single-orbital model does not reproduce their near-equality, and we return to this in Section S3.1.3.

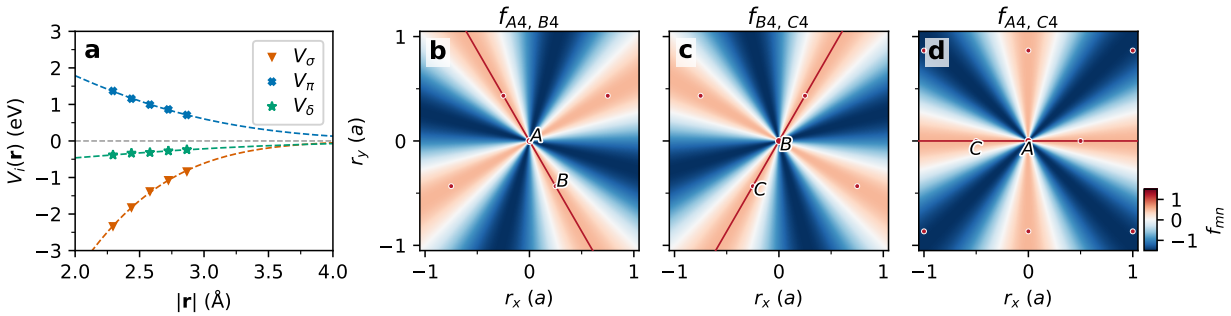


Figure S3.2: The fitted SK parameters. **a** Fitted Gaussian functions for the SK hopping integrals $V_i(\mathbf{r})$ $(i = \sigma, \pi, \delta)$. The parameters, defined in Eq. (S3.2), are $(\gamma_\sigma, V_\sigma) = (0.7143\,\text{Å}^{-2}, -15.2033\,\text{eV})$, $(\gamma_\pi, V_\pi) = (0.4351\,\text{Å}^{-2}, 4.2644\,\text{eV})$ and $(\gamma_\delta, V_\delta) = (0.3096\,\text{Å}^{-2}, -0.8584\,\text{eV})$. **b**–**d** Distribution of $f_{mn}(\mathbf{r})$ with respect to $\mathbf{r} = (r_x, r_y, r_z = 0)$ for $f_{A4,B4}$, $f_{B4,C4}$ and $f_{A4,C4}$. Red circles are the lattice sites and the red line the direction of the corresponding NN hopping vector. In the kagome lattice defined by Eqs. (S3.4) and (S3.5) these are $\mathbf{r}_{A4,B4} = (a/4, -\sqrt{3}a/4, 0)$, $\mathbf{r}_{B4,C4} = (a/4, \sqrt{3}a/4, 0)$ and $\mathbf{r}_{A4,C4} = (a/2, 0, 0)$. **a** is the radial and **b**–**d** the angular part of one formula, and neither half is readable alone.

The angular term does not modify this ratio: $f_{mn}(\mathbf{r})$ is stationary along the NN direction [Fig. S3.2**b**–**d**], so its first derivatives vanish at $\mathbf{r} = \mathbf{R}_{ij}$ and the only contribution left in Eq. (S3.17) is the radial one. Within this single-orbital treatment the EPC of the B_{3u} phonon is therefore smaller than that of the B_{2u} phonon by exactly $\sqrt{3}$. That $\sqrt{3}$ is a property of the A_g-only projection rather than of the kagome lattice, and it bounds the anisotropy instead of predicting it: the *ab-initio* couplings of the two modes are nearly equal. Section S3.1.3 identifies the coupling channel the projection discards.

S3.1.3 Interorbital A_g–B_{1g} hopping

The $\sqrt{3}$ coupling ratio in Section S3.1.2 follows from the A_g–A_g hopping derivative in Eq. (S3.17). Here we examine an interorbital channel omitted by that single-orbital projection.

At the Ru $3g$ site of the parent SG 191 ($P6/mmm$) structure, the local $d_{x^2-y^2}$ and d_{xy} orbitals transform as A_g and B_{1g} of D_{2h}, respectively (Table S2.1). Their distinct site-symmetry labels do not by themselves forbid intersite hopping. The bond-frame $d_{x^2-y^2}$–d_{xy} matrix element vanishes for a bond along x (Eq. (S3.7)), but rotating to the site-local frames mixes these orbitals (Eqs. (S3.11) and (S3.14)). For a representative nearest-neighbor bond, using the orbital convention of Eq. (S3.14), the resulting hopping is

$$t[A_g(i), B_{1g}(j)] = \frac{\sqrt{3}}{4}\left[V_\pi(\mathbf{r}) + \frac{3}{4}V_\sigma(\mathbf{r}) + \frac{1}{4}V_\delta(\mathbf{r})\right], \tag{S3.24}$$

At the parent-phase bond length $|\mathbf{r}| = a/2 = 2.835\,\text{Å}$, the fitted parameters of Fig. S3.2 give $t[A_g(i), B_{1g}(j)] = +0.0148\,\text{eV}$, approximately 2% of the magnitude of the intraorbital hopping in Eq. (S3.15). This small value results from cancellation between $V_\pi = +0.742\,\text{eV}$ and $\frac{3}{4}V_\sigma + \frac{1}{4}V_\delta = -0.708\,\text{eV}$. Because the fitted radial dependences differ (Eq. (S3.2)), this cancellation depends on bond length. The fitted hopping has a zero at

$$|\mathbf{r}|^* = 2.766\,\text{Å}, \tag{S3.25}$$

approximately 0.07 Å below the parent-phase bond length. For comparison, the two Ru–Ru distances in SG 176, 2.75 and 2.93 Å (Fig. S2.2**h**), bracket this zero of the parent-geometry parameterization.

The cancellation of the equilibrium hopping does not require its displacement derivatives, which enter the EPC through Eq. (S3.17), to be small. This interorbital channel can therefore contribute to the EPC of quasi-FB states with mixed A_g and B_{1g} character. Determining whether it explains the nearly equal *ab initio* B_{3u} and B_{2u} couplings requires the multiorbital Bloch eigenvectors and the corresponding displacement-dependent hopping matrix. The present hopping fit does not specify the on-site energies needed to determine these eigenvectors, so it does not quantify the correction to the single-orbital $\sqrt{3}$ result. The hopping cancellation is parameter-specific and should be reassessed when extending the single-orbital description to the candidates of Section S5.

S3.2 Spring-ball model for the kagome lattice

To further investigate the phonon spectrum of the kagome lattice, we employ the spring-ball model. It is set up in the same global Cartesian frame as the electronic model above, with the lattice vectors of Eq. (S3.4) and the three kagome sites, labeled as A, B, and C, on the $3g$ sublattices of Eq. (S3.5), which in Cartesian coordinates are

$$\mathbf{t}_A = (a/4, \sqrt{3}a/4, 0) \qquad \mathbf{t}_B = (a/2, 0, 0) \qquad \mathbf{t}_C = (-a/4, \sqrt{3}a/4, 0). \tag{S3.26}$$

The origin of z is placed in the kagome plane, which is immaterial here because the z motion decouples from the in-plane motion. In this spring-ball model, every two NN kagome sites are connected by a pre-stretched spring (characterized by η) with spring constant κ. The potential energy of the spring connecting neighboring sites i and j is given by the expression

$$E_{ij}(\mathbf{R}_j - \mathbf{R}_i) = \kappa[|\mathbf{t}_j + \mathbf{u}_j - \mathbf{t}_i - \mathbf{u}_i + \mathbf{R}_j - \mathbf{R}_i| - \eta|\mathbf{t}_j - \mathbf{t}_i + \mathbf{R}_j - \mathbf{R}_i|]^2 \tag{S3.27}$$

where $\mathbf{u}_i = (u_{i,x}, u_{i,y}, u_{i,z})$ and $\mathbf{u}_j = (u_{j,x}, u_{j,y}, u_{j,z})$ represent the small displacements of the atoms i and j from their equilibrium positions in global Cartesian coordinate. Here, η represents the pre-stretching parameter of the springs, which defines the equilibrium length of the spring as η times the NN hopping vector length, denoted by $|\mathbf{r}|$. In other words, the natural length of each spring in this model is scaled by the factor η relative to the original NN bond length. The prefactor in Eq. (S3.27) is written as κ rather than $\kappa/2$, so that the longitudinal force constant of a single spring is 2κ, which is the convention in which the force-constant matrices below and Fig. S3.3 are expressed.

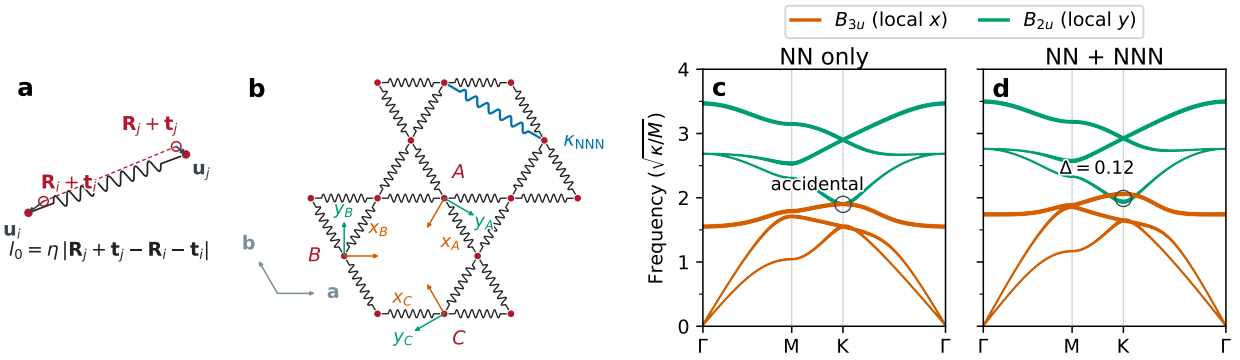


Figure S3.3: The kagome spring-ball model. **a** Illustration of Eq. (S3.27), the interaction between two sites, where $l_0 = \eta|\mathbf{R}_j + \mathbf{t}_j - \mathbf{R}_i - \mathbf{t}_i|$ is the equilibrium length of the spring. **b** The spring-ball model for a 2D kagome system. The local axes at each site are colored as the branches of **c** and **d**, local x in orange and local y in green, and the lattice vectors **a**, **b** are the gray key at the lower left, and κ_{NNN} marks the next-nearest-neighbor (NNN) spring. **c**, **d** The phonon-mode-resolved spectrum of the model without (**c**) and with (**d**) the NNN springs, the two transverse branches labelled by their irrep. The ringed crossing at K in **c** is an accidental degeneracy, not one the little group requires. The NNN springs lift it by $\Delta = 0.12\sqrt{\kappa/M}$ at $\kappa_{\mathrm{NNN}} = 0.05\,\kappa$ and the same η, and leave the other two K degeneracies alone.

In practice, for the NN bonds, we have

$$
\begin{aligned}
E_{AB}[(0,0,0)] &= \kappa\left[\left((u_{B,x}-u_{A,x}+\frac{a}{4})^2+(u_{B,y}-u_{A,y}-\frac{\sqrt{3}a}{4})^2+(u_{B,z}-u_{A,z})^2\right)^{1/2}-\eta\frac{a}{2}\right]^2\\
E_{AC}[(0,0,0)] &= \kappa\left[\left((u_{C,x}-u_{A,x}-\frac{a}{2})^2+(u_{C,y}-u_{A,y})^2+(u_{C,z}-u_{A,z})^2\right)^{1/2}-\eta\frac{a}{2}\right]^2\\
E_{BC}[(1,0,0)] &= \kappa\left[\left((u_{C,x}-u_{B,x}+\frac{a}{4})^2+(u_{C,y}-u_{B,y}+\frac{\sqrt{3}a}{4})^2+(u_{C,z}-u_{B,z})^2\right)^{1/2}-\eta\frac{a}{2}\right]^2.
\end{aligned}
\tag{S3.28}
$$

The force constant matrix $F_{i\mu,j\nu}(\mathbf{R}_j - \mathbf{R}_i)$, which represents the interaction between sites i and j, is calculated as the second derivative of the potential:

$$
F_{i\mu,j\nu}(\mathbf{R}_j - \mathbf{R}_i) = \left.\frac{\partial^2 E_{ij}(\mathbf{R}_j - \mathbf{R}_i)}{\partial \mathbf{u}_{i\mu}\partial \mathbf{u}_{j\nu}}\right|_{\mathbf{u}_{i\mu}=0,\mathbf{u}_{j\nu}=0} \tag{S3.29}
$$

therefore, for the NN bonds,

$$
\begin{aligned}
F_{AB}[(0,0,0)] &= \left.\frac{\partial^2 E_{AB}}{\partial \mathbf{u}_A \partial \mathbf{u}_B}\right|_{\mathbf{u}_A=\mathbf{u}_B=\mathbf{0}} = \begin{pmatrix} -\kappa(2-3\eta/2) & \sqrt{3}\kappa\eta/2 & \\ \sqrt{3}\kappa\eta/2 & -\kappa(2-\eta/2) & \\ & & -2\kappa(1-\eta) \end{pmatrix} \\
F_{AC}[(0,0,0)] &= \left.\frac{\partial^2 E_{AC}}{\partial \mathbf{u}_A \partial \mathbf{u}_C}\right|_{\mathbf{u}_A=\mathbf{u}_C=\mathbf{0}} = \begin{pmatrix} -2\kappa & & \\ & -2\kappa(1-\eta) & \\ & & -2\kappa(1-\eta) \end{pmatrix} \\
F_{BC}[(1,0,0)] &= \left.\frac{\partial^2 E_{BC}}{\partial \mathbf{u}_B \partial \mathbf{u}_C}\right|_{\mathbf{u}_B=\mathbf{u}_C=\mathbf{0}} = \begin{pmatrix} -\kappa(2-3\eta/2) & -\sqrt{3}\kappa\eta/2 & \\ -\sqrt{3}\kappa\eta/2 & -\kappa(2-\eta/2) & \\ & & -2\kappa(1-\eta) \end{pmatrix}.
\end{aligned}
\tag{S3.30}
$$

From this, it is evident that the z-phonon is completely decoupled from the in-plane x- and y-phonons due to the mirror z symmetry $\mathcal{M}_z$. As a result, we will limit our analysis to the system consisting only of the x- and y-phonons. The onsite blocks are second derivatives of the total energy $E = \sum_{\langle ij \rangle} E_{ij}$, equivalently fixed by the acoustic sum rule $F_{ii}(\mathbf{0}) = -\sum_{j\neq i,\mathbf{R}} F_{ij}(\mathbf{R})$. In the global coordinate they read

$$
\begin{aligned}
F_{AA}[(0,0,0)] &= \left.\frac{\partial^2 E}{\partial \mathbf{u}_A^2}\right|_{\mathbf{u}=\mathbf{0}} = \begin{pmatrix} \kappa(8-3\eta) & -\sqrt{3}\kappa\eta \\ -\sqrt{3}\kappa\eta & \kappa(8-5\eta) \end{pmatrix}, \\
F_{BB}[(0,0,0)] &= \left.\frac{\partial^2 E}{\partial \mathbf{u}_B^2}\right|_{\mathbf{u}=\mathbf{0}} = \begin{pmatrix} 2\kappa(4-3\eta) & \\ & 2\kappa(4-\eta) \end{pmatrix}, \\
F_{CC}[(0,0,0)] &= \left.\frac{\partial^2 E}{\partial \mathbf{u}_C^2}\right|_{\mathbf{u}=\mathbf{0}} = \begin{pmatrix} \kappa(8-3\eta) & \sqrt{3}\kappa\eta \\ \sqrt{3}\kappa\eta & \kappa(8-5\eta) \end{pmatrix},
\end{aligned}
\tag{S3.31}
$$

The local axes (x_i, y_i) for each sublattice $\mathbf{t}_i$ are the ones already defined in Eq. (S3.12), drawn in Fig. S3.3**b**. The columns of $\mathcal{R}_i^{ph}$ are the local axes of site $\mathbf{t}_i$ written in the global Cartesian frame. Its first column, the local x_i axis, points at the centre of one of the two hexagons the site borders. Which of the two is not a property of the site: the frame belongs to the sublattice, so $\mathcal{R}_i^{ph}$ is the same matrix at every $\mathbf{t}_i + \mathbf{R}$ while $+x_i$ and $-x_i$ exchange hexagons as $\mathbf{R}$ changes. The sign is fixed by $\mathcal{R}_i^{ph}$ itself, and its effect is that the three sites surrounding any one hexagon all point their local x at that centre. Fig. S3.3**b** draws that triple, $\mathbf{t}_A$, $\mathbf{t}_B - \mathbf{a}$ and $\mathbf{t}_C - \mathbf{b}$. A displacement therefore transforms as $\mathbf{u}' = \mathcal{R}_i^{ph,\mathsf{T}}\mathbf{u}$ and a force-constant block as $F_{ij}^{\mathrm{loc}} = \mathcal{R}_i^{ph,\mathsf{T}} F_{ij} \mathcal{R}_j^{ph}$, the same convention as Eq. (S3.13). Since only one type of atom is considered in this model, the real-space dynamic matrix $D(\mathbf{R})$ is simply:

$$
D_{i\mu,j\nu}(\mathbf{R}) = \frac{F_{i\mu,j\nu}(\mathbf{R})}{\sqrt{M_i M_j}} = \frac{F_{i\mu,j\nu}(\mathbf{R})}{M}
\tag{S3.32}
$$

where M is the mass. In the local coordinate system (x_i, y_i) for site $\mathbf{t}_i$ (here, owing to the $\mathcal{M}_z$ symmetry, the z axis can be neglected), as defined in Fig. S3.3**b**, the dynamical matrix for the NN kagome spring-ball model in real space takes the following form

$$
D_{AB}[(0,0,0)] = \frac{1}{M}\begin{pmatrix} t_{xx} & t_{xy} \\ -t_{xy} & t_{yy} \end{pmatrix} = D_{BC}[(1,0,0)] = D_{CA}[(0,0,0)]
\tag{S3.33}
$$

where the three blocks are equal because C_3 cycles $A \to B \to C \to A$ together with the local frames. The remaining orientation, $A \to C$, is the transpose,

$$
D_{AC}[(0,0,0)] = D_{CA}[(0,0,0)]^{\mathsf{T}} = \frac{1}{M}\begin{pmatrix} t_{xx} & -t_{xy} \\ t_{xy} & t_{yy} \end{pmatrix},
\tag{S3.34}
$$

where

$$t_{xx} = \frac{\kappa}{2}(2-3\eta), \qquad t_{xy} = \frac{\sqrt{3}\kappa}{2}(2-\eta), \qquad t_{yy} = \frac{\kappa}{2}(2+\eta), \tag{S3.35}$$

and the onsite energies are

$$D_{AA}[(0,0,0)] = \frac{1}{M}\begin{pmatrix}\varepsilon_x & \\ & \varepsilon_y\end{pmatrix} = D_{BB}[(0,0,0)] = D_{CC}[(0,0,0)] \tag{S3.36}$$

where

$$\varepsilon_x = 2\kappa(4-3\eta), \qquad \varepsilon_y = 2\kappa(4-\eta). \tag{S3.37}$$

This indicates that the x-phonon generally has lower onsite energy compared to the y-phonon, which arises from the fact that the horizontal movement involves lower energy and weaker coupling, leading to a smaller bandwidth for the x-phonon. Upon performing the Fourier transformation, the dynamical matrix in $\mathbf{q}$-space becomes:

$$D_{i\mu,j\nu}(\mathbf{q}) = \sum_{\mathbf{R}} e^{i\mathbf{q}\cdot\mathbf{R}} D_{i\mu,j\nu}(\mathbf{R}) \tag{S3.38}$$

where $\mathbf{R} = \mathbf{R}_j - \mathbf{R}_i$ due to translational symmetry. The dynamical matrix $D(\mathbf{q})$ of the kagome spring-ball model in local coordinate, whose eigenvalues are ω^2, is then

$$D(\mathbf{q}) = \frac{1}{M}\begin{pmatrix}
\varepsilon_x & 0 & t_{AxBx}(\mathbf{q}) & t_{AxBy}(\mathbf{q}) & t_{AxCx}(\mathbf{q}) & -t_{AxCy}(\mathbf{q}) \\
 & \varepsilon_y & -t_{AxBy}(\mathbf{q}) & t_{AyBy}(\mathbf{q}) & t_{AxCy}(\mathbf{q}) & t_{AyCy}(\mathbf{q}) \\
 & & \varepsilon_x & 0 & t_{BxCx}(\mathbf{q}) & t_{BxCy}(\mathbf{q}) \\
 & & & \varepsilon_y & -t_{BxCy}(\mathbf{q}) & t_{ByCy}(\mathbf{q}) \\
 & & \dagger & & \varepsilon_x & 0 \\
 & & & & & \varepsilon_y
\end{pmatrix} \tag{S3.39}$$

where

$$\begin{aligned}
&t_{AxBx}(\mathbf{q}) = t_{xx}(1+e^{iq_b}), && t_{AxBy}(\mathbf{q}) = t_{xy}(1+e^{iq_b}), && t_{AyBy}(\mathbf{q}) = t_{yy}(1+e^{iq_b}),\\
&t_{AxCx}(\mathbf{q}) = t_{xx}(1+e^{iq_a}), && t_{AxCy}(\mathbf{q}) = t_{xy}(1+e^{iq_a}), && t_{AyCy}(\mathbf{q}) = t_{yy}(1+e^{iq_a}),\\
&t_{BxCx}(\mathbf{q}) = t_{xx}(e^{iq_a}+e^{-iq_b}), && t_{BxCy}(\mathbf{q}) = t_{xy}(e^{iq_a}+e^{-iq_b}), && t_{ByCy}(\mathbf{q}) = t_{yy}(e^{iq_a}+e^{-iq_b}).
\end{aligned} \tag{S3.40}$$

The two A–B bonds sit at $\mathbf{R} = \mathbf{0}, \mathbf{b}$, the two A–C bonds at $\mathbf{R} = \mathbf{0}, \mathbf{a}$ and the two B–C bonds at $\mathbf{R} = \mathbf{a}, -\mathbf{b}$, which is the origin of the phase factors above. Here, $\mathbf{q} = (q_a, q_b, q_c)$ is the phonon wavevector in direct coordinates in the BZ from Eq. (S3.4). Without loss of generality, the eigenvalues of the spring-ball model Eq. (S3.39) are computed using the parameters $\eta = 0.8$, $\kappa = 1$, and $M = 1$. As demonstrated by the mode-resolved phonon dispersion in Fig. S3.3**c**, numerical analysis confirms that the local x phonon exhibits a roughly two-times lower frequency compared to the local y phonon. The *ab-initio* real-space EPC of the local x and y phonons is nearly equal [Section S3.1.2], yet the contribution to λ from the two is in a ratio of roughly $4:1$ [Fig. S2.16**c**]. This is what the spring-ball frequencies imply, since $\lambda \propto |g|^2/\omega^2$ [Eq. (S2.9)] with g the real-space EPC strength.

The observed degeneracy between the x and y phonon bands (B_{3u}@$3g$ and B_{2u}@$3g$ EBRs) at the K point is accidental and can be lifted by including springs beyond the nearest neighbors. Specifically, when considering the spring connecting the NNN atoms (the spring marked κ_{NNN} in Fig. S3.3**b**), the phonon dispersion changes, as shown in Fig. S3.3**d**.

S4 Tight-binding model and superfluid weight

We construct a simple kagome-lattice model with an attractive interaction to compute the superfluid weight, and find it dominated by the conventional contribution, the geometric part being negligible.

Model and calibration. The tight-binding model is constructed with an on-site energy $E = -0.9259\,\text{eV}$, hopping amplitudes $t_{\text{NN}} = -0.39\,\text{eV}$ and $t_{\text{NNN}} = 0.048\,\text{eV}$ between nearest and next nearest neighbors in the kagome plane, respectively, and an out-of-plane hopping amplitude $t_z = -0.033\,\text{eV}$ between the kagome layers. The resulting band structure is shown in Fig. S4.1(a). Using multiband BCS mean-field theory with an attractive Hubbard-U interaction [73], where $U = 0.205\,\text{eV}$ has been calibrated to yield a superconducting gap of $\Delta \approx 5\,\text{meV}$ at zero temperature, we find a mean-field T_c of 34 K, see Fig. S4.1(b). The gap $\Delta \approx 5\,\text{meV}$ is chosen to match the average gap on the $d_{x^2-y^2}$ FS of the SG 191 phase, as shown in Fig. S2.11**f**. The overestimation of T_c in the model calculation may arise from multiple factors. First, mean-field approximations are known to generally overestimate superconducting transition temperatures. Additionally, the model used is highly simplified, as $LaRu_3Si_2$ possesses multiple FSs, whereas the model calculation primarily focuses on the dominant contribution from $d_{x^2-y^2}$ orbitals. The superconducting gap on other FSs is significantly smaller.

Conventional and geometric contributions. We calculate the superfluid weight tensor D_s for this model, split into its conventional and geometric parts, as described in Refs. [73, 74], and find

$$D_s^{\text{conv}} = \begin{pmatrix} 2.14 \cdot 10^{19} & 0 & 0 \\ 0 & 2.14 \cdot 10^{19} & 0 \\ 0 & 0 & 8.27 \cdot 10^{18} \end{pmatrix}, \tag{S4.1}$$

$$D_s^{\text{geom}} = \begin{pmatrix} 1.89 \cdot 10^{17} & 0 & 0 \\ 0 & 1.89 \cdot 10^{17} & 0 \\ 0 & 0 & 0 \end{pmatrix}, \tag{S4.2}$$

$$D_s = D_s^{\text{conv}} + D_s^{\text{geom}} = \begin{pmatrix} 2.16 \cdot 10^{19} & 0 & 0 \\ 0 & 2.16 \cdot 10^{19} & 0 \\ 0 & 0 & 8.27 \cdot 10^{18} \end{pmatrix}. \tag{S4.3}$$

The components are indexed by the Cartesian coordinates x, y, z, and are expressed in SI-units 1/Hm. The superfluid weight is almost purely conventional, with a difference of two orders of magnitude between the conventional and geometric parts. As D_s is defined as an integral over the BZ, in Fig. S4.2 we show how the integrand behaves around the FS. The x and y components especially show clear peaks in complementing directions around the xy plane, while the contribution to the superfluid weight drops to zero in other directions.

Dependence on gap magnitude and band filling. The large conventional part in the superfluid weight is likely due to the large bandwidth compared with the superconducting gap Δ. As shown in Fig. S4.3, when the superconducting gap Δ increases to the order of the quasi-FB bandwidth $\sim 100\,\text{meV}$, the geometric contribution to the superfluid weight becomes comparable to the conventional part. From the figure one can also see that even if $\Delta \approx 5\,\text{meV}$ is an overestimate for this model, the geometric part would remain much smaller than the conventional part also in case of smaller Δ.

By tuning the chemical potential so that the Fermi energy is lowered by 0.065 eV, roughly corresponding to a maximum of the DOS, the superconducting gap and the T_c are increased by around 70% to 8.5 meV and 57 K, respectively. At this optimal filling, the total superfluid weight increases by around 50%. The relative increase for the geometric part is larger than for the conventional part such that it now accounts for around 2% of the total superfluid weight in the xx and yy directions (compared to 1% above).

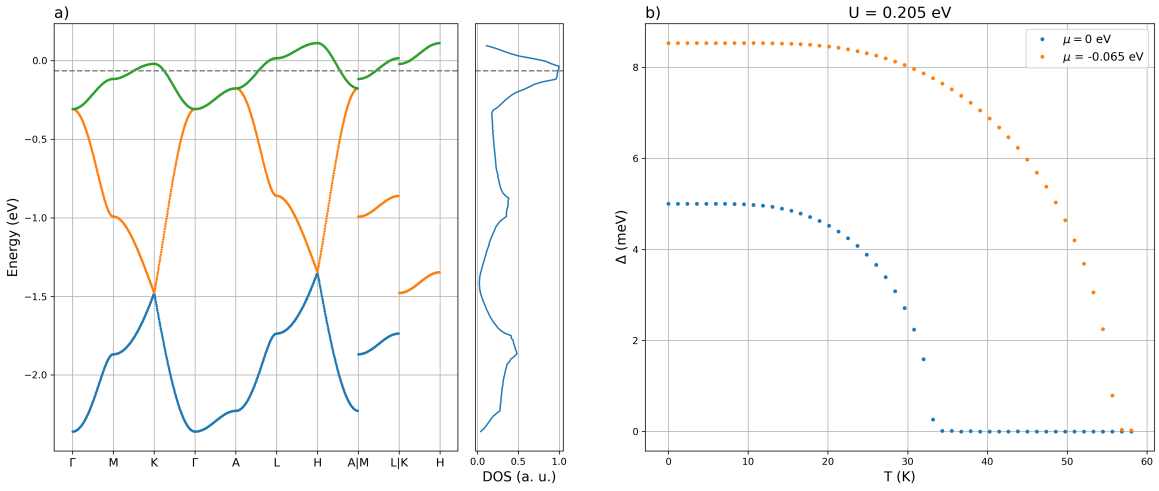


Figure S4.1: (a) The band structure and the DOS of the tight-binding model. The Fermi energy is set to zero. The dashed gray line indicates where the superconducting gap reaches a maximum when the chemical potential is tuned. (b) The superconducting gap Δ as a function of temperature with and without tuning the chemical potential. A slight change in the Fermi energy increases both the gap and the critical temperature by around 70%.

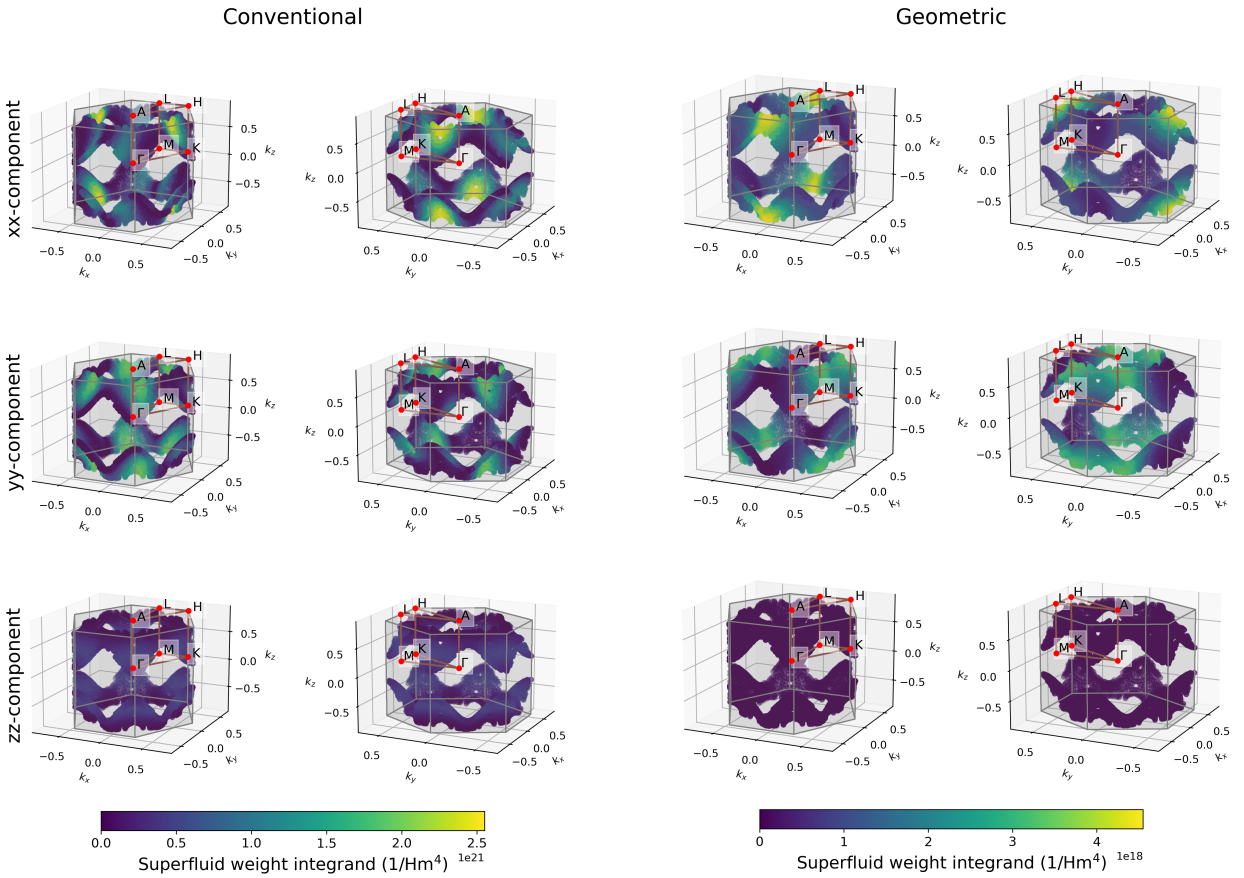


Figure S4.2: The diagonal components of the superfluid weight integrand around the FS. Each plot is shown from two different angles. Note the difference in scales between the conventional and geometric parts, with the conventional part being two orders of magnitude larger than the geometric part.

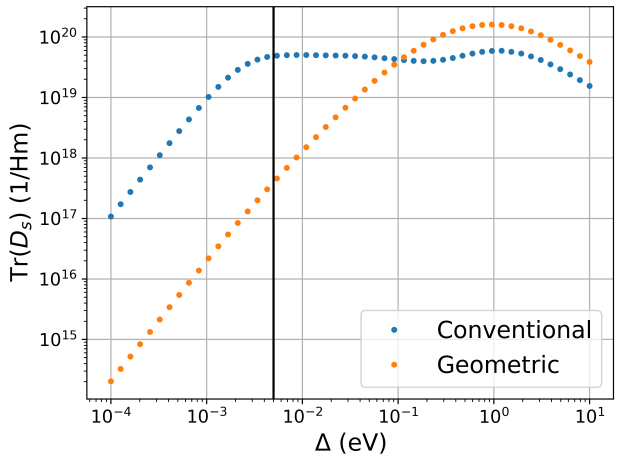


Figure S4.3: The traced conventional and geometric components of the superfluid weight for the tight-binding model in Fig. S4.1(a) are shown, with the black line indicating $\Delta = 5\,\text{meV}$. The geometric contribution becomes comparable to the conventional part when $\Delta \sim 100\,\text{meV}$, at which point the superconducting gap is on the order of the FB bandwidth.

S5 Superconducting candidates in the 1:3:2 family

Section S3 leaves two predictions that are not specific to $LaRu_3Si_2$, and this section tests both of them against the whole 1:3:2 family. The first is geometric. The spring-ball analysis of Section S3.2 places the local x phonon of the kagome net below the local y phonon for *any* masses and spring constants, $\varepsilon_x = 2\kappa(4-3\eta) < \varepsilon_y = 2\kappa(4-\eta)$. Since the *ab initio* real-space couplings of the two modes are nearly equal, 0.0201 against 0.0204 Ry/Bohr [Section S3.1.2], and $\lambda \sim |g|^2/\langle\omega^2\rangle$ [Eq. (S2.9)], the B_{3u} (local x) branch of Fig. S2.3 should dominate λ in any kagome metal, whatever chemistry decorates the net. The second is electronic. Because $\lambda_{\mathbf{q}\nu} \propto D(E_F)$ [Eq. (S2.9)], a kagome-derived quasi-FB that pins a DOS peak near E_F should raise λ at fixed phonon frequency, which is the mechanism established for $LaRu_3Si_2$ in Section S2.5.6. A high-throughput screening is the natural test of both, because it varies the chemistry while holding the kagome net fixed.

The family is a large one. Compounds crystallizing in SG 191 ($P6/mmm$), such as $LaIr_3Ga_2$ [75] and YRu_3Si_2 [76], belong to the 1:3:2 family, also referred to as the RT_3X_2 family, where T is the element forming the kagome net. Several compounds in the 1:3:2 family have been experimentally confirmed to exhibit SC with critical temperatures around 5 K, while some others are predicted by *ab initio* [35–38, 40, 50, 52, 60–67, 75–77]. All of them share the $(1:3:2) = (0:3:3) - (0:0:1) + (1:0:0)$ building block of Section S2.1, hence the same kagome net of T atoms, which is what makes a common underlying mechanism plausible in the first place.

The screening protocol, and the respects in which it differs from the $LaRu_3Si_2$ calculations, are given in Section S1.4. It returns 3063 candidates within 100 meV/atom of the convex hull. Those with $T_c > 1$ K are listed in Tables S5.3 and S5.4, and the thermodynamically most stable among them, $E_{\text{hull}} < 30$ meV/atom, in Tables S5.1 and S5.2 together with their electronic, phononic and EPC properties [Figs. S5.1 and S5.2 and the plates that follow each of them]. In all four tables the formula is written in the site order $R\,X_2\,T_3$ and colored by site, R teal, X blue and T red, so that the red element is always the one carrying the kagome net. The prose keeps the conventional RT_3X_2 order, and $SrIr_3Ni_2$ in the text is $SrNi_2Ir_3$ in the tables. The presence of an FB near E_F, reported in the last column of Tables S5.1 and S5.2, is determined by identifying a local DOS peak within the energy range of $E_F \pm 0.5$ eV. This is the criterion under which the Ru A_g quasi-FB of $LaRu_3Si_2$, some 150 meV below E_F [Section S2.4.1], counts as an FB at E_F.

The candidates split into two groups according to which orbitals build the kagome bands. The first (Section S5.1) closely resembles $LaRu_3Si_2$ and can be considered as its doped analogs, with kagome bands from T d orbitals, and examples include $LaIr_3Ga_2$ and $CaRh_3Ga_2$. In the second (Section S5.2) the T elements are main-group metals, predominantly Al, Be and Ga, so the kagome bands derive from p rather than d electrons, and the electronic structures differ accordingly. Because the spring-ball argument of Section S3.2 refers to the lattice alone, it should apply to both groups, whereas the FB argument need not.

S5.1 Type I: compounds with d-derived kagome bands

As shown by the phonon spectrum and EPC properties in Fig. S5.1 ff., nearly all materials in the first category of the RT_3X_2 family exhibit a common feature in their phonon spectra: the EPC is predominantly contributed by a low-frequency mode, identified as the B_{3u} (local x) phonon mode of the kagome lattice [Fig. S2.3]. In addition to this characteristic of EPC, these compounds universally feature a quasi-FB formed by kagome $d_{x^2-y^2}$ electrons near E_F. This quasi-FB contributes to the FS and leads to a pronounced peak in the DOS near E_F, similar to what is observed in $LaRu_3Si_2$ [Fig. S2.10].

Among the 65 Type I compounds of Table S5.1, the 18 that carry an FB at E_F have $\langle D(E_F)\rangle =$

2.04 against 1.72 for the other 47, $\langle\lambda\rangle = 0.76$ against 0.61, and $\langle T_c\rangle = 5.4\,\mathrm{K}$ against 3.1 K, at an essentially unchanged phonon scale, $\langle\omega_{\log}\rangle = 134\,\mathrm{K}$ against 132 K. With $\omega_{\log}$ held fixed by the chemistry, the whole T_c difference is carried by λ, and λ tracks $D(E_F)$: the $LaRu_3Si_2$ mechanism of Section S2.5.6 reappears as a trend across a chemically diverse set.

Notably, the broad range of available transition metal substitutions provides significant opportunities for tuning the electronic properties of these compounds, effectively acting as a doping mechanism. In most cases, such substitutions lead to electron doping, which shifts the FB associated with the T $d_{x^2-y^2}$ orbitals away from E_F. While electron doping may enhance structural stability, it often reduces the DOS at E_F, potentially leading to a decrease in T_c, as discussed in Section S2.5.6 and observed in Refs. [65–67].

YRu_3B_2, listed at $E_{\mathrm{hull}} = 0$ with an FB at E_F, has since been synthesized and superconducts between 0.63 and 0.81 K [78–80], an order of magnitude below the 6.8 K tabulated for it, so the tabulated T_c ranks candidates rather than predicting them.

S5.2 Type II: compounds with p-derived kagome bands

The second category differs from the first in the orbital character of its kagome bands, which are formed by p electrons rather than d electrons and may therefore carry weaker electron-electron correlations, the p orbitals being the more itinerant. Most of them host a quasi-FB at the Fermi level from kagome p_z orbitals [Fig. S5.2 ff.], typically only partially flat on the $k_z = \pi$ plane but still giving a DOS peak near E_F. The group is markedly less stable than Type I: the mean distance to the convex hull is 60 meV/atom across Table S5.4, against 46 meV/atom for Table S5.3, and only 20 members fall below 30 meV/atom [Table S5.2] as against 65 in Type I. Their predicted T_c are comparable to Type I on average, means 3.2 against 3.1 K and medians 2.7 against 2.5 K, but with a longer tail: the five highest, 10.9-15.0 K, are all Be-kagome $M\mathrm{Be_3Pd_2}$ and $M\mathrm{Be_3Pt_2}$ (M = Ti, Zr, Hf), none of which reaches $E_{\mathrm{hull}} < 30$ meV/atom, and within the stable subset the largest T_c is 3.0 K.

The same comparison within the 20 Type II compounds of Table S5.2 gives $\langle D(E_F)\rangle = 1.60$ against 1.19 but $\langle\lambda\rangle = 0.43$ against 0.49, because the FB compounds here are the Be-based ones, whose phonons are far stiffer, $\langle\omega_{\log}\rangle = 271\,\mathrm{K}$ against 180 K, so the gain in DOS is spent against the $1/\langle\omega^2\rangle$ of Eq. (S2.9). A quasi-FB at E_F therefore raises T_c only when it is not paid for by a stiffer lattice, which is why the FB argument of the main text is made for $LaRu_3Si_2$ and its close analogs and not for the screened set as a whole.

The EPC nevertheless keeps the defining feature of Type I and of $LaRu_3Si_2$ [Fig. S2.17]: λ is still dominated by the low-frequency B_{3u} kagome-x phonons [Fig. S5.2 ff.], as Section S3.2 requires of the kagome geometry alone. That this survives both the chemical range of the screening and the change from d to p kagome bands is the sense in which the mode selectivity belongs to the lattice rather than to $LaRu_3Si_2$.

S5.3 Scope of the screening

Two limits of this dataset should be kept in mind when reading the tables against the main text.

First, the FB statement of the main text is established for $LaRu_3Si_2$ and holds as a trend among the Type I compounds that share its three ingredients, a kagome-derived quasi-FB near E_F, an enhanced DOS and a strongly coupled low-frequency B_{3u} branch, $CaRh_3Ga_2$, $SrRh_3Ga_2$, YRu_3B_2 [78–80] and $LuRu_3B_2$ [80] among them. It is not a criterion the screened set satisfies as a whole, and the Type II comparison above shows where it breaks.

Second, several compounds with high predicted T_c carry no FB near E_F at all, their λ dominated instead by very soft phonons, which the harmonic $\lambda \sim 1/\langle\omega^2\rangle$ amplifies without bound. The same effect inflates λ by a factor of 5.3 in the unstable SG 191 phase of $LaRu_3Si_2$ itself, where 4.788 collapses to 0.9089 once the soft modes are removed in SG 66 [Table S2.4], so a large computed EPC there signals proximity to a lattice instability more reliably than a high T_c. Compounds that develop instabilities only upon Fourier interpolation were retained but flagged [Section S1.4], and as in $LaRu_3Si_2$ they may well stabilize in a lower-symmetry ground state [70], which we leave to future work.

The dataset is therefore best read as a map of stable candidates within one structural family, spanning several routes to EPC-enhanced SC, rather than as support for a single universal mechanism. What it does establish family-wide is the geometric statement of Section S3.2: the kagome B_{3u} branch dominates the coupling everywhere in the family, and the FB decides whether that coupling is put to use.

S5.4 Candidate tables and spectral data

Tables S5.1 and S5.2 list the lower-energy-above-hull subsets discussed in Sections S5.1 and S5.2, with their spectra shown in Figs. S5.1 and S5.2 and the plates that follow each of them. Tables S5.3 and S5.4 provide the broader candidate lists.

Table S5.1: Predicted compounds with $E_{\text{hull}} < 30\,\text{meV/atom}$ in Type I. Formulas are written in the site order RX_2T_3 and colored by site, R teal, X blue and T red, so the red element is the one carrying the kagome net. The text uses the conventional RT_3X_2 order. $D(E_F)$ is the density of states per spin and per unit cell at the Fermi level. The last column marks a local DOS peak within $E_F \pm 0.5\,\text{eV}$ (Section S5).

Formula	Material ID	E_{hull} (meV/atom)	$\omega_{\log}$ (K)	$D(E_F)$ (eV^{-1})	λ	T_c (K)	FB @ E_F
TmB_2Ir_3	agm002137253	0	73	0.98	1.45	9.2	No
ErB_2Ir_3	agm003202452	0	85	0.98	1.20	8.5	No
CeB_2Os_3	agm002199385	27	131	1.99	0.89	8.1	Yes
$PrAl_2Ir_3$	agm002195389	25	89	1.65	1.11	7.9	Yes
$SrNi_2Ir_3$	agm002226323	0	94	3.21	1.02	7.3	Yes
LuB_2Rh_3	agm003195416	21	127	1.07	0.85	7.2	No
$LaGa_2Ir_3$	agm002274867	0	80	1.62	1.10	6.9	Yes
TbB_2Ru_3	agm003202167	0	137	1.96	0.81	6.9	Yes
YB_2Ru_3	agm003202168	0	165	1.96	0.74	6.8	Yes
SmB_2Ir_3	agm002137232	3	112	1.07	0.88	6.8	No
$PrGa_2Ir_3$	agm002274922	0	90	1.61	1.00	6.7	Yes
PmB_2Ru_3	agm071840373	12	162	2.07	0.74	6.7	Yes
SmB_2Ru_3	agm003195414	7	157	2.04	0.74	6.5	Yes
NdB_2Ru_3	agm003195435	21	166	2.12	0.71	6.3	Yes
TmB_2Rh_3	agm002137195	13	144	1.09	0.75	6.2	No
LaB_2Ru_3	agm003195432	23	166	2.12	0.71	6.2	Yes

Continued on next page

Table S5.1 – continued from previous page

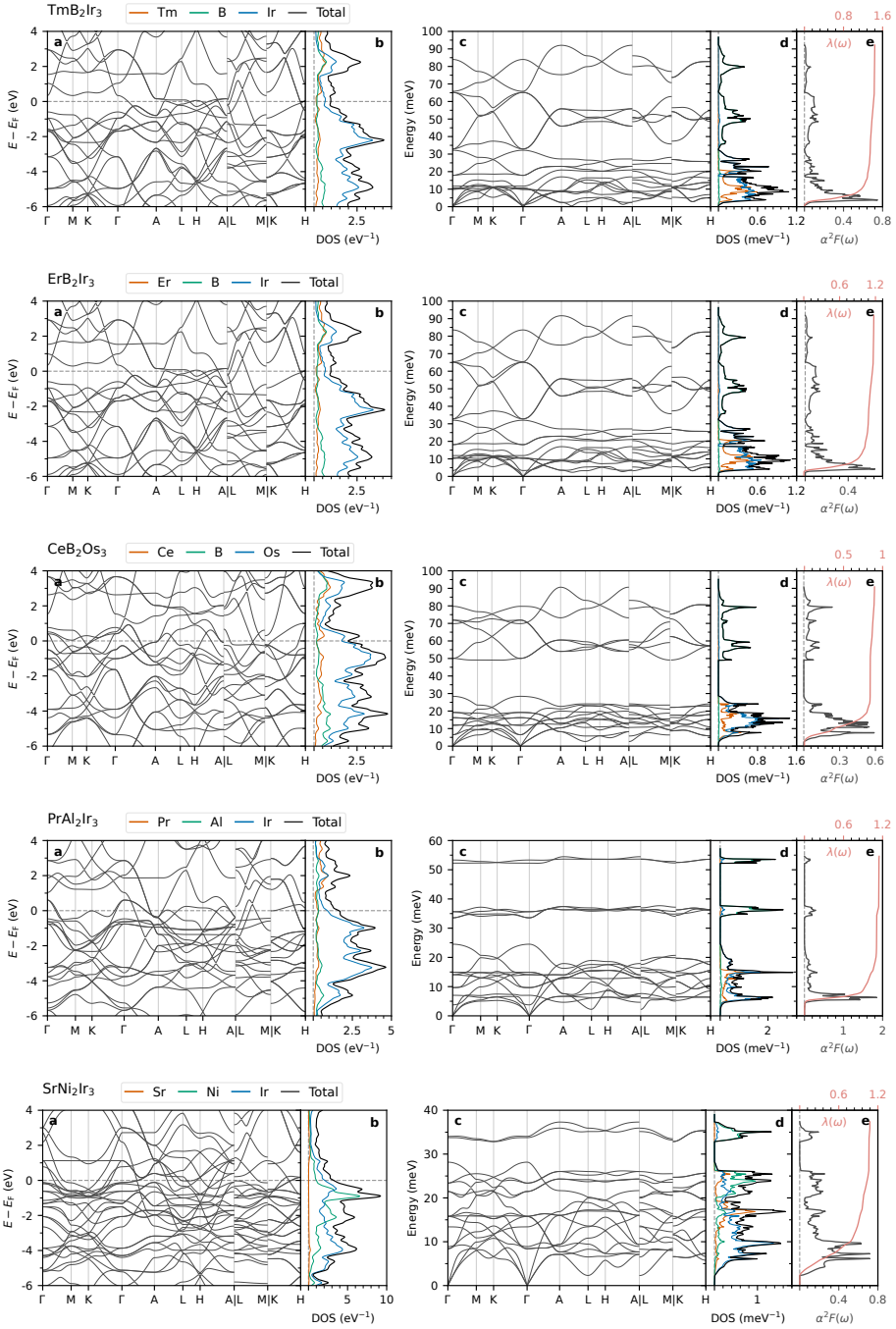
Formula	Material ID	E_{hull} (meV/atom)	$\omega_{\log}$ (K)	$D(E_F)$ (eV^{-1})	λ	T_c (K)	FB @ E_F
CeB_2Ru_3	agm003202683	0	178	2.19	0.67	5.9	Yes
$CaGa_2Rh_3$	agm002260176	0	117	1.76	0.80	5.8	Yes
LaB_2Rh_3	agm003202760	17	180	1.33	0.66	5.7	No
ErB_2Rh_3	agm003195426	8	152	1.10	0.70	5.5	No
HoB_2Rh_3	agm003195417	5	158	1.11	0.67	5.1	No
LaB_2Ir_3	agm003195415	23	130	1.10	0.72	5.1	No
DyB_2Rh_3	agm003195430	2	162	1.13	0.66	5.0	No
TbB_2Rh_3	agm002137193	1	167	1.15	0.64	4.7	No
YB_2Rh_3	agm003202164	0	175	1.14	0.62	4.6	No
$SmAu_2Zn_3$	agm002324461	0	90	1.28	0.80	4.4	No
$TbAu_2Zn_3$	agm002324476	0	90	1.21	0.77	4.0	No
$LaAu_2Zn_3$	agm002246263	0	103	1.50	0.71	3.9	No
KGe_2Pt_3	agm038799382	25	93	1.25	0.74	3.8	No
$ErNi_2Ir_3$	agm002225978	25	127	2.51	0.62	3.2	No
$HoNi_2Ir_3$	agm002226083	18	131	2.51	0.61	3.2	No
$SrGa_2Rh_3$	agm002275043	0	132	1.65	0.60	3.1	Yes
$DyNi_2Ir_3$	agm002225968	12	136	2.51	0.58	2.8	No
$TbNi_2Ir_3$	agm002226335	5	140	2.53	0.56	2.7	No
YNi_2Ir_3	agm002226370	11	143	2.54	0.55	2.6	No
$PmAu_2Zn_3$	agm031465753	0	110	1.30	0.60	2.6	No
$PrAu_2Zn_3$	agm002324445	0	114	1.35	0.59	2.5	No
KIn_2Au_3	agm040038476	27	54	0.92	0.76	2.3	No
$NdAu_2Zn_3$	agm002324425	0	114	1.32	0.57	2.3	No
$BaLi_2Cd_3$	agm071678116	16	103	1.90	0.57	2.1	Yes
$SmNi_2Ir_3$	agm002226250	0	149	2.56	0.52	2.1	No
$PmNi_2Ir_3$	agm005853112	0	151	2.57	0.50	2.0	No
$LaNi_2Ir_3$	agm002167274	0	152	2.68	0.50	1.8	No
$DyNi_2Rh_3$	agm002167305	23	143	2.99	0.50	1.7	No
$TbAg_2Zn_3$	agm002360031	14	108	1.28	0.53	1.7	No
$PrNi_2Ir_3$	agm002226175	0	157	2.60	0.48	1.7	No
$SrLi_2Cd_3$	agm071725069	23	102	1.71	0.54	1.7	No
$SrAu_2Zn_3$	agm002324467	18	121	1.25	0.51	1.6	No
$TbNi_2Rh_3$	agm002167312	17	150	3.01	0.48	1.6	No
NaB_2Ir_3	agm005806208	2	185	1.12	0.46	1.6	No
$LaAg_2Zn_3$	agm002324396	0	118	1.43	0.51	1.6	No
$PmPt_2Rh_3$	agm031020160	28	159	2.59	0.47	1.5	No
$CeNi_2Ir_3$	agm002227628	0	160	2.64	0.46	1.4	No
$CeBe_2Co_3$	agm038805054	28	201	3.34	0.44	1.4	Yes
$NaAu_2Zn_3$	agm039946149	14	114	1.04	0.50	1.4	No
$PrPt_2Rh_3$	agm002235386	28	165	2.62	0.45	1.3	No
$LaPt_2Rh_3$	agm002180579	22	160	2.69	0.45	1.3	No
$BaPd_2Zn_3$	agm002360061	28	117	1.46	0.49	1.3	No
$BaGa_2Rh_3$	agm002337544	0	135	1.53	0.47	1.3	Yes

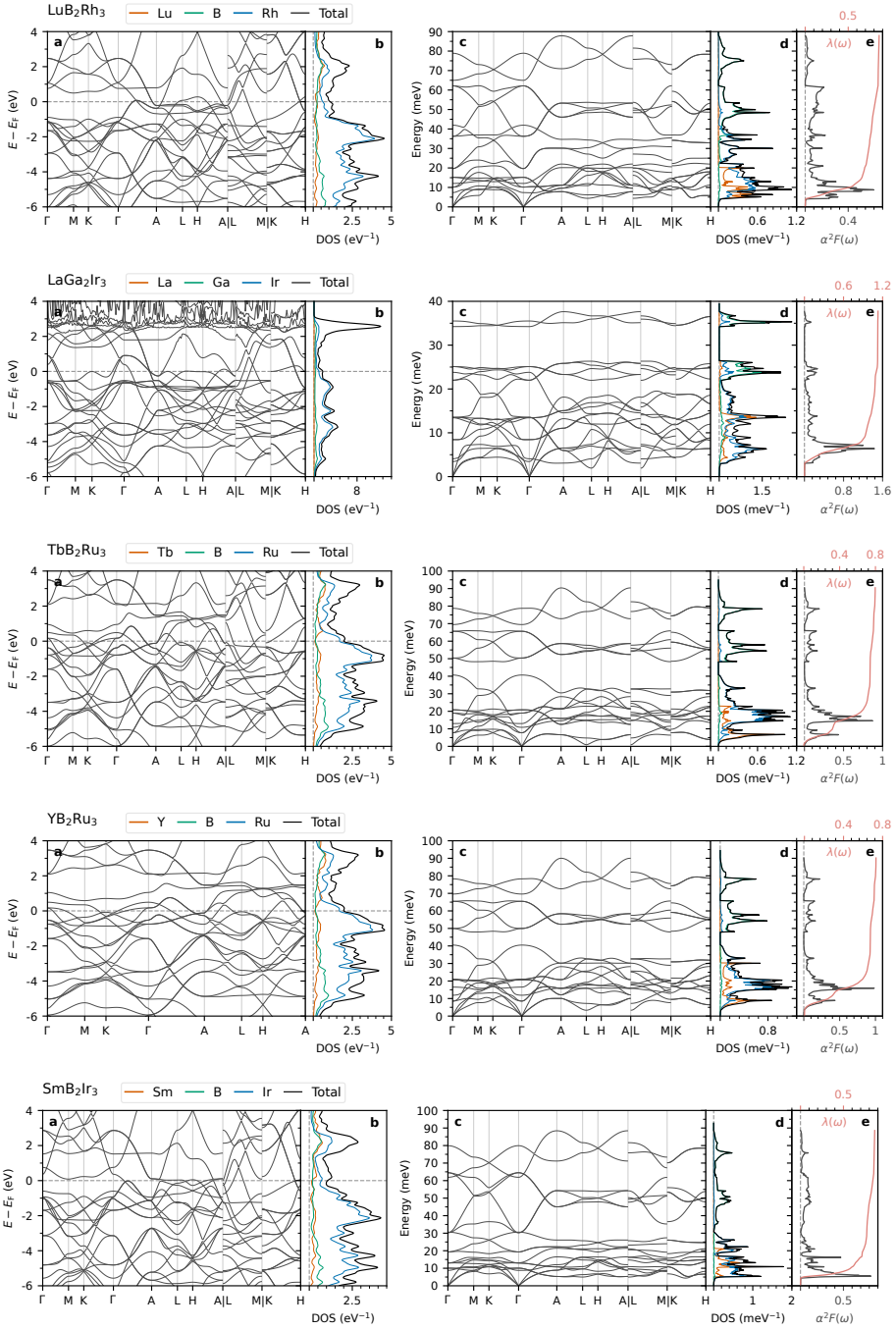
Continued on next page

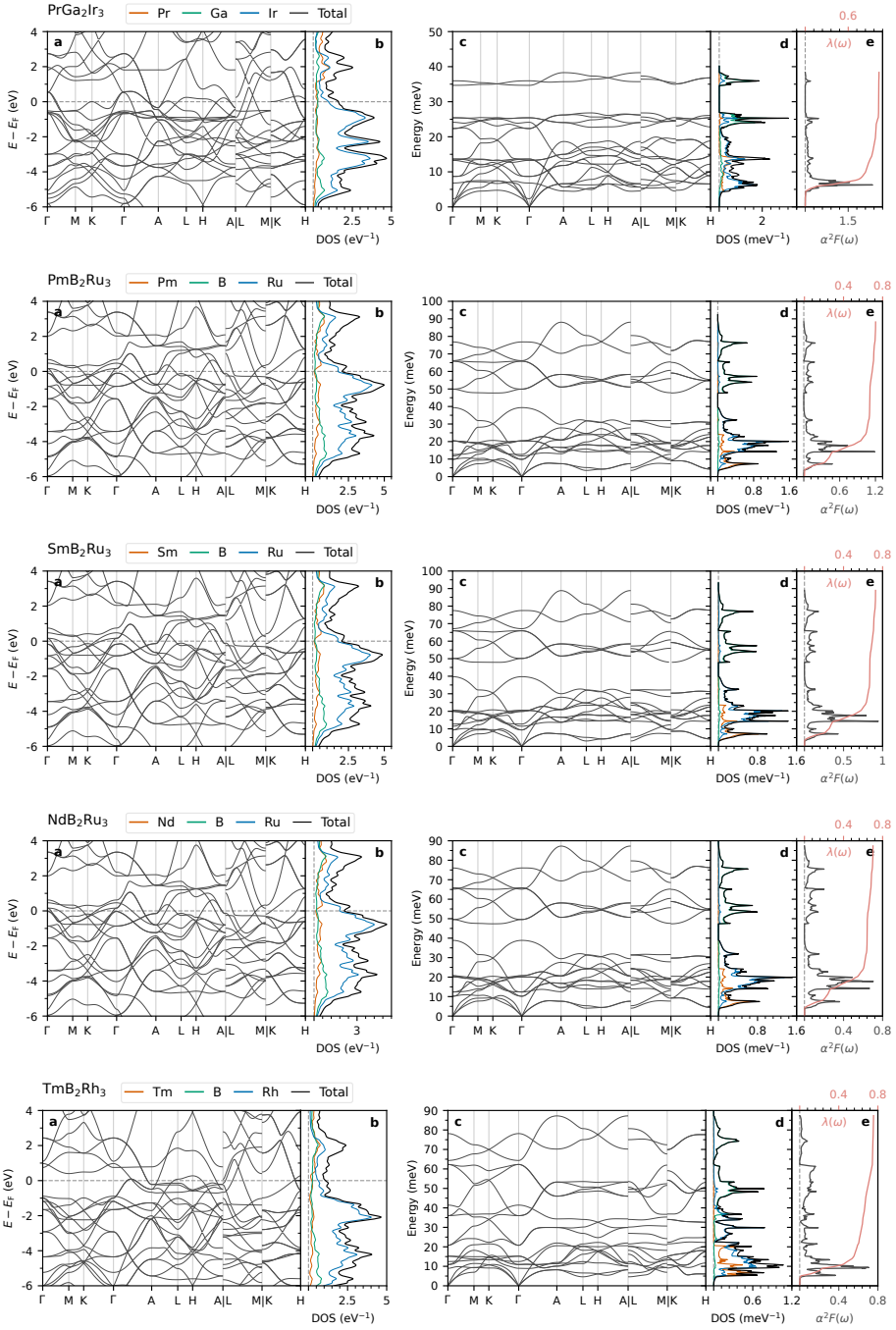
Table S5.1 – continued from previous page

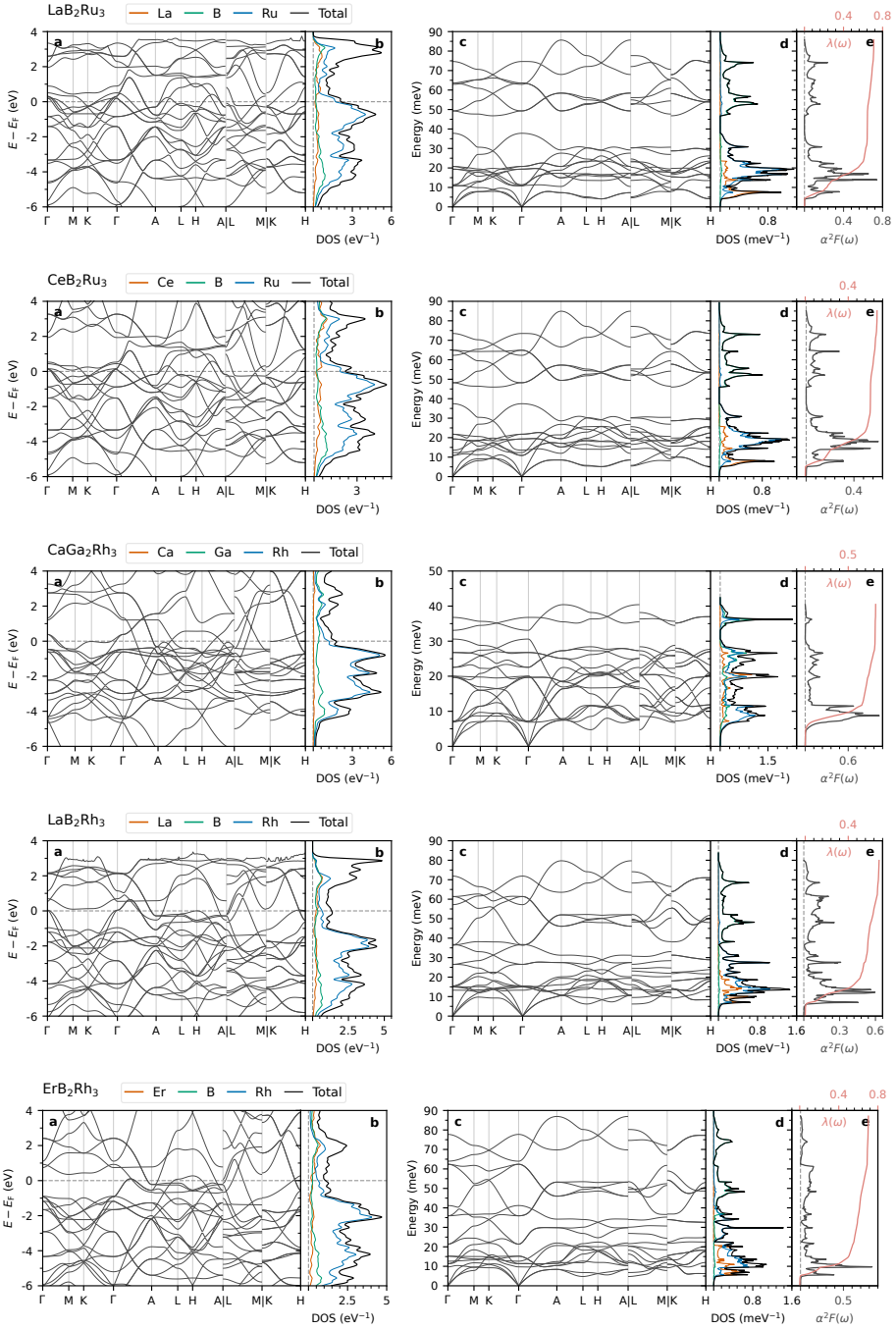
Formula	Material ID	E_{hull} (meV/atom)	$\omega_{\log}$ (K)	$D(E_F)$ (eV^{-1})	λ	T_c (K)	FB @ E_F
$SmAg_2Zn_3$	agm002360030	2	120	1.30	0.48	1.2	No
$SmNi_2Rh_3$	agm002167311	1	167	3.04	0.44	1.2	No
$LaPd_2Zn_3$	agm002246275	0	145	1.73	0.45	1.1	No
$LaPd_2Pt_3$	agm002234138	0	103	2.04	0.47	1.0	Yes
$PrAg_2Zn_3$	agm002360029	0	126	1.31	0.45	1.0	No
$SrAg_2Zn_3$	agm002360072	0	124	1.33	0.45	1.0	No

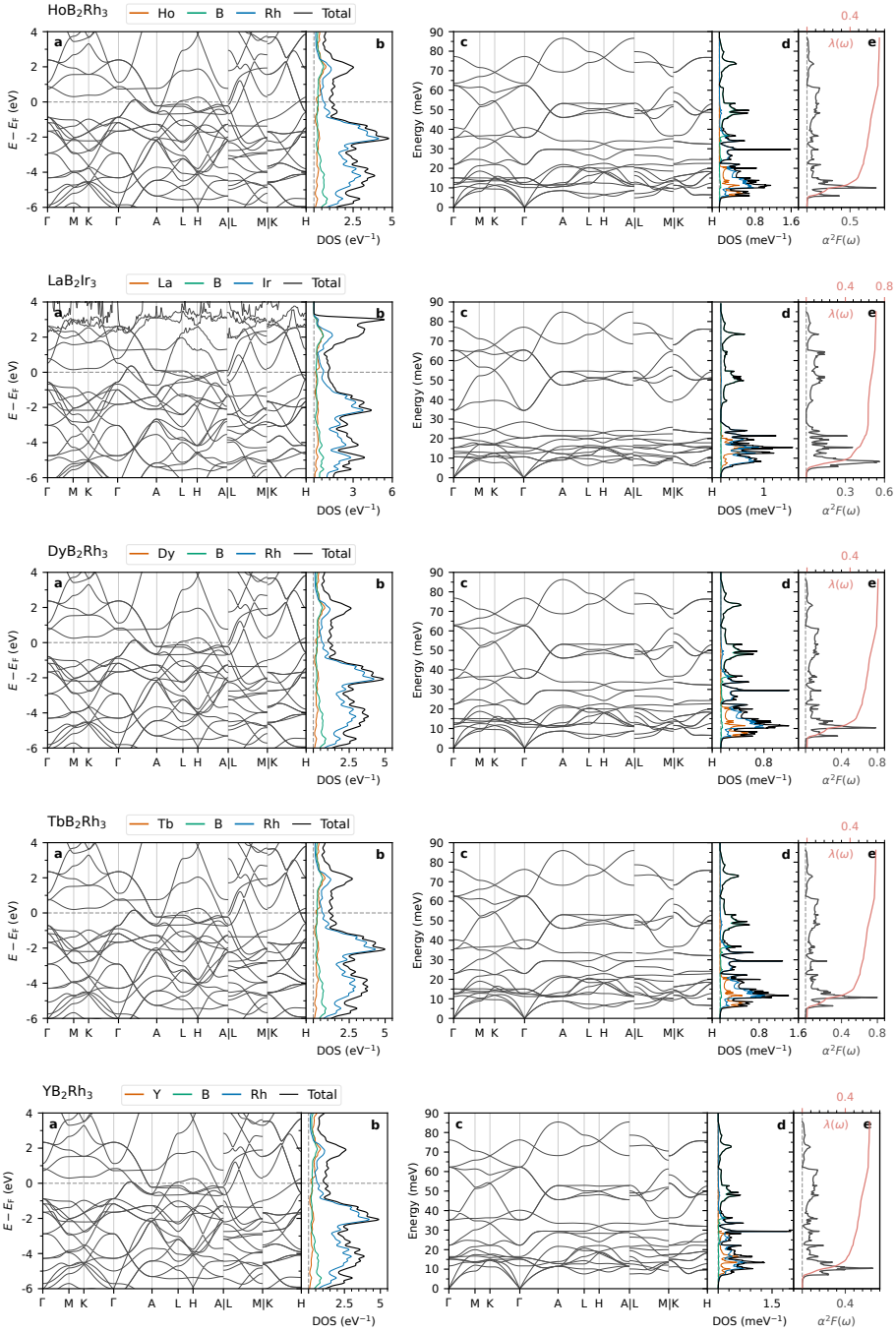
Figure S5.1: Electronic band, electronic DOS, phononic band, phononic DOS and Eliashberg spectral function of materials listed in Table S5.1.

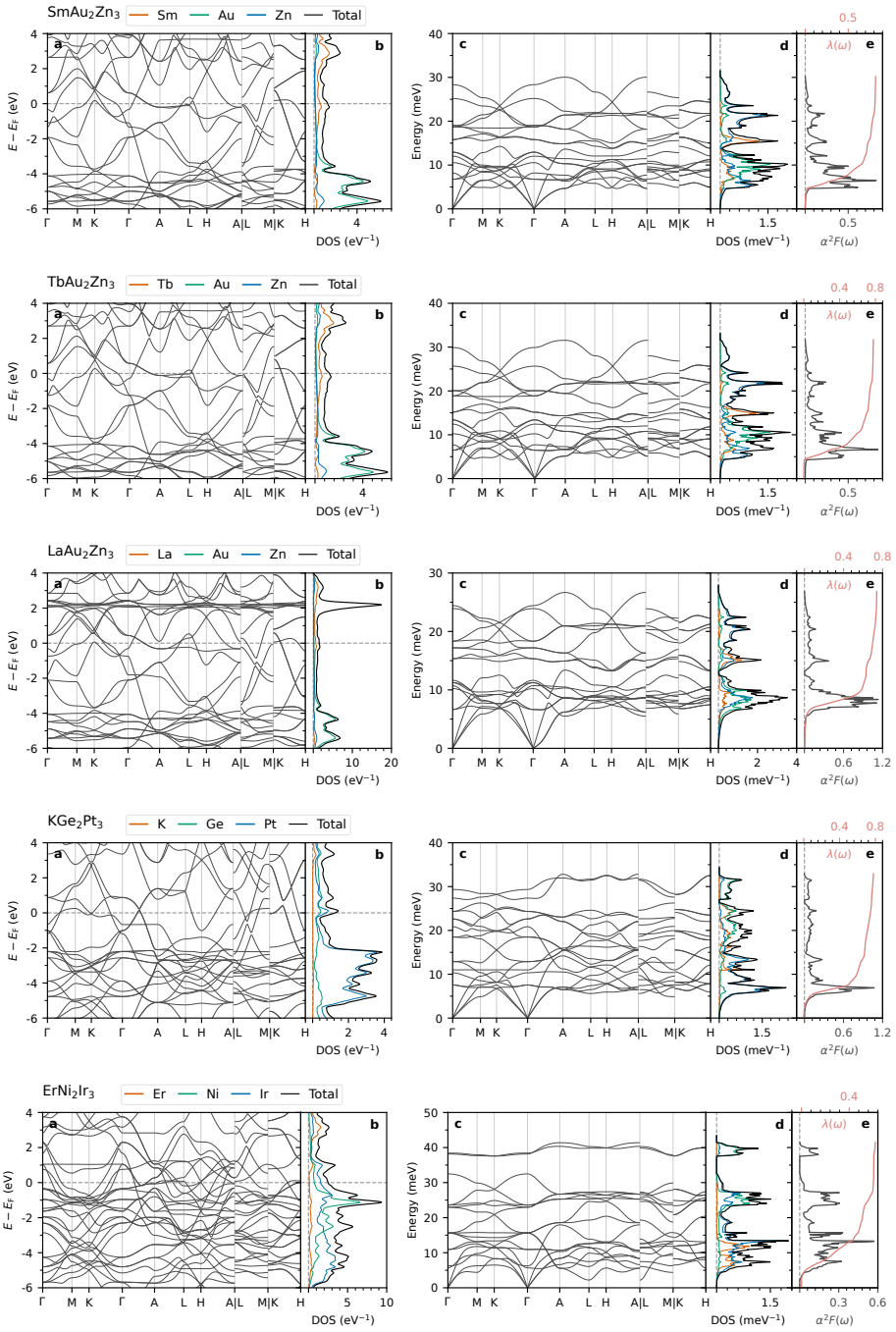


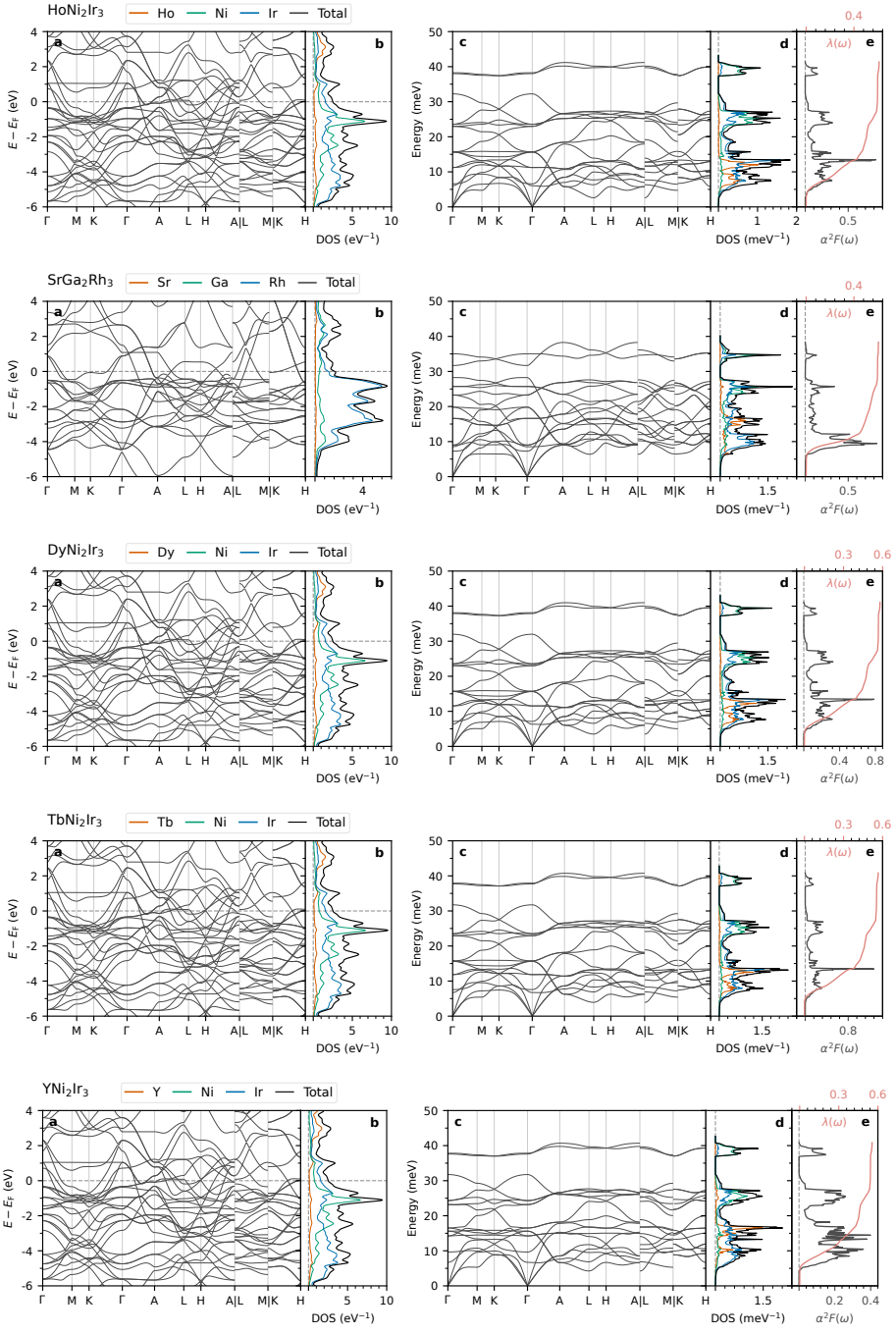

LuB2Rh3
Lu
B
Rh
Total
LaGa2Ir3
La
Ga
Ir
Total
TbB2Ru3
Tb
B
Ru
Total
YB2Ru3
Y
B
Ru
Total
SmB2Ir3
Sm
B
Ir
Total
a
b
c
d
e
E − Ef (eV)
Energy (meV)
DOS (eV−1)
DOS (meV−1)
α2F(ω)
λ(ω)
Γ M K Γ A L H A|L M|K H

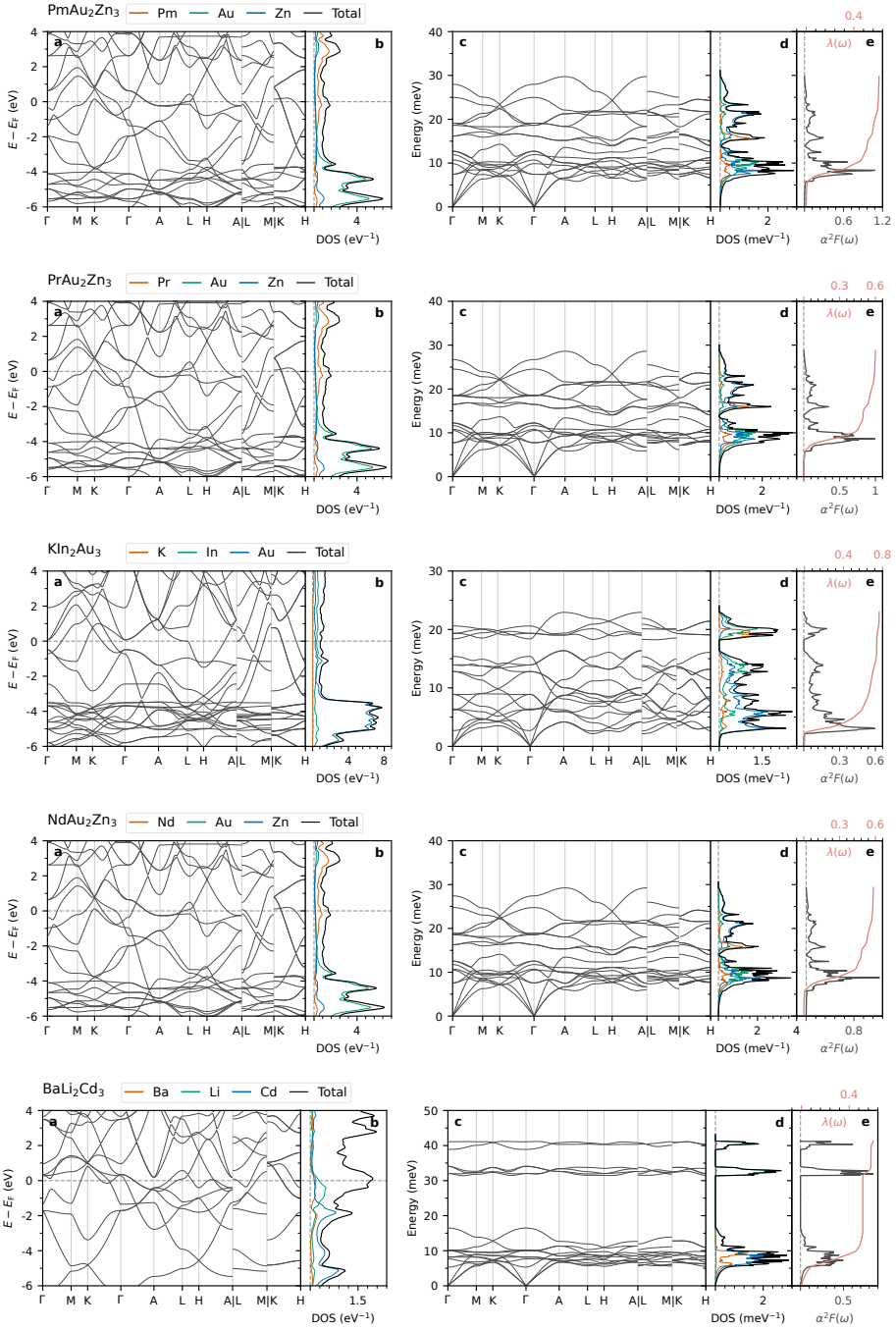

PrGa2Ir3
Pr
Ga
Ir
Total
PmB2Ru3
Pm
B
Ru
Total
SmB2Ru3
Sm
B
Ru
Total
NdB2Ru3
Nd
B
Ru
Total
TmB2Rh3
Tm
B
Rh
Total
a
b
c
d
e
E − Ef (eV)
Energy (meV)
Γ M K Γ A L H A|L M|K H
DOS (eV−1)
DOS (meV−1)
λ(ω)
α2F(ω)

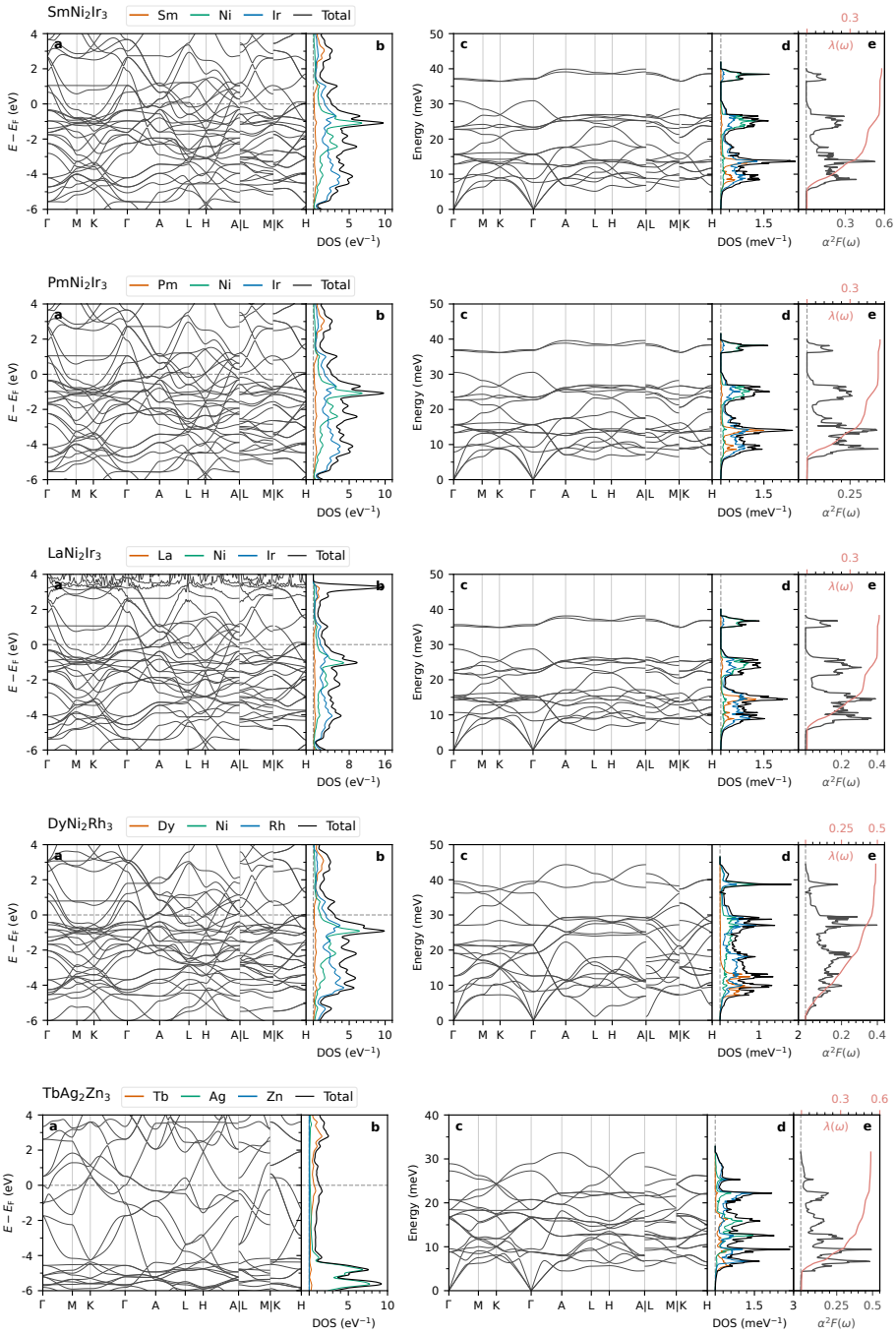

LaB2Ru3
La
B
Ru
Total
CeB2Ru3
Ce
B
Ru
Total
CaGa2Rh3
Ca
Ga
Rh
Total
LaB2Rh3
La
B
Rh
Total
ErB2Rh3
Er
B
Rh
Total
a
b
c
d
e
E − Ef (eV)
Energy (meV)
Γ M K Γ A L H A|L M|K H
DOS (eV−1)
DOS (meV−1)
λ(ω)
α2F(ω)

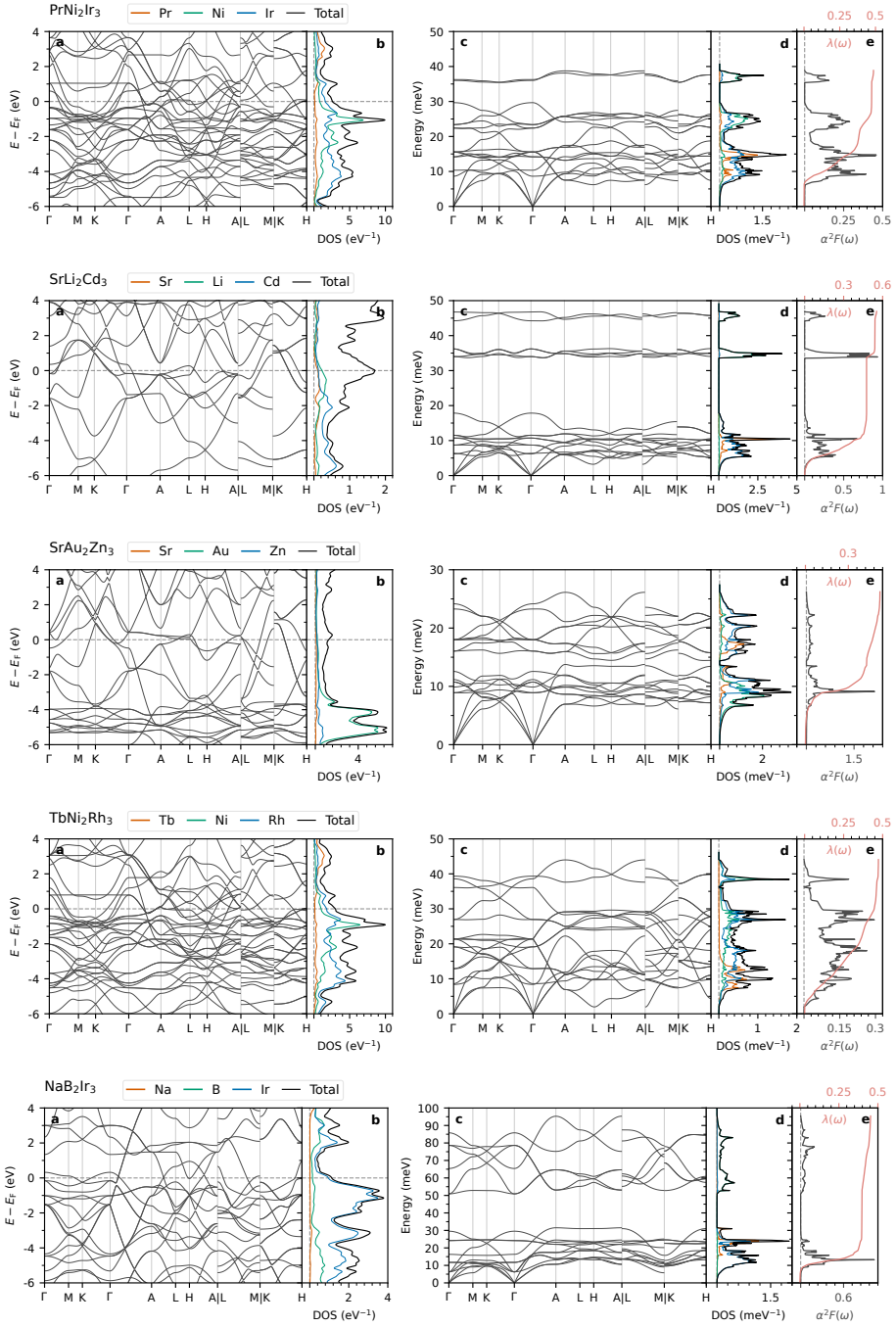

HoB2Rh3
Ho B Rh Total
LaB2Ir3
La B Ir Total
DyB2Rh3
Dy B Rh Total
TbB2Rh3
Tb B Rh Total
YB2Rh3
Y B Rh Total
a
b
c
d
e
E − Ef (eV)
Energy (meV)
Γ M K Γ A L H A|L M|K H
DOS (eV−1)
DOS (meV−1)
λ(ω)
α2F(ω)

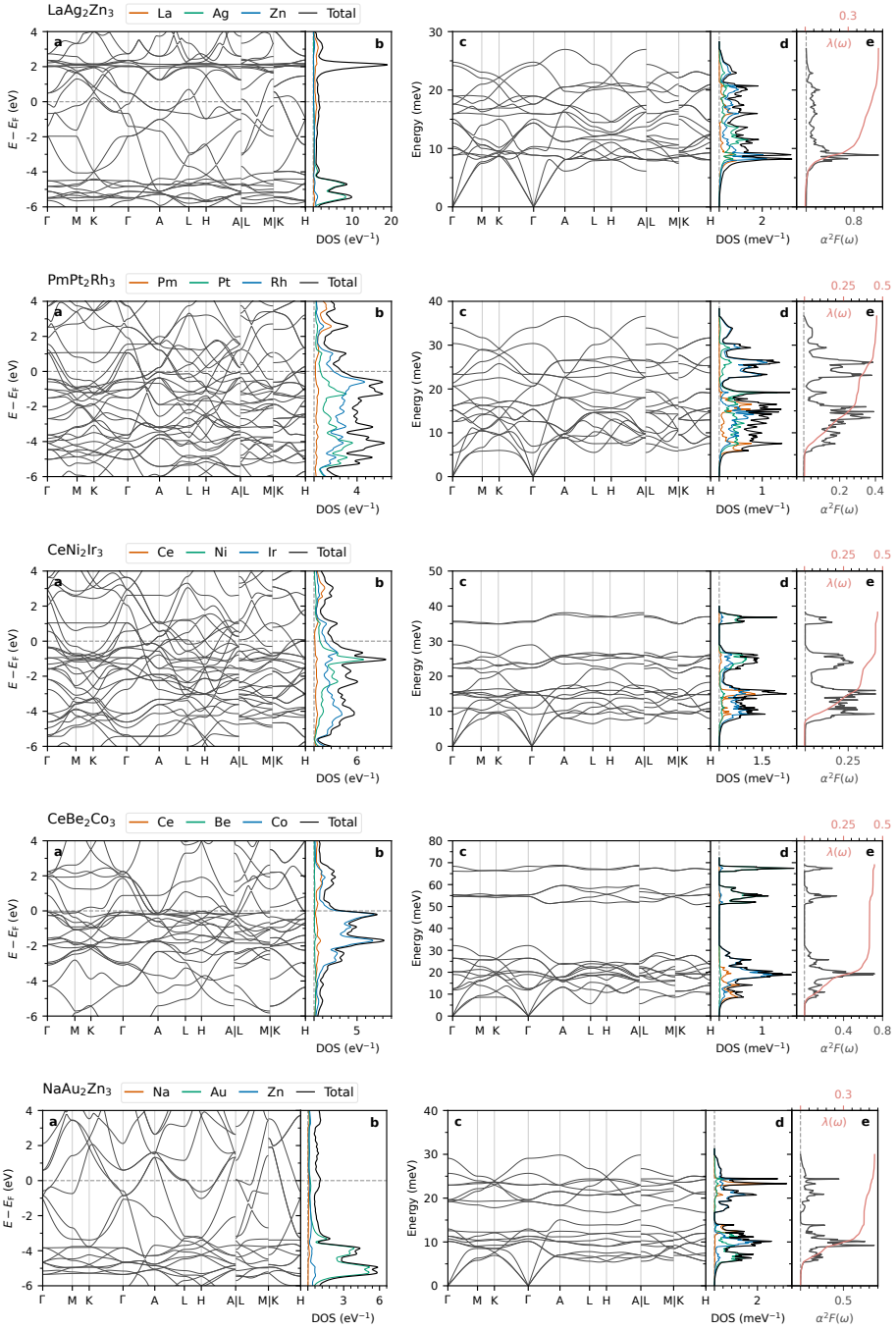

SmAu2Zn3
Sm
Au
Zn
Total
TbAu2Zn3
Tb
Au
Zn
Total
LaAu2Zn3
La
Au
Zn
Total
KGe2Pt3
K
Ge
Pt
Total
ErNi2Ir3
Er
Ni
Ir
Total
a
b
c
d
e
E − Ef (eV)
Energy (meV)
DOS (eV−1)
DOS (meV−1)
α2F(ω)
λ(ω)
Γ M K Γ A L H A|L M|K H

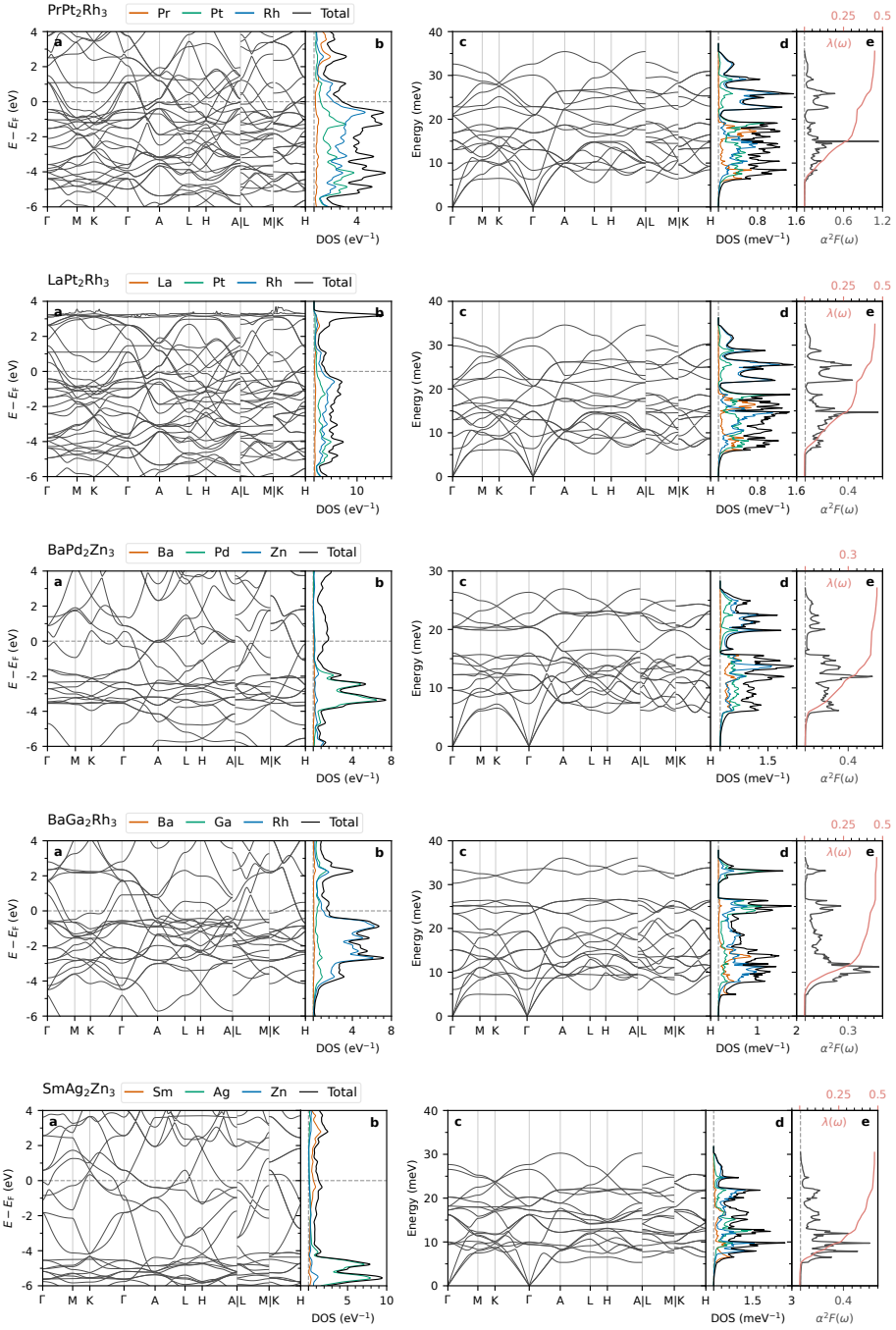

HoNi2Ir3
Ho
Ni
Ir
Total
SrGa2Rh3
Sr
Ga
Rh
Total
DyNi2Ir3
Dy
Ni
Ir
Total
TbNi2Ir3
Tb
Ni
Ir
Total
YNi2Ir3
Y
Ni
Ir
Total
a
b
c
d
e
E − Ef (eV)
Energy (meV)
Γ M K Γ A L H A|L M|K H
DOS (eV−1)
DOS (meV−1)
λ(ω)
α2F(ω)


PmAu2Zn3
Pm
Au
Zn
Total
PrAu2Zn3
Pr
Au
Zn
Total
KIn2Au3
K
In
Au
Total
NdAu2Zn3
Nd
Au
Zn
Total
BaLi2Cd3
Ba
Li
Cd
Total
a
b
c
d
e
E − Ef (eV)
DOS (eV−1)
Energy (meV)
DOS (meV−1)
λ(ω)
α2F(ω)
Γ M K Γ A L H A|L M|K H


SmNi2Ir3
Sm
Ni
Ir
Total
PmNi2Ir3
Pm
Ni
Ir
Total
LaNi2Ir3
La
Ni
Ir
Total
DyNi2Rh3
Dy
Ni
Rh
Total
TbAg2Zn3
Tb
Ag
Zn
Total
a
b
c
d
e
E − Ef (eV)
Energy (meV)
DOS (eV−1)
DOS (meV−1)
α2F(ω)
λ(ω)
Γ M K Γ A L H A|L M|K H


PrNi2Ir3
Pr
Ni
Ir
Total
SrLi2Cd3
Sr
Li
Cd
Total
SrAu2Zn3
Sr
Au
Zn
Total
TbNi2Rh3
Tb
Ni
Rh
Total
NaB2Ir3
Na
B
Ir
Total
a
b
c
d
e
E − Ef (eV)
Energy (meV)
DOS (eV−1)
DOS (meV−1)
α2F(ω)
λ(ω)
Γ M K Γ A L H A|L M|K H


LaAg2Zn3
La
Ag
Zn
Total
PmPt2Rh3
Pm
Pt
Rh
Total
CeNi2Ir3
Ce
Ni
Ir
Total
CeBe2Co3
Ce
Be
Co
Total
NaAu2Zn3
Na
Au
Zn
Total
a
b
c
d
e
E − Ef (eV)
Energy (meV)
DOS (eV−1)
DOS (meV−1)
α2F(ω)
λ(ω)
Γ M K Γ A L H A|L M|K H


PrPt2Rh3
Pr
Pt
Rh
Total
LaPt2Rh3
La
Pt
Rh
Total
BaPd2Zn3
Ba
Pd
Zn
Total
BaGa2Rh3
Ba
Ga
Rh
Total
SmAg2Zn3
Sm
Ag
Zn
Total
a
b
c
d
e
E − Ef (eV)
DOS (eV−1)
Energy (meV)
DOS (meV−1)
λ(ω)
α2F(ω)
Γ M K Γ A L H A|L M|K H

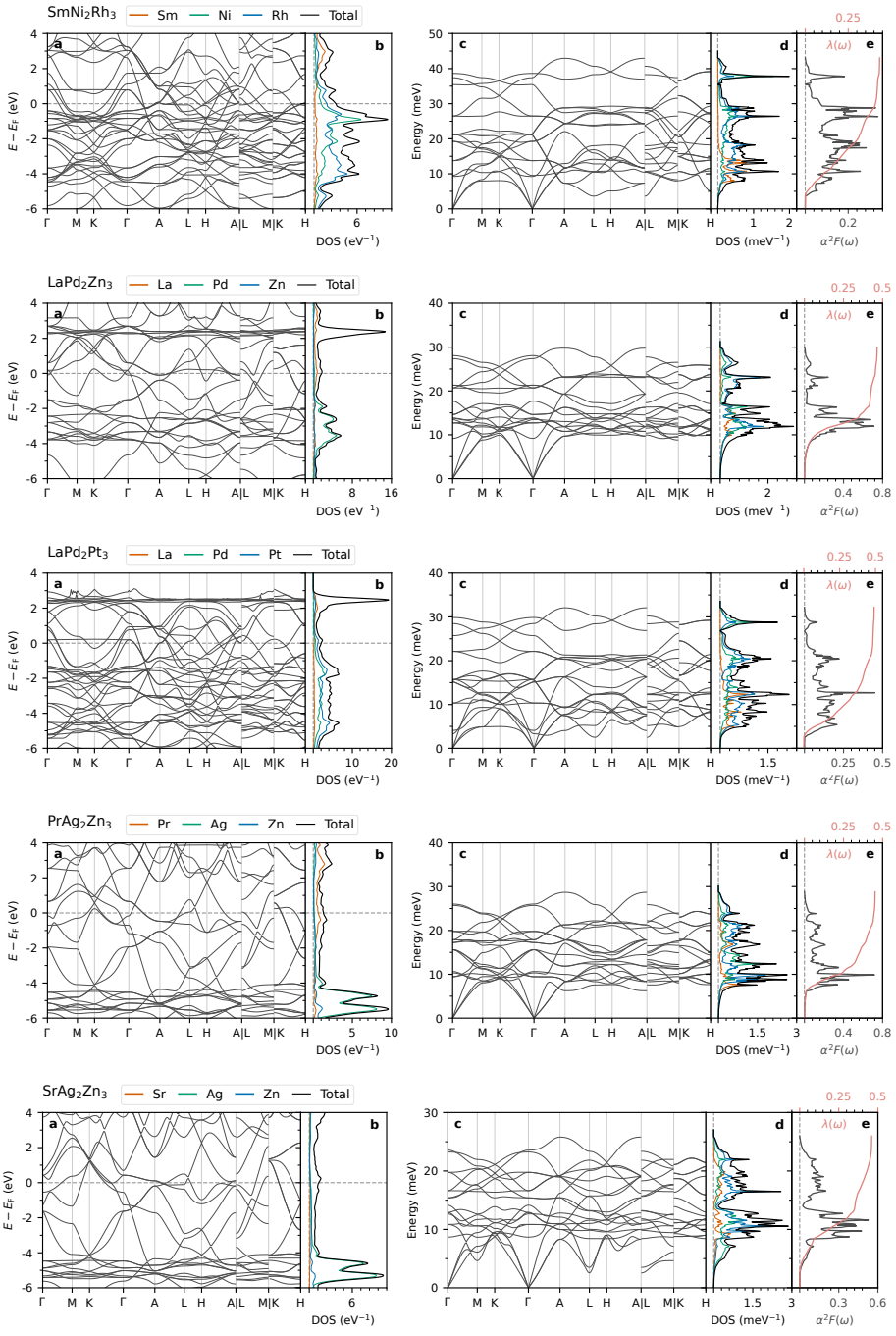
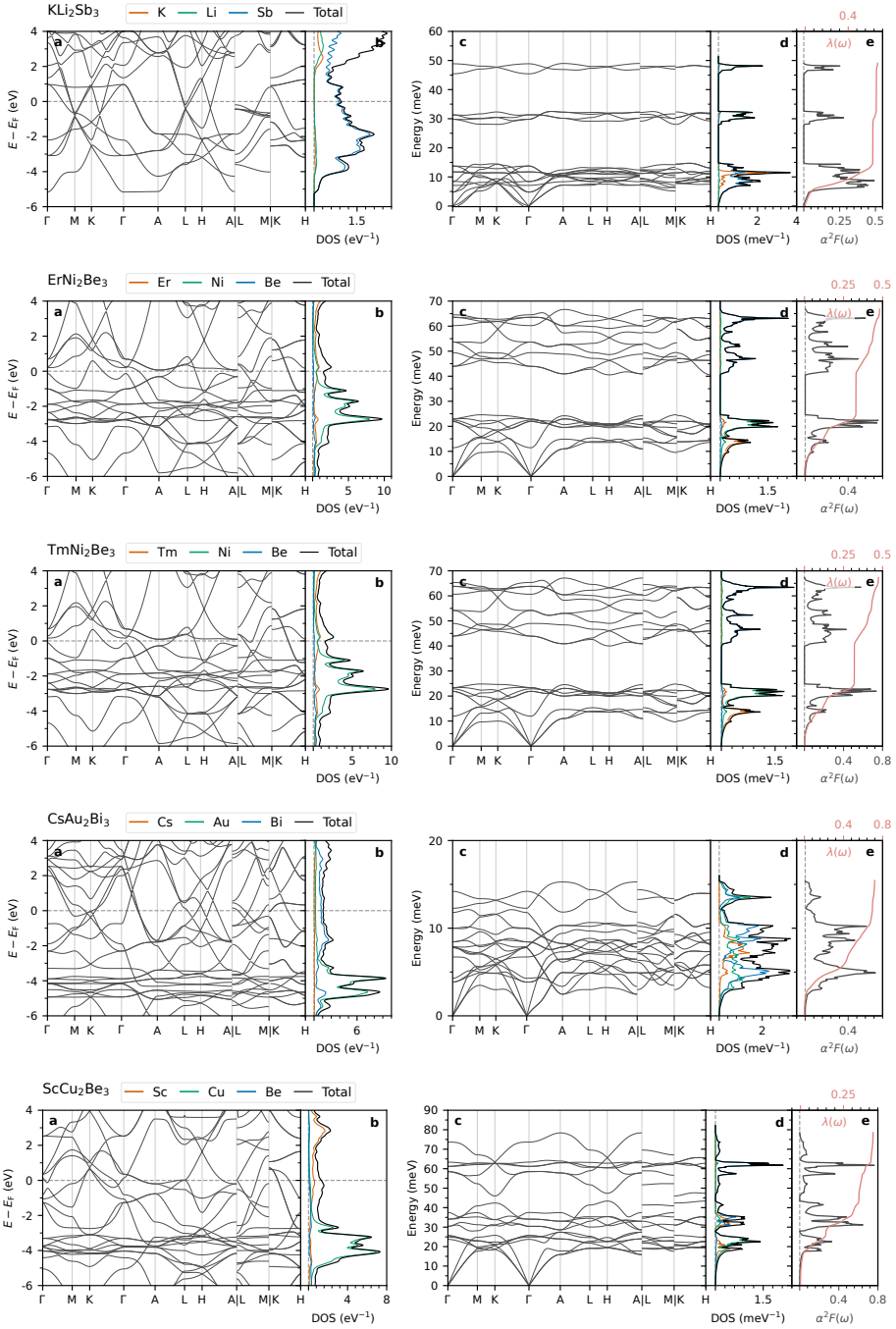
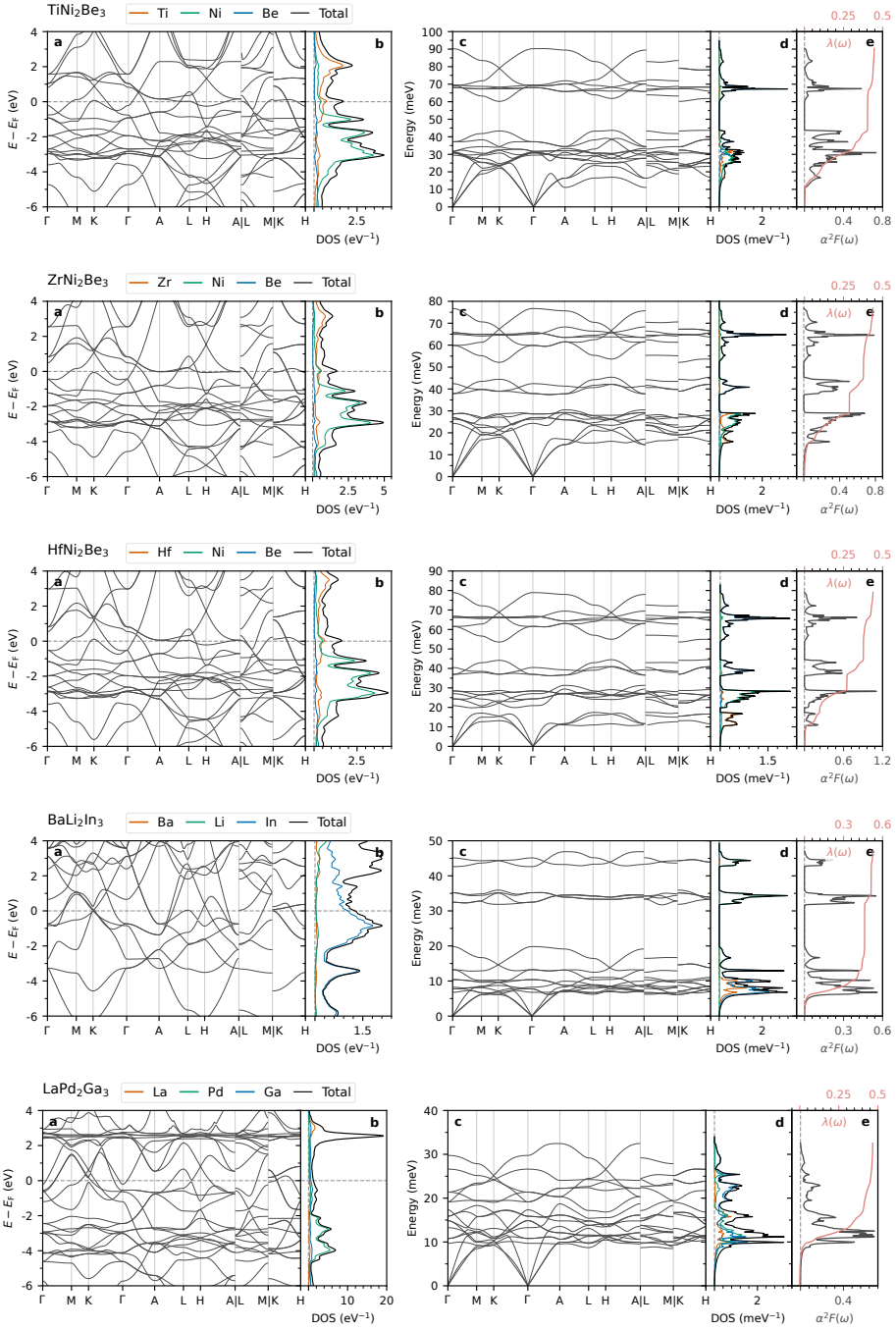

SmNi2Rh3
Sm
Ni
Rh
Total
LaPd2Zn3
La
Pd
Zn
Total
LaPd2Pt3
La
Pd
Pt
Total
PrAg2Zn3
Pr
Ag
Zn
Total
SrAg2Zn3
Sr
Ag
Zn
Total
a
b
c
d
e
E − Ef (eV)
Energy (meV)
Γ M K Γ A L H A|L M|K H
DOS (eV−1)
DOS (meV−1)
λ(ω)
α2F(ω)

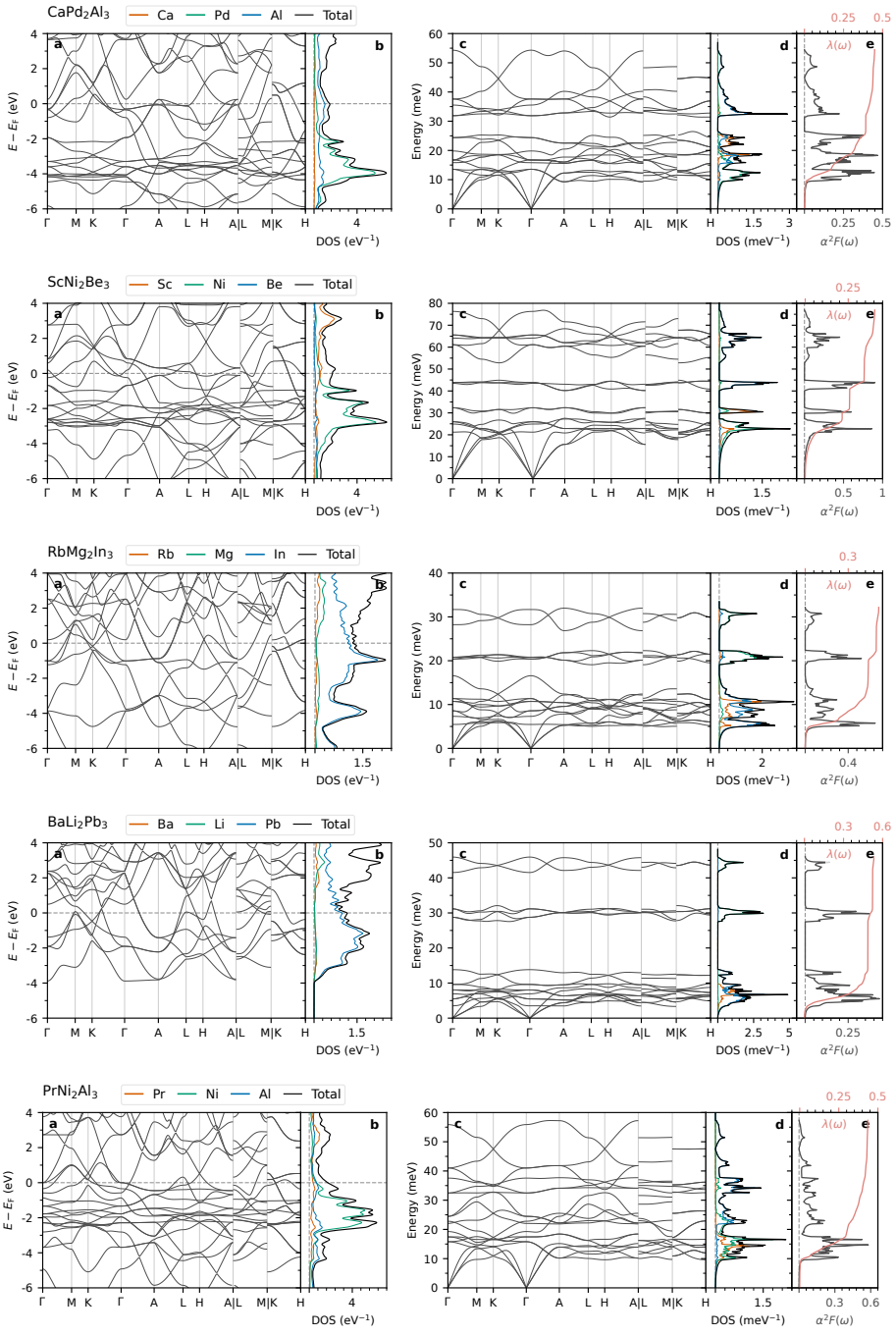
Table S5.2: Predicted compounds with $E_{\text{hull}} < 30\,\text{meV/atom}$ in Type II. Formulas are written in the site order $R\,X_2\,T_3$ and colored by site, R teal, X blue and T red, so the red element is the one carrying the kagome net. The text uses the conventional RT_3X_2 order. $D(E_F)$ is the density of states per spin and per unit cell at the Fermi level. The last column marks a local DOS peak within $E_F \pm 0.5\,\text{eV}$ (Section S5).

Formula	Material ID	E_{hull} (meV/atom)	$\omega_{\log}$ (K)	$D(E_F)$ (eV^{-1})	λ	T_c (K)	FB @ E_F
KLi_2Sb_3	agm071907720	27	102	0.95	0.64	3.0	No
$ErNi_2Be_3$	agm071708349	27	268	1.60	0.48	2.8	Yes
$TmNi_2Be_3$	agm072045138	22	274	1.60	0.47	2.7	Yes
$CsAu_2Bi_3$	agm071689831	27	68	1.24	0.72	2.6	No
$ScCu_2Be_3$	agm071792821	3	365	1.32	0.42	2.0	No
$TiNi_2Be_3$	agm071725295	21	335	1.68	0.42	1.9	Yes
$ZrNi_2Be_3$	agm072043899	0	334	1.66	0.42	1.8	Yes
$HfNi_2Be_3$	agm071827366	0	321	1.59	0.42	1.8	Yes
$BaLi_2In_3$	agm038771285	21	111	1.26	0.51	1.5	No
$LaPd_2Ga_3$	agm003202957	22	149	1.25	0.47	1.4	No
$CaPd_2Al_3$	agm002133833	20	198	1.44	0.44	1.4	No
$ScNi_2Be_3$	agm072095816	0	346	1.71	0.39	1.4	Yes
$RbMg_2In_3$	agm035460572	28	97	1.19	0.50	1.3	No
$BaLi_2Pb_3$	agm005704465	0	81	1.15	0.52	1.2	No
$PrNi_2Al_3$	agm003195351	27	195	1.71	0.42	1.1	Yes
$ZrCu_2Be_3$	agm071593344	16	319	1.06	0.38	1.1	No
$TmPd_2Al_3$	agm002133979	0	174	1.18	0.43	1.1	Yes
$NdNi_2Al_3$	agm003195352	18	195	1.68	0.42	1.1	Yes
$BaLi_2Al_3$	agm071675708	8	221	1.23	0.41	1.1	No
$HfCu_2Be_3$	agm071848908	28	269	0.99	0.39	1.0	No

Figure S5.2: Electronic band, electronic DOS, phononic band, phononic DOS and Eliashberg spectral function of materials listed in Table S5.2.




TiNi2Be3
Ti
Ni
Be
Total
ZrNi2Be3
Zr
Ni
Be
Total
HfNi2Be3
Hf
Ni
Be
Total
BaLi2In3
Ba
Li
In
Total
LaPd2Ga3
La
Pd
Ga
Total
a
b
c
d
e
E − Ef (eV)
DOS (eV−1)
Energy (meV)
DOS (meV−1)
λ(ω)
α2F(ω)
Γ M K Γ A L H A|L M|K H


CaPd2Al3
Ca
Pd
Al
Total
ScNi2Be3
Sc
Ni
Be
Total
RbMg2In3
Rb
Mg
In
Total
BaLi2Pb3
Ba
Li
Pb
Total
PrNi2Al3
Pr
Ni
Al
Total
a
b
c
d
e
E − Ef (eV)
Energy (meV)
Γ M K Γ A L H A|L M|K H
DOS (eV−1)
DOS (meV−1)
α2F(ω)
λ(ω)

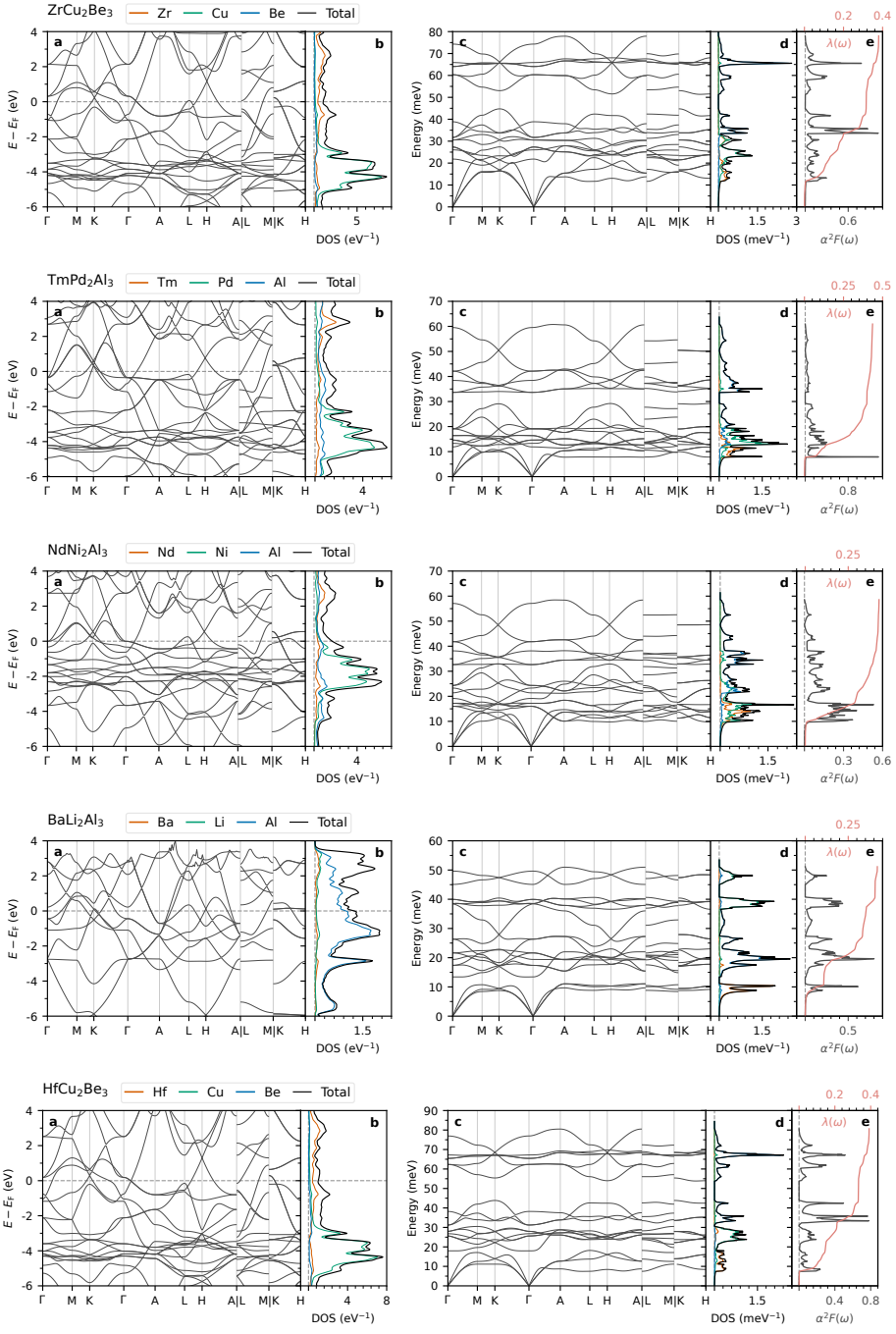

ZrCu2Be3
Zr
Cu
Be
Total
TmPd2Al3
Tm
Pd
Al
Total
NdNi2Al3
Nd
Ni
Al
Total
BaLi2Al3
Ba
Li
Al
Total
HfCu2Be3
Hf
Cu
Be
Total
a
b
c
d
e
E − Ef (eV)
Energy (meV)
DOS (eV−1)
DOS (meV−1)
α2F(ω)
λ(ω)
Γ M K Γ A L H A|L M|K H

Table S5.3: Predicted compounds with $E_{\text{hull}} < 100\,\text{meV/atom}$ in Type I. Formulas are written in the site order $R\,X_2\,T_3$ and colored by site, R teal, X blue and T red, so the red element is the one carrying the kagome net. The text uses the conventional RT_3X_2 order. $D(E_F)$ is the density of states per spin and per unit cell at the Fermi level.

Formula	Material ID	E_{hull} (meV/atom)	$\omega_{\log}$ (K)	$D(E_F)$ (eV^{-1})	λ	T_c (K)
TmB_2Ir_3	agm002137253	0	73	0.98	1.45	9.2
$CaNi_2Ir_3$	agm002203799	59	90	3.07	1.18	8.7
ErB_2Ir_3	agm003202452	0	85	0.98	1.20	8.5
CeB_2Os_3	agm002199385	27	131	1.99	0.89	8.1
$NdAl_2Ir_3$	agm002195286	37	88	1.65	1.13	7.9
$PrAl_2Ir_3$	agm002195389	25	89	1.65	1.11	7.9
$SrNi_2Ir_3$	agm002226323	0	94	3.21	1.02	7.3
LuB_2Rh_3	agm003195416	21	127	1.07	0.85	7.2
$SrCu_2Ir_3$	agm002266899	54	66	2.87	1.29	7.2
$CeAl_2Ir_3$	agm002133322	87	94	1.63	1.01	7.1
$LaGa_2Ir_3$	agm002274867	0	80	1.62	1.10	6.9
TbB_2Ru_3	agm003202167	0	137	1.96	0.81	6.9
YB_2Ru_3	agm003202168	0	165	1.96	0.74	6.8
SmB_2Ir_3	agm002137232	3	112	1.07	0.88	6.8
$PrGa_2Ir_3$	agm002274922	0	90	1.61	1.00	6.7
PmB_2Ru_3	agm071840373	12	162	2.07	0.74	6.7
$PmPd_2Ir_3$	agm032116159	97	90	2.41	0.99	6.6
SmB_2Ru_3	agm003195414	7	157	2.04	0.74	6.5
NdB_2Ru_3	agm003195435	21	166	2.12	0.71	6.3
TmB_2Rh_3	agm002137195	13	144	1.09	0.75	6.2
LaB_2Ru_3	agm003195432	23	166	2.12	0.71	6.2
PrB_2Ru_3	agm003195427	30	171	2.15	0.70	6.2
CeB_2Ru_3	agm003202683	0	178	2.19	0.67	5.9
$NdPd_2Ir_3$	agm002307003	86	99	2.42	0.88	5.9
$CaGa_2Rh_3$	agm002260176	0	117	1.76	0.80	5.8
LaB_2Rh_3	agm003202760	17	180	1.33	0.66	5.7
$RbGe_2Pt_3$	agm034485715	61	81	1.32	0.96	5.6
ErB_2Rh_3	agm003195426	8	152	1.10	0.70	5.5
$PrBe_2Os_3$	agm033617485	93	146	2.40	0.71	5.5
$NdBe_2Os_3$	agm041486382	96	149	2.37	0.70	5.4
$PrPd_2Ir_3$	agm002307010	73	106	2.43	0.80	5.2
HoB_2Rh_3	agm003195417	5	158	1.11	0.67	5.1
LaB_2Ir_3	agm003195415	23	130	1.10	0.72	5.1
$LaPd_2Ir_3$	agm002234136	71	106	2.47	0.79	5.1
DyB_2Rh_3	agm003195430	2	162	1.13	0.66	5.0
$NaGe_2Pt_3$	agm031905555	31	70	1.11	0.96	4.9
TbB_2Rh_3	agm002137193	1	167	1.15	0.64	4.7

Continued on next page

Table S5.3 – continued from previous page

Formula	Material ID	E_{hull} (meV/atom)	$\omega_{\log}$ (K)	$D(E_F)$ (eV^{-1})	λ	T_c (K)
$TbRh_2Cu_3$	agm002267053	83	103	2.56	0.77	4.6
YB_2Rh_3	agm003202164	0	175	1.14	0.62	4.6
$SmAu_2Zn_3$	agm002324461	0	90	1.28	0.80	4.4
$DyRh_2Cu_3$	agm002267047	84	105	2.54	0.74	4.4
$CsMg_2Hg_3$	agm072076899	69	44	1.58	1.20	4.3
$PrRh_2Cu_3$	agm002267051	76	109	2.59	0.72	4.3
$SrAl_2Rh_3$	agm002195511	67	123	1.57	0.69	4.3
$CeRu_2Cu_3$	agm031763759	63	130	2.66	0.67	4.2
$HoRh_2Cu_3$	agm002267049	85	106	2.54	0.73	4.2
$BaGa_2Au_3$	agm002337523	62	70	1.30	0.88	4.2
KGa_2Hg_3	agm071870928	87	61	1.13	0.95	4.1
$PrRu_2Zn_3$	agm002324454	55	127	2.47	0.67	4.1
$NdRu_2Zn_3$	agm002324453	46	127	2.45	0.67	4.0
$BaNi_2Rh_3$	agm002296558	62	141	4.06	0.64	4.0
$TbAu_2Zn_3$	agm002324476	0	90	1.21	0.77	4.0
$TmRh_2Cu_3$	agm002267055	85	106	2.51	0.71	4.0
$SmPt_2Ir_3$	agm002319875	70	116	2.29	0.69	4.0
$LaAu_2Zn_3$	agm002246263	0	103	1.50	0.71	3.9
$PmRu_2Zn_3$	agm071694789	39	126	2.43	0.66	3.9
$SmRu_2Zn_3$	agm002324455	37	125	2.41	0.66	3.9
KGe_2Pt_3	agm038799382	25	93	1.25	0.74	3.8
$CeNi_2Os_3$	agm002296416	87	153	2.78	0.61	3.8
$BaLi_2Zn_3$	agm072080557	59	126	1.72	0.65	3.7
$TmNi_2Ir_3$	agm002227683	34	118	2.50	0.66	3.7
$PmPt_2Ir_3$	agm034807046	59	120	2.29	0.65	3.6
$BaHg_2Au_3$	agm035054481	69	48	1.26	1.00	3.6
YRu_2Zn_3	agm002324493	36	130	2.40	0.63	3.6
$CaCu_2Rh_3$	agm002260829	96	134	3.26	0.62	3.6
$HoLi_2Zn_3$	agm071727858	96	117	1.57	0.65	3.6
YLi_2Zn_3	agm071921673	86	136	1.60	0.62	3.5
$TbRu_2Zn_3$	agm002324456	36	125	2.37	0.64	3.5
$PrNi_2Os_3$	agm002226176	96	159	2.73	0.58	3.4
$DyRu_2Zn_3$	agm002360069	39	125	2.34	0.63	3.4
$DyLi_2Zn_3$	agm071883793	89	122	1.56	0.63	3.3
$LaAl_2Ag_3$	agm002194988	72	96	1.75	0.68	3.3
$NdPt_2Ir_3$	agm002294665	60	124	2.29	0.62	3.3
$ErNi_2Ir_3$	agm002225978	25	127	2.51	0.62	3.2
$BaAl_2Ag_3$	agm002194986	79	91	1.56	0.69	3.2
$HoRu_2Zn_3$	agm002360071	44	125	2.32	0.62	3.2
$NdNi_2Os_3$	agm002226149	90	162	2.69	0.57	3.2
$HoNi_2Ir_3$	agm002226083	18	131	2.51	0.61	3.2
$SmNi_2Os_3$	agm002226251	99	165	2.64	0.56	3.1
$SrGa_2Rh_3$	agm002275043	0	132	1.65	0.60	3.1

Continued on next page

Table S5.3 – continued from previous page

Formula	Material ID	E_{hull} (meV/atom)	$\omega_{\log}$ (K)	$D(E_F)$ (eV^{-1})	λ	T_c (K)
$RbIn_2Hg_3$	agm072085691	58	54	1.26	0.86	3.1
$ErRu_2Zn_3$	agm002360070	48	125	2.30	0.61	3.0
$PrPt_2Ir_3$	agm002308019	56	129	2.30	0.60	3.0
$TbLi_2Zn_3$	agm071791439	82	130	1.55	0.60	3.0
$TmRu_2Zn_3$	agm033727218	52	125	2.28	0.60	2.9
$LaPt_2Ir_3$	agm002218184	38	128	2.38	0.59	2.9
$DyNi_2Ir_3$	agm002225968	12	136	2.51	0.58	2.8
$BaTl_2Ag_3$	agm043468796	86	60	1.48	0.79	2.8
$RbAl_2Ag_3$	agm071885861	99	83	1.08	0.68	2.8
KGa_2Au_3	agm031668111	54	77	0.92	0.70	2.8
$SmPd_2Rh_3$	agm002235382	85	145	2.77	0.56	2.7
$PbGa_2Au_3$	agm039509009	57	51	0.76	0.82	2.7
$TbNi_2Ir_3$	agm002226335	5	140	2.53	0.56	2.7
$PbAl_2Au_3$	agm034909433	73	67	0.83	0.72	2.6
SmV_2Co_3	agm071991445	77	234	2.95	0.49	2.6
$LaIn_2Ag_3$	agm002132859	98	79	1.86	0.68	2.6
$CePt_2Ir_3$	agm002261886	46	131	2.32	0.57	2.6
$BaCu_2Rh_3$	agm002371184	51	132	3.41	0.57	2.6
YNi_2Ir_3	agm002226370	11	143	2.54	0.55	2.6
$SmSi_2Ni_3$	agm002316118	63	172	2.25	0.52	2.6
$PmAu_2Zn_3$	agm031465753	0	110	1.30	0.60	2.6
$PmGa_2Cu_3$	agm033452294	66	123	1.57	0.58	2.5
$PmPd_2Rh_3$	agm041108863	73	149	2.77	0.54	2.5
$PrAu_2Zn_3$	agm002324445	0	114	1.35	0.59	2.5
KHg_2Au_3	agm035388847	73	60	1.16	0.74	2.5
$NaZn_2Au_3$	agm043268940	43	74	1.11	0.68	2.5
$NdLi_2Cd_3$	agm071982672	60	96	1.80	0.62	2.5
$DyPt_2Rh_3$	agm044065542	77	143	2.57	0.54	2.5
$BaAg_2Zn_3$	agm002384834	34	112	1.43	0.59	2.4
KIn_2Au_3	agm040038476	27	54	0.92	0.76	2.3
NdV_2Os_3	agm071889712	85	190	1.93	0.50	2.3
$NdAu_2Zn_3$	agm002324425	0	114	1.32	0.57	2.3
$SrLi_2Zn_3$	agm071926568	35	152	1.61	0.52	2.3
$BaAl_2Zn_3$	agm002327363	75	142	1.13	0.53	2.3
$LaGa_2Cu_3$	agm002267000	84	131	1.67	0.55	2.3
$SmLi_2Zn_3$	agm071929341	59	141	1.52	0.53	2.3
PrV_2Os_3	agm072092776	76	191	1.93	0.49	2.2
$TbPt_2Rh_3$	agm039629032	64	147	2.57	0.52	2.2
$BaIn_2Ag_3$	agm002247479	47	74	1.59	0.64	2.1
$BaGa_2Ag_3$	agm002274762	47	106	1.59	0.57	2.1
$PrMg_2Zn_3$	agm039915784	73	98	1.35	0.58	2.1
$BaLi_2Cd_3$	agm071678116	16	103	1.90	0.57	2.1
$SmCu_2Ir_3$	agm002266833	80	124	2.42	0.54	2.1

Continued on next page

Table S5.3 – continued from previous page

Formula	Material ID	E_{hull} (meV/atom)	$\omega_{\log}$ (K)	$D(E_F)$ (eV^{-1})	λ	T_c (K)
$SmNi_2Ir_3$	agm002226250	0	149	2.56	0.52	2.1
TbV_2Co_3	agm071683364	61	239	2.90	0.46	2.1
$CaLi_2Zn_3$	agm071598618	37	158	1.56	0.51	2.1
$NdLi_2Zn_3$	agm072072237	46	147	1.49	0.51	2.0
$NdPd_2Rh_3$	agm002235380	65	156	2.78	0.51	2.0
$DyBe_2Zn_3$	agm030890617	97	165	0.93	0.50	2.0
KAl_2Zn_3	agm071765022	82	147	0.93	0.51	2.0
$PrLi_2Zn_3$	agm071732143	39	148	1.48	0.51	2.0
$LaLi_2Zn_3$	agm071648186	42	149	1.62	0.51	2.0
$PmNi_2Ir_3$	agm005853112	0	151	2.57	0.50	2.0
HoV_2Co_3	agm071696855	69	241	2.86	0.45	1.9
$PrPd_2Rh_3$	agm002235381	53	159	2.79	0.50	1.9
$CaGa_2Zn_3$	agm002331397	89	140	0.93	0.51	1.9
TmV_2Co_3	agm071696573	81	240	2.83	0.45	1.9
$BaGa_2Cu_3$	agm002371224	89	130	1.53	0.52	1.9
ErV_2Co_3	agm071982099	73	241	2.84	0.45	1.9
$LaPd_2Rh_3$	agm002180591	55	155	2.84	0.50	1.9
$CaLi_2Cd_3$	agm072084042	58	96	1.62	0.57	1.9
$LaNi_2Ir_3$	agm002167274	0	152	2.68	0.50	1.8
$BaGa_2Cd_3$	agm071730727	89	110	1.27	0.54	1.8
$SrGe_2Ni_3$	agm002295246	71	149	1.93	0.49	1.8
$RbTl_2Pt_3$	agm034136002	94	61	1.20	0.64	1.8
$NdMg_2Zn_3$	agm033357793	79	98	1.32	0.55	1.7
$NdCu_2Ir_3$	agm002268171	61	133	2.40	0.51	1.7
$LaLi_2Cd_3$	agm071989287	47	104	1.93	0.54	1.7
$DyNi_2Rh_3$	agm002167305	23	143	2.99	0.50	1.7
$NaAl_2Zn_3$	agm071985931	50	138	0.81	0.50	1.7
$LaHg_2Ag_3$	agm071674034	84	59	1.68	0.64	1.7
YV_2Co_3	agm072080688	60	252	2.88	0.44	1.7
$TbAg_2Zn_3$	agm002360031	14	108	1.28	0.53	1.7
$PrNi_2Ir_3$	agm002226175	0	157	2.60	0.48	1.7
$SrLi_2Cd_3$	agm071725069	23	102	1.71	0.54	1.7
$BaAg_2Hg_3$	agm034076976	70	62	1.41	0.62	1.6
$SrAu_2Zn_3$	agm002324467	18	121	1.25	0.51	1.6
$TbNi_2Rh_3$	agm002167312	17	150	3.01	0.48	1.6
$SmPt_2Rh_3$	agm002235389	39	157	2.59	0.48	1.6
NaB_2Ir_3	agm005806208	2	185	1.12	0.46	1.6
$LaAg_2Zn_3$	agm002324396	0	118	1.43	0.51	1.6
$PrCu_2Ir_3$	agm002268180	49	135	2.40	0.49	1.5
KAg_2Zn_3	agm039598974	40	108	1.09	0.52	1.5
$RbZn_2Au_3$	agm041423042	61	76	0.98	0.57	1.5
$PmPt_2Rh_3$	agm031020160	28	159	2.59	0.47	1.5
$CeNi_2Ir_3$	agm002227628	0	160	2.64	0.46	1.4

Continued on next page

Table S5.3 – continued from previous page

Formula	Material ID	E_{hull} (meV/atom)	$\omega_{\log}$ (K)	$D(E_F)$ (eV^{-1})	λ	T_c (K)
$CeBe_2Co_3$	agm038805054	28	201	3.34	0.44	1.4
$NdPt_2Rh_3$	agm002235378	32	161	2.60	0.46	1.4
$BaCu_2Zn_3$	agm002334916	55	135	1.49	0.48	1.4
$NaAu_2Zn_3$	agm039946149	14	114	1.04	0.50	1.4
$CsAu_2Hg_3$	agm071934027	33	54	0.90	0.61	1.4
$TbSi_2Ni_3$	agm002316120	55	195	2.09	0.44	1.3
$PrPt_2Rh_3$	agm002235386	28	165	2.62	0.45	1.3
$NaGe_2Cu_3$	agm032410195	76	161	0.98	0.45	1.3
$SrAl_2Ag_3$	agm002133724	42	126	1.38	0.48	1.3
$LaPt_2Rh_3$	agm002180579	22	160	2.69	0.45	1.3
$BaPd_2Zn_3$	agm002360061	28	117	1.46	0.49	1.3
$LaMg_2Zn_3$	agm002286631	57	111	1.38	0.49	1.3
KZn_2Cd_3	agm032429899	68	102	1.21	0.50	1.3
$SrAl_2Zn_3$	agm002248477	78	160	0.98	0.45	1.3
$SrGa_2Zn_3$	agm002360053	95	149	0.98	0.46	1.3
$BaGa_2Rh_3$	agm002337544	0	135	1.53	0.47	1.3
$SrGa_2Cu_3$	agm002267004	49	144	1.44	0.46	1.3
$SmAg_2Zn_3$	agm002360030	2	120	1.30	0.48	1.2
$BaLi_2Ag_3$	agm071772019	42	69	1.49	0.55	1.2
KZn_2Au_3	agm032323358	42	86	1.07	0.51	1.2
$SrGa_2Ag_3$	agm002213111	32	115	1.37	0.48	1.2
KAu_2Hg_3	agm072065774	57	59	0.87	0.57	1.2
$SmNi_2Rh_3$	agm002167311	1	167	3.04	0.44	1.2
$DySi_2Ni_3$	agm002316112	53	199	2.05	0.42	1.1
$RbAu_2Hg_3$	agm071959257	39	58	0.86	0.57	1.1
$CePt_2Rh_3$	agm033056941	55	166	2.64	0.44	1.1
$LaCu_2Ir_3$	agm002207746	35	138	2.32	0.45	1.1
$BaSb_2Rh_3$	agm071960227	46	126	1.44	0.46	1.1
$LaPd_2Zn_3$	agm002246275	0	145	1.73	0.45	1.1
$RbCd_2Au_3$	agm039823197	45	66	1.07	0.54	1.1
$SrZn_2Au_3$	agm002324322	50	83	1.21	0.51	1.1
TmV_2Ru_3	agm071671242	96	223	1.72	0.41	1.1
LaV_2Ru_3	agm071966397	41	206	1.77	0.41	1.0
$PmZn_2Ag_3$	agm072053067	47	101	1.61	0.48	1.0
$LaPd_2Pt_3$	agm002234138	0	103	2.04	0.47	1.0
$PrAg_2Zn_3$	agm002360029	0	126	1.31	0.45	1.0
$SrAg_2Zn_3$	agm002360072	0	124	1.33	0.45	1.0

Table S5.4: Predicted compounds with $E_{\text{hull}} < 100\,\text{meV/atom}$ in Type II. Formulas are written in the site order $R\,X_2\,T_3$ and colored by site, R teal, X blue and T red, so the red element is the one carrying the kagome net. The text uses the conventional RT_3X_2 order. $D(E_F)$ is the density of states per spin and per unit cell at the Fermi level.

Formula	Material ID	E_{hull} (meV/atom)	$\omega_{\log}$ (K)	$D(E_F)$ (eV^{-1})	λ	T_c (K)
$ZrPd_2Be_3$	agm071721414	60	189	1.60	1.04	15.0
$HfPd_2Be_3$	agm071647583	71	202	1.49	0.89	12.3
$HfPt_2Be_3$	agm071755690	49	202	1.17	0.88	12.0
$TiPt_2Be_3$	agm071816678	73	193	1.32	0.89	11.8
$ZrPt_2Be_3$	agm072017833	34	215	1.24	0.81	10.9
$LaSi_2Al_3$	agm002134055	86	160	1.45	0.87	9.4
$LaRh_2Ga_3$	agm002151213	65	120	1.99	0.93	7.9
$LaPt_2Ga_3$	agm002151180	87	100	1.38	1.04	7.9
$BaPd_2Al_3$	agm002248752	96	118	1.82	0.93	7.8
$TbPd_2Be_3$	agm071773951	85	216	1.51	0.69	7.6
$TmPd_2Be_3$	agm071781809	78	229	1.50	0.68	7.6
$HoPd_2Be_3$	agm071784762	80	223	1.51	0.68	7.5
$ErPd_2Be_3$	agm071892668	79	228	1.50	0.67	7.4
$LaRh_2Al_3$	agm002134004	58	145	2.04	0.81	7.3
$CsGa_2Bi_3$	agm071652597	78	60	1.42	1.39	7.1
$CeRh_2Ga_3$	agm002151212	54	125	1.86	0.86	7.1
$ScPd_2Be_3$	agm072096804	61	257	1.62	0.63	7.0
$BaPd_2Ga_3$	agm002213204	79	114	1.67	0.88	6.8
$PrRh_2Al_3$	agm002195978	43	148	1.90	0.77	6.7
$PrRh_2Ga_3$	agm002213223	63	131	1.84	0.78	6.1
$LaPt_2Al_3$	agm002133904	68	137	1.54	0.75	5.9
$NdRh_2Al_3$	agm002248776	45	159	1.87	0.68	5.4
$CaIr_2Al_3$	agm005704535	99	89	1.68	0.86	5.1
$PrPt_2Al_3$	agm002195965	56	149	1.39	0.67	4.7
$TmRu_2Al_3$	agm033899183	97	158	2.65	0.65	4.7
$LaIr_2Al_3$	agm002133903	88	141	1.71	0.68	4.7
$LuPt_2Al_3$	agm002195858	78	139	1.12	0.68	4.7
$TmPt_2Al_3$	agm002196091	70	142	1.15	0.67	4.6
$NdPt_2Al_3$	agm002248749	54	150	1.35	0.65	4.5
$ErPt_2Al_3$	agm002195729	65	143	1.16	0.66	4.5
$DyPt_2Al_3$	agm002195723	61	146	1.19	0.65	4.4
$TbPt_2Al_3$	agm002196075	59	148	1.21	0.65	4.4
$PmRh_2Al_3$	agm032802255	46	167	1.84	0.62	4.4
$HoPt_2Al_3$	agm002195840	64	145	1.18	0.65	4.4
$SmPt_2Al_3$	agm002248953	55	151	1.29	0.64	4.3
$PmPt_2Al_3$	agm038766191	37	151	1.32	0.64	4.3
$PmCu_2Be_3$	agm071902574	86	303	1.45	0.52	4.3

Continued on next page

Table S5.4 – continued from previous page

Formula	Material ID	E_{hull} (meV/atom)	$\omega_{\log}$ (K)	$D(E_F)$ (eV^{-1})	λ	T_c (K)
$TmCu_2Be_3$	agm071590064	47	303	1.37	0.52	4.3
$HoCu_2Be_3$	agm071706171	53	308	1.41	0.51	4.3
$DyCu_2Be_3$	agm071966243	56	305	1.43	0.51	4.3
$CsGa_2In_3$	agm071615201	75	96	1.37	0.76	4.2
$ErCu_2Be_3$	agm072008289	50	305	1.40	0.51	4.2
$SmCu_2Be_3$	agm071702232	79	304	1.45	0.51	4.1
KLi_2Tl_3	agm071807539	74	68	1.69	0.88	4.1
YPt_2Al_3	agm002196108	57	156	1.20	0.62	4.1
$TiCu_2Be_3$	agm071800885	64	163	1.18	0.61	4.1
$SrRh_2Ga_3$	agm002275198	85	147	1.84	0.63	4.0
$SmRh_2Al_3$	agm002248777	48	173	1.82	0.59	3.9
$RbTl_2Pb_3$	agm071712400	45	55	1.61	0.98	3.9
$LaGa_2Al_3$	agm002327397	92	133	1.37	0.64	3.8
KTl_2Pb_3	agm071986780	61	54	1.55	0.97	3.8
$CsHg_2Tl_3$	agm033730936	56	49	1.60	1.03	3.8
YCu_2Be_3	agm071894160	56	331	1.47	0.49	3.8
$SrPd_2Ga_3$	agm002151226	52	135	1.49	0.64	3.7
$BaLi_2Ga_3$	agm071816344	31	147	1.21	0.61	3.7
$BaHg_2Al_3$	agm031653555	89	133	1.23	0.63	3.6
$SrLi_2Tl_3$	agm072059304	45	57	1.37	0.90	3.5
$RbHg_2Pb_3$	agm071980026	56	54	1.38	0.92	3.5
$RbLi_2Sb_3$	agm071828172	30	93	0.98	0.71	3.5
KHg_2In_3	agm003420560	47	67	1.27	0.82	3.4
$PrIr_2Al_3$	agm002195964	73	158	1.59	0.58	3.4
$TbNi_2Be_3$	agm071909953	43	257	1.63	0.51	3.4
$LaCo_2Ga_3$	agm002143780	69	153	2.91	0.59	3.4
$CsAu_2In_3$	agm071742875	67	76	1.55	0.76	3.4
$LaCo_2Al_3$	agm002133847	97	171	2.93	0.56	3.3
$NaLi_2Sb_3$	agm071795043	74	99	0.90	0.68	3.3
$CsHg_2In_3$	agm003420557	45	71	1.37	0.77	3.3
$DyNi_2Be_3$	agm071796331	36	261	1.62	0.50	3.3
$SmRu_2Al_3$	agm031813136	65	170	2.51	0.56	3.2
$LaRu_2Ga_3$	agm032677294	67	142	2.40	0.59	3.2
$RbAu_2In_3$	agm071921243	67	75	1.42	0.75	3.2
$RbGa_2Pb_3$	agm071627791	93	74	1.37	0.74	3.1
$SnTa_2Ga_3$	agm071785002	88	138	1.34	0.59	3.1
$HoNi_2Be_3$	agm072053668	31	263	1.61	0.49	3.1
$NdIr_2Al_3$	agm002251375	69	160	1.59	0.56	3.0
KLi_2Sb_3	agm071907720	27	102	0.95	0.64	3.0
YNi_2Be_3	agm071893162	34	280	1.65	0.48	2.9
$BaAu_2Sn_3$	agm003411324	97	73	1.23	0.73	2.9
$TmPt_2Be_3$	agm071624759	78	221	1.16	0.51	2.9
$LaRu_2Al_3$	agm041897259	91	169	2.41	0.54	2.9

Continued on next page

Table S5.4 – continued from previous page

Formula	Material ID	E_{hull} (meV/atom)	$\omega_{\log}$ (K)	$D(E_F)$ (eV^{-1})	λ	T_c (K)
$SmRu_2Ga_3$	agm002275193	65	148	2.46	0.57	2.9
$SrPd_2Al_3$	agm002134079	32	174	1.62	0.54	2.9
$TbPt_2Be_3$	agm071683421	87	213	1.13	0.51	2.9
$ErNi_2Be_3$	agm071708349	27	268	1.60	0.48	2.8
$PrRu_2Al_3$	agm031668506	64	173	2.43	0.54	2.8
$BaLi_2Tl_3$	agm072080483	30	75	1.45	0.71	2.8
$CsAg_2In_3$	agm072020533	85	78	1.50	0.70	2.8
$DyPt_2Be_3$	agm071800260	84	217	1.13	0.50	2.8
$ErPt_2Be_3$	agm071999384	80	220	1.15	0.50	2.7
$SrNi_2Ga_3$	agm002294810	85	153	1.90	0.55	2.7
$PmIr_2Al_3$	agm033291134	55	161	1.58	0.54	2.7
$TmNi_2Be_3$	agm072045138	22	274	1.60	0.47	2.7
$CsAu_2Bi_3$	agm071689831	27	68	1.24	0.72	2.6
$PmZn_2Al_3$	agm003420545	88	137	1.25	0.56	2.5
$SmIr_2Al_3$	agm043463842	67	161	1.58	0.53	2.5
$AlNi_2Be_3$	agm071967410	79	242	1.12	0.48	2.5
$NaPd_2Ga_3$	agm071700982	65	135	1.16	0.56	2.5
$TbRh_2Al_3$	agm002195979	53	185	1.76	0.51	2.4
$PrRu_2Ga_3$	agm002275191	59	153	2.39	0.53	2.4
$NdRu_2Ga_3$	agm002275190	53	153	2.41	0.53	2.4
$BaCd_2Al_3$	agm043790175	94	163	1.23	0.52	2.4
$SrLi_2Ga_3$	agm071848698	41	163	1.10	0.52	2.3
KLi_2Pb_3	agm071988679	81	80	1.25	0.64	2.3
$CaZn_2Al_3$	agm003420537	59	177	1.22	0.50	2.3
$NaAg_2Al_3$	agm005806252	46	166	1.04	0.51	2.2
$CaRh_2Ga_3$	agm002260183	44	163	1.77	0.51	2.2
$CaRh_2Al_3$	agm042201279	71	180	1.71	0.50	2.2
$PrCo_2Al_3$	agm002195637	82	187	2.81	0.49	2.2
$NdZn_2Al_3$	agm003420540	84	150	1.24	0.52	2.2
$DyRh_2Al_3$	agm002195973	55	186	1.73	0.49	2.2
$DyIr_2Al_3$	agm002195722	78	158	1.59	0.51	2.1
$TbIr_2Al_3$	agm002196074	76	159	1.59	0.51	2.1
$HoIr_2Al_3$	agm002195839	81	158	1.59	0.51	2.1
$SrLi_2Pb_3$	agm005853412	34	65	1.09	0.66	2.1
KLi_2In_3	agm071928819	91	115	1.46	0.55	2.0
$HoRh_2Al_3$	agm002195976	57	188	1.71	0.48	2.0
$CaRu_2Ga_3$	agm041449476	32	161	2.37	0.50	2.0
$ScCu_2Be_3$	agm071792821	3	365	1.32	0.42	2.0
$LuAu_2Al_3$	agm002195856	94	102	0.85	0.56	2.0
$TiNi_2Be_3$	agm071725295	21	335	1.68	0.42	1.9
$ErIr_2Al_3$	agm002195728	84	157	1.59	0.50	1.9
$LuIr_2Al_3$	agm002195857	84	152	1.57	0.50	1.9
$LaNi_2Al_3$	agm002133938	36	181	1.82	0.48	1.9

Continued on next page

Table S5.4 – continued from previous page

Formula	Material ID	E_{hull} (meV/atom)	$\omega_{\log}$ (K)	$D(E_F)$ (eV^{-1})	λ	T_c (K)
$PrZn_2Al_3$	agm003420542	80	160	1.24	0.49	1.9
YIr_2Al_3	agm002196107	71	165	1.59	0.49	1.9
$TmIr_2Al_3$	agm002196090	88	156	1.59	0.50	1.9
$ZrNi_2Be_3$	agm072043899	0	334	1.66	0.42	1.8
$PrCo_2Ga_3$	agm002205430	58	173	2.78	0.48	1.8
$HfNi_2Be_3$	agm071827366	0	321	1.59	0.42	1.8
$BaMg_2Al_3$	agm043575535	48	195	1.31	0.47	1.8
YRh_2Al_3	agm002196109	47	200	1.75	0.46	1.7
KZn_2Al_3	agm034193883	59	191	0.97	0.46	1.7
$CaAu_2Al_3$	agm032393163	45	159	0.91	0.48	1.6
$ErRh_2Al_3$	agm002195974	59	189	1.69	0.46	1.6
$TmRh_2Al_3$	agm002195981	62	188	1.67	0.46	1.6
$TmTc_2Al_3$	agm071773881	83	167	2.15	0.47	1.6
$ErTc_2Al_3$	agm072023859	81	168	2.15	0.46	1.5
$ZrNi_2Al_3$	agm003199116	62	162	1.23	0.47	1.5
$InTa_2Ga_3$	agm071596010	64	166	1.33	0.46	1.5
$HoTc_2Al_3$	agm071792469	80	169	2.16	0.46	1.5
$SrMg_2Al_3$	agm034675852	54	200	1.26	0.45	1.5
$BaLi_2In_3$	agm038771285	21	111	1.26	0.51	1.5
$RbLi_2Sn_3$	agm072039152	97	123	1.18	0.50	1.5
$TbCo_2Al_3$	agm002195638	58	191	2.76	0.45	1.5
$HfNi_2Al_3$	agm033574488	69	145	1.14	0.48	1.5
$LaPd_2Ga_3$	agm003202957	22	149	1.25	0.47	1.4
$SrZn_2Al_3$	agm002248994	40	196	1.20	0.44	1.4
$TmAu_2Al_3$	agm002196089	75	115	0.83	0.50	1.4
$CsMg_2Tl_3$	agm039487723	38	73	1.40	0.56	1.4
$CsMg_2In_3$	agm034268822	41	99	1.26	0.51	1.4
$CaPd_2Al_3$	agm002133833	20	198	1.44	0.44	1.4
$ScNi_2Be_3$	agm072095816	0	346	1.71	0.39	1.4
YTc_2Al_3	agm071966873	78	184	2.20	0.44	1.4
$PmCo_2Ga_3$	agm034920347	46	177	2.78	0.44	1.3
$DyCo_2Al_3$	agm002195633	61	193	2.74	0.44	1.3
$LaAg_2Ga_3$	agm041761825	59	114	1.02	0.49	1.3
$SmTc_2Al_3$	agm071655756	93	176	2.18	0.44	1.3
$PmTc_2Al_3$	agm071704127	95	179	2.18	0.44	1.3
$RbMg_2In_3$	agm035460572	28	97	1.19	0.50	1.3
KZn_2In_3	agm039657883	92	106	1.10	0.49	1.2
$LuRh_2Al_3$	agm002195977	58	189	1.62	0.43	1.2
$InNb_2Ga_3$	agm071672771	88	206	1.40	0.43	1.2
$NbNi_2Be_3$	agm071623885	44	317	1.32	0.39	1.2
$BaCu_2Ga_3$	agm002266652	60	151	1.11	0.45	1.2
$HoCo_2Al_3$	agm002195635	64	192	2.72	0.43	1.2
$SrLi_2In_3$	agm034085442	41	110	1.16	0.48	1.2

Continued on next page

Table S5.4 – continued from previous page

Formula	Material ID	E_{hull} (meV/atom)	$\omega_{\log}$ (K)	$D(E_F)$ (eV^{-1})	λ	T_c (K)
$BaLi_2Pb_3$	agm005704465	0	81	1.15	0.52	1.2
$BaAu_2In_3$	agm033628198	59	86	1.15	0.51	1.2
$ErAu_2Al_3$	agm002195727	67	121	0.83	0.47	1.2
$PrNi_2Al_3$	agm003195351	27	195	1.71	0.42	1.1
$ErCo_2Al_3$	agm002195634	67	192	2.69	0.42	1.1
$LaZn_2Al_3$	agm002196113	49	175	1.30	0.43	1.1
$ZrCu_2Be_3$	agm071593344	16	319	1.06	0.38	1.1
$TmPd_2Al_3$	agm002133979	0	174	1.18	0.43	1.1
$PmLi_2Ga_3$	agm071788452	97	148	1.01	0.44	1.1
$PrAg_2Ga_3$	agm034145266	74	119	0.94	0.46	1.1
$NdNi_2Al_3$	agm003195352	18	195	1.68	0.42	1.1
$BaLi_2Al_3$	agm071675708	8	221	1.23	0.41	1.1
$HfCu_2Be_3$	agm071848908	28	269	0.99	0.39	1.0
$TmCo_2Al_3$	agm002195640	70	191	2.66	0.42	1.0
$RbLi_2Bi_3$	agm071755728	47	94	1.01	0.48	1.0
YCo_2Al_3	agm002195641	61	209	2.76	0.41	1.0

References

[1] Blöchl, P. E. Projector augmented-wave method. *Phys. Rev. B* **50**, 17953–17979 (1994).

[2] Kresse, G. & Joubert, D. From ultrasoft pseudopotentials to the projector augmented-wave method. *Phys. Rev. B* **59**, 1758–1775 (1999).

[3] Kresse, G. & Furthmüller, J. Efficiency of ab-initio total energy calculations for metals and semiconductors using a plane-wave basis set. *Computational Materials Science* **6**, 15–50 (1996).

[4] Kresse, G. & Furthmüuller, J. Efficient iterative schemes for ab initio total-energy calculations using a plane-wave basis set. *Phys. Rev. B* **54**, 11169–11186 (1996).

[5] Giannozzi, P. *et al.* Quantum ESPRESSO: a modular and open-source software project for quantum simulations of materials. *Journal of Physics: Condensed Matter* **21**, 395502 (2009).

[6] Giannozzi, P. *et al.* Advanced capabilities for materials modelling with quantum ESPRESSO. *Journal of Physics: Condensed Matter* **29**, 465901 (2017).

[7] Perdew, J. P., Burke, K. & Ernzerhof, M. Generalized gradient approximation made simple. *Phys. Rev. Lett.* **77**, 3865–3868 (1996).

[8] Monkhorst, H. J. & Pack, J. D. Special points for Brillouin-zone integrations. *Phys. Rev. B* **13**, 5188–5192 (1976).

[9] Gao, J., Wu, Q., Persson, C. & Wang, Z. Irvsp : To obtain irreducible representations of electronic states in the VASP. *Computer Physics Communications* **261**, 107760 (2021).

[10] Zhang, R. *et al.* Large shift current, π Zak phase, and the unconventional nature of Se and Te. *Phys. Rev. Res.* **5**, 023142 (2023).

[11] Wu, Q., Zhang, S., Song, H.-F., Troyer, M. & Soluyanov, A. A. WannierTools : An open-source software package for novel topological materials. *Computer Physics Communications* **224**, 405 – 416 (2018).

[12] Mostofi, A. A. *et al.* Wannier90 : A tool for obtaining maximally-localised Wannier functions. *Computer Physics Communications* **178**, 685 – 699 (2008).

[13] Pizzi, G. *et al.* Wannier90 as a community code: new features and applications. *Journal of Physics: Condensed Matter* **32**, 165902 (2020).

[14] Togo, A., Chaput, L., Tadano, T. & Tanaka, I. Implementation strategies in phonopy and phono3py. *Journal of Physics: Condensed Matter* **35**, 353001 (2023).

[15] Togo, A. First-principles phonon calculations with Phonopy and Phono3py. *Journal of the Physical Society of Japan* **92**, 012001 (2023).

[16] Giustino, F., Cohen, M. L. & Louie, S. G. Electron-phonon interaction using Wannier functions. *Phys. Rev. B* **76**, 165108 (2007).

[17] Noffsinger, J. *et al.* EPW: A program for calculating the electron–phonon coupling using maximally localized Wannier functions. *Computer Physics Communications* **181**, 2140–2148 (2010).

[18] Poncé, S., Margine, E. R., Verdi, C. & Giustino, F. EPW: Electron-phonon coupling, transport and superconducting properties using maximally localized Wannier functions. *Computer Physics Communications* **209**, 116–133 (2016). ArXiv:1604.03525 [cond-mat].

[19] Lee, H. *et al.* Electron-phonon physics from first principles using the EPW code. *npj Computational Materials* **9**, 156 (2023).

[20] Blaha, P. *et al.* WIEN2k: An APW+lo program for calculating the properties of solids. *The Journal of Chemical Physics* **152**, 074101 (2020).

[21] Haule, K., Yee, C.-H. & Kim, K. Dynamical mean-field theory within the full-potential methods: Electronic structure of $CeIrIn_5$, $CeCoIn_5$, and $CeRhIn_5$. *Phys. Rev. B* **81**, 195107 (2010).

[22] Perdew, J. P. & Wang, Y. Accurate and simple analytic representation of the electron-gas correlation energy. *Phys. Rev. B* **45**, 13244–13249 (1992).

[23] Haule, K. & Birol, T. Free energy from stationary implementation of the DFT + DMFT functional. *Phys. Rev. Lett.* **115**, 256402 (2015).

[24] Haule, K. & Pascut, G. L. Forces for structural optimizations in correlated materials within a DFT+embedded DMFT functional approach. *Phys. Rev. B* **94**, 195146 (2016).

[25] Haule, K. Quantum Monte Carlo impurity solver for cluster dynamical mean-field theory and electronic structure calculations with adjustable cluster base. *Phys. Rev. B* **75**, 155113 (2007).

[26] Schmidt, J., Pettersson, L., Verdozzi, C., Botti, S. & Marques, M. A. L. Crystal graph attention networks for the prediction of stable materials. *Science Advances* **7**, eabi7948 (2021).

[27] Schmidt, J. *et al.* Improving machine-learning models in materials science through large datasets. *Mater. Today Phys.* **48**, 101560 (2024).

[28] Perdew, J. P. *et al.* Restoring the density-gradient expansion for exchange in solids and surfaces. *Phys. Rev. Lett.* **100**, 136406 (2008).

[29] van Setten, M. *et al.* The PseudoDojo: Training and grading a 85 element optimized norm-conserving pseudopotential table. *Computer Physics Communications* **226**, 39–54 (2018).

[30] Methfessel, M. & Paxton, A. T. High-precision sampling for Brillouin-zone integration in metals. *Phys. Rev. B* **40**, 3616–3621 (1989).

[31] McMillan, W. L. Transition temperature of strong-coupled superconductors. *Phys. Rev.* **167**, 331–344 (1968).

[32] Dynes, R. McMillan's equation and the Tc of superconductors. *Solid State Communications* **10**, 615–618 (1972).

[33] Jiang, Y. *et al.* FeGe as a building block for the kagome 1:1, 1:6:6, and 1:3:5 families: Hidden *d*-orbital decoupling of flat band sectors, effective models, and interaction Hamiltonians. *Phys. Rev. B* **111**, 125163 (2025).

[34] Deng, J., Zhang, R., Xie, Y., Wu, X. & Wang, Z. Two elementary band representation model, Fermi surface nesting, and surface topological superconductivity in AV_3Sb_5 (A = K, Rb, Cs). *Phys. Rev. B* **108**, 115123 (2023).

[35] Ku, H., Meisner, G., Acker, F. & Johnston, D. Superconducting and magnetic properties of new ternary borides with the $CeCo_3B_2$-type structure. *Solid State Communications* **35**, 91–96 (1980).

[36] Kishimoto, Y. *et al.* Magnetic susceptibility study of $LaRu_3Si_2$. *Journal of the Physical Society of Japan* **71**, 2035–2038 (2002).

[37] Li, S. *et al.* Anomalous properties in the normal and superconducting states of $LaRu_3Si_2$. *Phys. Rev. B* **84**, 214527 (2011).

[38] Mielke, C. *et al.* Nodeless kagome superconductivity in $LaRu_3Si_2$. *Phys. Rev. Mater.* **5**, 034803 (2021).

[39] Mielke, C. *et al.* Microscopic study of the impurity effect in the kagome superconductor $La(Ru_{1-x}Fe_x)_3Si_2$. *Phys. Rev. B* **109**, 134501 (2024).

[40] Ushioda, T. & Muranaka, T. Two-gap superconducting states of $LaRu_3Si_2$. *Physica C: Superconductivity and its Applications* **625**, 1354583 (2024).

[41] Plokhikh, I. *et al.* Discovery of charge order above room-temperature in the prototypical kagome superconductor $La(Ru_{1-x}Fe_x)_3Si_2$. *Communications Physics* **7**, 182 (2024).

[42] Mielke III, C. *et al.* Coexisting multiple charge orders and magnetism in the kagome superconductor $LaRu_3Si_2$. *Advanced Materials* **37**, 2503065 (2025).

[43] Aroyo, M. I. *et al.* Bilbao crystallographic server: I. databases and crystallographic computing programs. *Zeitschrift für Kristallographie - Crystalline Materials* **221**, 15–27 (2006).

[44] Aroyo, M. I., Kirov, A., Capillas, C., Perez-Mato, J. M. & Wondratschek, H. Bilbao crystallographic server. II. Representations of crystallographic point groups and space groups. *Acta Crystallographica Section A* **62**, 115–128 (2006).

[45] Weber, F. *et al.* Extended phonon collapse and the origin of the charge-density wave in $2H-NbSe_2$. *Phys. Rev. Lett.* **107**, 107403 (2011).

[46] Weber, F. *et al.* Optical phonons and the soft mode in $2H$-$NbSe_2$. *Phys. Rev. B* **87**, 245111 (2013).

[47] Mialitsin, A., Dennis, B. S., Zhigadlo, N. D., Karpinski, J. & Blumberg, G. Anharmonicity and self-energy effects of the E_{2g} phonon in MgB_2. *Phys. Rev. B* **75**, 020509 (2007).

[48] Ponosov, Y. S. & Streltsov, S. V. Raman-active E_{2g} phonon in MgB_2: Electron-phonon interaction and anharmonicity. *Phys. Rev. B* **96**, 214503 (2017).

[49] Wang, Y. *et al.* Soft phonon charge-density-wave formation in the kagome metal KV_3Sb_5. *Phys. Rev. Lett.* **136**, 136401 (2026).

[50] Barz, H. New ternary superconductors with silicon. *Materials Research Bulletin* **15**, 1489–1491 (1980).

[51] Li, Z. *et al.* Superconducting dome and structural changes in $LaRu_3Si_2$ under pressure. *Phys. Rev. B* **111**, 144505 (2025).

[52] Ma, K. *et al.* Correlation between the dome-shaped superconducting phase diagram, charge order, and normal-state electronic properties in $LaRu_3Si_2$. *Nature Communications* **16**, 6149 (2025).

[53] Bradlyn, B. *et al.* Topological quantum chemistry. *Nature* **547**, 298–305 (2017).

[54] Cano, J. *et al.* Building blocks of topological quantum chemistry: Elementary band representations. *Phys. Rev. B* **97**, 035139 (2018).

[55] Elcoro, L. *et al.* Magnetic topological quantum chemistry. *Nature Communications* **12**, 5965 (2021).

[56] Giustino, F. Electron-phonon interactions from first principles. *Rev. Mod. Phys.* **89**, 015003 (2017).

[57] Allen, P. B. & Dynes, R. C. Transition temperature of strong-coupled superconductors reanalyzed. *Phys. Rev. B* **12**, 905 (1975).

[58] Eliashberg, G. M. Interactions between electrons and lattice vibrations in a superconductor. *Sov. Phys. JETP* **11**, 696 (1960).

[59] Margine, E. R. & Giustino, F. Anisotropic Migdal-Eliashberg theory using Wannier functions. *Phys. Rev. B* **87**, 024505 (2013).

[60] Chevalier, B., Lejay, P., Etourneau, J. & Hagenmuller, P. Superconducting and magnetic properties of ternary silicides in some rare earth-noble metal (Rh or Ir)-silicon systems. *Materials Research Bulletin* **18**, 315–330 (1983).

[61] Rauchschwalbe, U. *et al.* Superconductivity in a mixed-valent system: $CeRu_3Si_2$. *Phys. Rev. B* **30**, 444–446 (1984).

[62] Godart, C. & Gupta, L. Coexistence of superconductivity and spin glass freezing in $La_{0.95}Gd_{0.05}Ru_3Si_2$. *Physics Letters A* **120**, 427–429 (1987).

[63] Escorne, M., Mauger, A., Gupta, L. C. & Godart, C. Type-II superconductivity in a dilute magnetic system: $La_{1-x}Tm_xRu_3Si_2$. *Phys. Rev. B* **49**, 12051–12057 (1994).

[64] Chaudhary, S. *et al.* Role of electronic correlations in the kagome-lattice superconductor $LaRh_3B_2$. *Phys. Rev. B* **107**, 085103 (2023).

[65] Li, S. *et al.* Distinct behaviors of suppression to superconductivity in $LaRu_3Si_2$ induced by Fe and Co dopants. *Phys. Rev. B* **86**, 024513 (2012).

[66] Li, B., Li, S. & Wen, H.-H. Chemical doping effect in the $\mathbf{LaRu_3Si_2}$ superconductor with a kagome lattice. *Phys. Rev. B* **94**, 094523 (2016).

[67] Chakrabortty, S., Kumar, R. & Mohapatra, N. Effect of tunable spin-orbit coupling on the superconducting properties of $LaRu_3Si_2$ containing kagome-honeycomb layers. *Phys. Rev. B* **107**, 024503 (2023).

[68] Teng, X. *et al.* Discovery of charge density wave in a kagome lattice antiferromagnet. *Nature* **609**, 490–495 (2022).

[69] Teng, X. *et al.* Magnetism and charge density wave order in kagome FeGe. *Nature Physics* **19**, 814–822 (2023).

[70] Feng, X. *et al.* Catalogue of phonon instabilities in symmetry group 191 kagome MT_6Z_6 materials (2024). arXiv:2409.13078.

[71] Slater, J. C. & Koster, G. F. Simplified LCAO method for the periodic potential problem. *Phys. Rev.* **94**, 1498–1524 (1954).

[72] Yu, J. *et al.* Non-trivial quantum geometry and the strength of electron–phonon coupling. *Nature Physics* **20**, 1262–1268 (2024).

[73] Peotta, S. & Törmä, P. Superfluidity in topologically nontrivial flat bands. *Nature Communications* **6**, 8944 (2015).

[74] Huhtinen, K.-E., Herzog-Arbeitman, J., Chew, A., Bernevig, B. A. & Törmä, P. Revisiting flat band superconductivity: Dependence on minimal quantum metric and band touchings. *Phys. Rev. B* **106**, 014518 (2022).

[75] Gui, X. & Cava, R. J. $LaIr_3Ga_2$: A superconductor based on a kagome lattice of Ir. *Chemistry of Materials* **34**, 2824–2832 (2022).

[76] Gong, C. *et al.* Superconductivity in kagome metal YRu_3Si_2 with strong electron correlations. *Chinese Physics Letters* **39**, 087401 (2022).

[77] Liu, Y. *et al.* Superconductivity in kagome metal $ThRu_3Si_2$. *Chinese Physics B* **33**, 057401 (2024).

[78] Gaggl, T. *et al.* Bulk superconductivity in the kagome metal YRu_3B_2. *Physica Scripta* **101**, 055912 (2026).

[79] Winiarski, M. J. *et al.* YRu_3B_2 – a kagome lattice superconductor. *Journal of Physics: Materials* **9**, 025013 (2026).

[80] Albu Mustaf, R. *et al.* Machine-learning-guided discovery of kagome superconductors YRu_3B_2 and $LuRu_3B_2$. *Phys. Rev. Res.* **8**, 023308 (2026).